Chapter 5
SOFC Modeling

SOFC performance modeling is impacted by the multi-physic processes taking place on the fuel cell surfaces. Heat transfer together with electrochemical reactions, mass and charge transport are conducted inside the cell. There are many mathematical models of the SOFC [1], based mainly on mathematical descriptions of these physical, chemical, and electrochemical properties. There are several parameters affecting cell working conditions, e.g. electrolyte material, electrolyte thickness, cell temperature, inlet and outlet gas compositions at anode and cathode, anode and cathode porosities etc.

The structure of fuel cells is relatively simple, but the way they operate is exceedingly difficult to model. This is due to the large quantity of coefficients to be determined. Several variants of SOFCs are currently being built (e.g. electrolyte, anode or cathode supported, planar, tubular etc.). Additionally, fuel cell layers can be made from many various materials (YSZ, SDC, etc.) and are still under development. In addition, the layers forming the anode and cathode can have different porosities, and even consist of several different layers. Therefore, virtually every technical solution could branch off into broad and interdisciplinary research in pursuit of building model coefficients. A built and validated model is frequently valid only for one specific technical solution and cannot be used for other purposes. There are even problems in scaling up results obtained for small cells. A summary of cell parameters which should be taken into consideration during modeling is shown in Fig. 5.1.

The SOFC models developed thus far are mainly based on the Nernst equation, activation, ohmic, and concentration losses. This approach results in good agreement with experimental data (for which adequate factors were obtained) and poor agreement for other than original experimental working parameters. Moreover, most of the equations used require the addition of numerous factors which are difficult or impossible to determine [2]. Very detailed models (for instance based on finite elements methods) are often characterized by relatively long times needed to find a solution for the used set of equations. Proper identification of all

J. Milewski et al., *Advanced Methods of Solid Oxide Fuel Cell Modeling*,
Green Energy and Technology, DOI: 10.1007/978-0-85729-262-9_5,

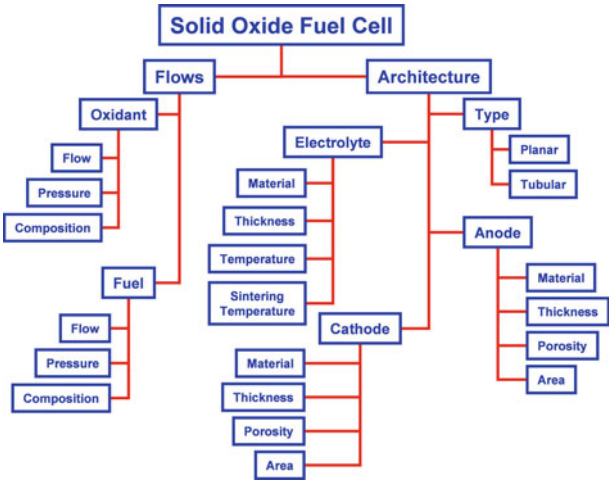

Fig. 5.1 Main parameters of SOFC

Fig. 5.2 Fuel cell modeling

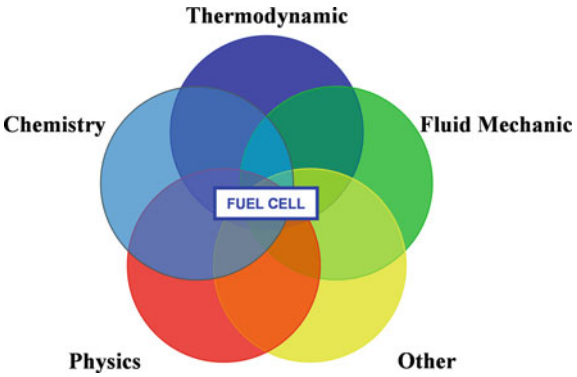

necessary factors and their impact on each other as well as on other parameters can often take a longer time and much more effort than later utilization of the model. Sometimes the task of preparing a model of the SOFC is disproportionately difficult relative to the calculations made subsequently. In practical applications, the complexity of the fuel cell model should not deviate greatly from the models of other devices that make up the whole power-generating module (i.e. turbines, compressors, heat exchangers, pumps, etc.). On occasion, it is far easier to use fully empirical models, e.g. based on an artificial neural network [3], than to make a model founded on basic principles, but of course this approach does not give any information about the main processes which occur during fuel cell operation.

Since fuel cell modeling is a multidisciplinary task (see Fig. 5.2), a good scientific background is needed to describe the fuel cell behavior in an appropriate way. As a first step, all known parameters which influence cell characteristics

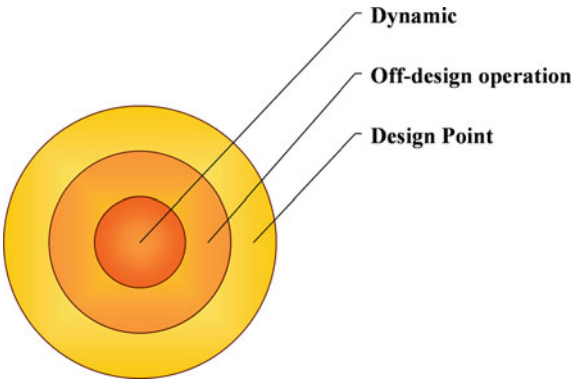

Fig. 5.3 The levels of mathematical modeling

should be selected to eliminate those whose impact can be sidelined. Once the description is ready, adequate experimental data are needed for the model validation procedures.

Mathematical modeling of any system can be divided into three levels:

1. Design point,
2. Off-design operation, and
3. Dynamic.

Figure 5.3 shows schematically all those modeling levels. The most general, and enjoying the largest area of utilization, is design point modeling, which is used mainly for device selection purposes or connectional evaluation of a system. In most cases, only general knowledge of the process is needed. Modeling off-design operation involves those devices, objects, or systems for which adequate characteristics are already known. To describe the off-design operation of a system, a more detailed model is required, often based on real operational data of the modeled object. The result of design point calculation can frequently be used as a reference state for off-design operation estimation. The most difficult and most detailed task is modeling transient behavior of the modeled objects (Fig. 5.4). This entails gathering all available detailed knowledge about the technical solution of the object. Apart from real object characteristics, additional knowledge is needed of time dependent variables (heat accumulation, mass accumulation, etc.)

In fact, in fuel cell modeling only two levels have been used to date: off-design operation (based on the current–voltage curve) and dynamic models. Thus far, the design point model of the SOFC is not specific in terms of details, and often instead of any model there are merely assumed constant values of fuel cell efficiency and voltage.

The typical current–voltage curve is a result of many parameters, which influence fuel cell performance. The parameters can be divided into two groups:

- Thermal-flow parameters,
- Architecture parameters.

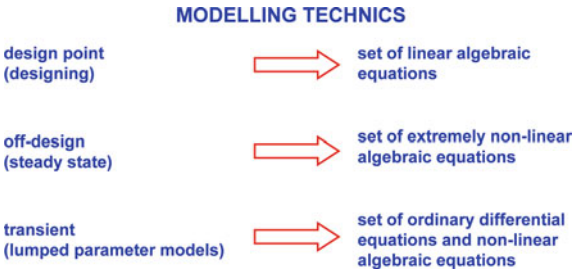

Fig. 5.4 Modeling techniques

Adequate classification of those parameters and their influence on the fuel cell operational characteristic is crucial to model the SOFC behaviors properly. During normal cell operation only thermal-flow parameters can be changed. Hence, the flow parameters mainly regard the off-design operation of the fuel cell. In contrast, at the construction stage we are free to change the design parameters of the cell (electrolyte type, thicknesses, etc.). In this case, a design-point model should be applied. Architecture parameters can be adjusted only in design point level calculation and should be kept at their nominal values. Only if long-term operation of the fuel cell is considered would degradation processes influence the architecture parameters.

5.1 Singular Cell

A singular cell is the basic element, and is composed of three main layers: anode, electrolyte and cathode (see Fig. 5.5). Electrodes are made as porous layers, whereas the electrolyte is a solid layer. There are additional elements (e.g. current collectors, interconnectors, gas manifolds) which impact cell performance, but they are not considered as singular cell components. Often, different materials are used for each cell layer, and it happens that each layer is composed from other layers (i.e. multilayer design).

Operation of a singular cell is often defined by the current–voltage curve, as with voltaic batteries. Seeing as there are many differences between fuel cells and

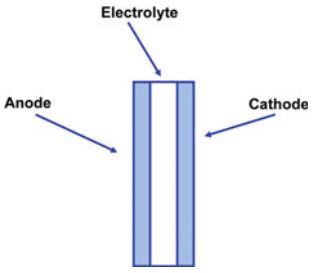

Fig. 5.5 Basic scheme of a singular fuel cell

batteries, using the same mathematical description meets with many difficulties. The most popular and most often used mathematical description of singular cell performance is based on division of the current–voltage curve into three parts: activation, ohmic and concentration. In this book, this type of fuel cell modeling is called the classical approach and is presented first. It is problematic to use the classical approach and its many disadvantages will be pointed out in the next section. A new model was developed, called the advanced approach and we will return to it later.

5.1.1 Classical Approach

The classical approach of fuel cell modeling is based on approximation of the current–voltage curve ($E = f(i)$), which is obtained from experimental studies. The current–voltage curve for modeling purposes is divided into three parts: initial (called activation loss), middle (called ohmic loss) and end (called concentration loss)—see Fig. 5.6. Those losses are subtracted from the maximum voltage defined by the Nernst equation and finally the value of the cell voltage is obtained. In general, several factors (described as functions of current density) are needed for each kind of loss because many various parameters influence those losses simultaneously. Thus, fuel cell voltage is described by a relationship made up of four elements, i.e. maximum voltage ($E_{\max}$), activation losses (η_{act}), losses associated with the resistance of the electrolyte (η_{Ω}), and concentration losses (η_{con}):

$$E = E_{\max} - \eta_{\text{act}} - \eta_{\text{ohm}} - \eta_{\text{con}} \tag{5.1}$$

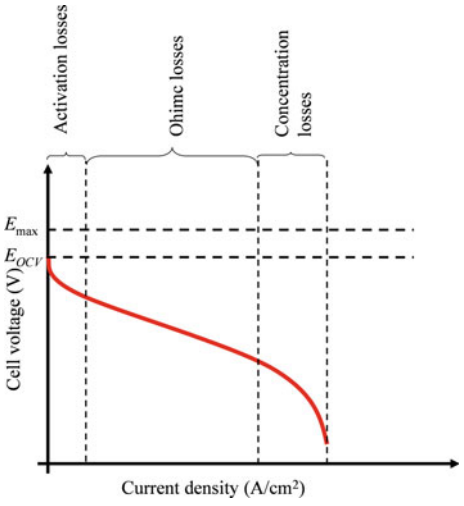

Fig. 5.6 Classical approach to SOFC current–voltage curve modeling

Maximum voltage is referred to the Nernst equation, which is often defined in relation to the reaction of hydrogen with oxygen:

$$E_{\max} = \frac{B \cdot T}{2 \cdot F} \ln K - \frac{B \cdot T}{2 \cdot F} \ln \frac{p_{H_2} \cdot p_{O_2}^{1/2}}{p_{H_2O} \cdot p_{ref}^{1/2}} \tag{5.2}$$

Both activation and concentration losses are described as functions of current density and some additional factors (e.g. i_0, b). The values of these factors are determined for specific fuel cell characteristics and are obtained from experiment results.

5.1.1.1 Activation Losses

The voltage drop in the initial part of the curve, which corresponds to the activation losses, is identified by the Butler-Volmer equation:

$$i = i_0 \cdot \left\{ e^{-\frac{\alpha \cdot n \cdot F}{R \cdot T} \cdot \eta_{act}} - e^{\frac{(1-\alpha) \cdot n \cdot F}{R \cdot T} \cdot \eta_{act}} \right\} \tag{5.3}$$

The complexity of the function renders it impossible to formulate a direct equation for η_{act}, and the calculations must take an iterative approach. The relationship of activation loss is a function of current density $\eta_{act} = f(i)$. In addition, at least the values of both coefficients and i_0 and α must be known. The relationships between these values and flow parameters of the fuel cell are very difficult to determine. The situation becomes even more complicated when there is more than one reaction on the cell surfaces.

In order to simplify the calculation of the Butler–Volmer equation, the main relationship is linearized to the form of the Tafel equation. At sufficiently small η_{act}, (in practice <0.01 V), the Butler–Volmer equation can be developed into a series and then, taking into account only the first two components, a linear representation of it is obtained:

$$\eta_{act} = \frac{R \cdot T}{\alpha \cdot n \cdot F} \ln i_0 - \frac{R \cdot T}{\alpha \cdot n \cdot F} \ln i \tag{5.4}$$

Assuming a constant temperature, Eq. 5.4 can be written in the form of the Tafel equation:

$$\eta_{act} = a + b \cdot \ln i \tag{5.5}$$

Neither the original Butler–Volmer nor the Tafel equations allow for accurate identification of the voltage for open circuit voltage (either tending to infinity, or becoming undefined, depending). The Butler–Volmer equation is used to determine the value of the coefficient i_0, whereas the coefficient b is determined by taking into account the diffusion laws.

Activation polarization can be described separately for anode and cathode by analyzing half-side reaction or triple-phase boundaries.

5.1.1.2 Ohmic Losses

After the part where the dominant role is played by the activation losses, the current–voltage curve becomes almost linear in its middle range. This part of the curve is described by the losses associated with the resistance of the electrolyte (ohmic losses) by the following relationship:

$$\eta_{\Omega} = r \cdot i \tag{5.6}$$

Usually, there is no distinction between electronic resistance and ionic resistance, and the factor r corresponds to the mixed conductivity of the entire cell.

5.1.1.3 Concentration Losses

In the final part of the current–voltage curve, the dominant role is played by the losses associated with the transport of gases in a perpendicular direction to the surface of the electrodes. The flows of these gases can occur in both directions simultaneously, i.e. toward electrolyte (the flow of gases involved in reactions), and in the opposite direction (reactants flow). The flow of the gases and their distribution in the perpendicular direction to the electrode surface is described by the diffusion laws. The electrodes are made of porous materials, which also affect the way of delivery and receipt of gas around the reaction zone.

The amount of gas flowing perpendicular to the electrode surface is determined by both the type of reaction occurring and the current density drawn from the cell. If the diameter of the pores of electrode layer is significant greater than the average molecule path, the flow of these gases can be described by Fick's law (or other diffusion laws, see Sect. 1.4). In the opposite case, i.e. where the path is comparable to the size of pores, the transport phenomenon is described by Knudsen diffusion. There are several empirical or semi-empirical relationships which can be found in the literature, below is one which defines dependencies for the flow at the anode channel for the reaction of hydrogen with oxygen:

$$\eta_{\text{con}} = \frac{R \cdot T}{2F} \ln\left(1 + \frac{p_{\text{H}_2} \cdot i}{p_{\text{H}_2 \cdot \text{i}_\text{l}}}\right) - \frac{R \cdot T}{2F} \ln\left(1 - \frac{i}{i_l}\right) \tag{5.7}$$

The concentration losses are influenced mainly by parameter i_l, called a limiting current density, which is a function of many various parameters, mainly:

$$i_l = f(D,\ \text{microstructure},\ \text{partial pressures etc.})$$

A value of the limiting current density must be estimated individually for each case; an example relationship is presented here:

$$i_l = \frac{2F \cdot p_{H_2} \cdot D}{R \cdot T \cdot \delta_{\text{electrode}}} \tag{5.8}$$

5.1.1.4 Discussion

The classical approach makes for many difficulties during calculations, e.g. it virtually ignores the impact of the quantity of gas supplied on the cell surface, focusing only on the current density drawn from it. Greatly affecting performance is the fact that the fuel cell can be fed by different amounts of gas (at both anode and cathode) for the same value of current density.

The classical approach results in relative good agreement with particular experimental data (for which adequate factors were obtained) and poor agreement for non-original experimental working parameters. This means that determination of the performance of the fuel cell under other conditions is very difficult and the model cannot be extrapolated. Moreover, most of the equations require the addition of numerous factors (porosity, tortuosity, ionic and electronic paths, etc.) that are hard to determine and which often relate to the microscopic properties of the cell. Very often those parameters are used as just the fitting parameters, without any physical background. This is particularly relevant in the case of complex fuels feeding. It is not easy to determine all necessary coefficients and factors even for a few current–voltage curves generated with dry hydrogen as a fuel. The addition of other components makes this task much more taxing. In the most complex cases, singular current–voltage curve is described by several empirical coefficients (up to 6), and even a minimal change in the work cell operational conditions results in a need to correct these factors. It should be noted that the singular curve relates only to specific conditions of work cells, i.e. fixed rates of delivered gases, constant temperature, pressure, etc.

Models based on an approximation of the current–voltage curve are in fact models for off-design operation and they should be used only for specific and fixed gas compositions at both anode and cathode sides. Widespread use of the classical approach models for calculating the nominal point (called design-point) appears unjustified and, frankly, wrong.

5.1.2 Advanced Approach

The presented model in this section is termed “advanced” not because of the complex equations used, but because it affords an opportunity to investigate the influences of key factors on fuel cell performance in isolation from each other. This means that when changing one parameter (e.g. fuel flow, electrolyte type, temperature, anode thickness, etc.) there is no need to change the values of the other coefficients used.

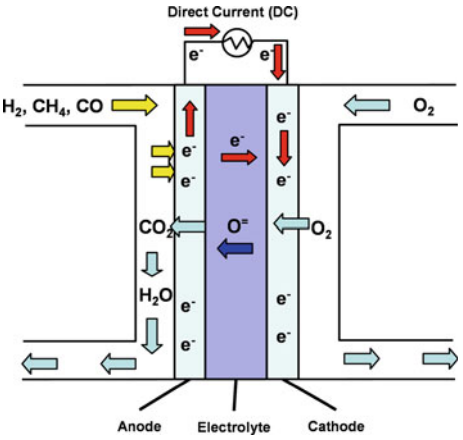

Fig. 5.7 Working principles of SOFC

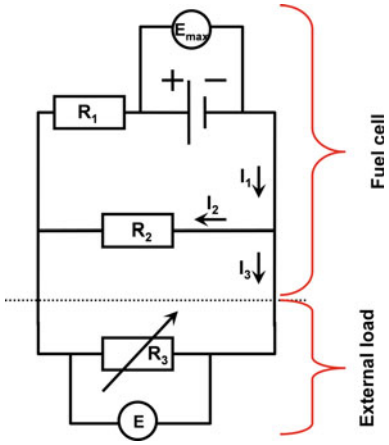

Fig. 5.8 Equivalent electric circuit of fuel cell

The working principles of SOFCs are shown in Fig. 5.7. The SOFC working principles are based on partial oxygen pressure difference between the cathode and anode side. The pressure difference forces oxygen ions (O^{-2}) to pass through the solid electrolyte. This process generates voltage and an electric current can be drawn from the cell. A reverse working mode is also possible (e.g. oxygen pumps). To obtain a practical value of generated voltage, oxygen partial pressure at the anode side must be very low ($\approx 10^{-20}$ MPa), which can be achieved through oxidization of the fuel at the anode side.

Oxygen ions are electrons carriers, thus the fuel cell working principles can be described by an adequate electric circuit. An equivalent electric circuit of the fuel cell is illustrated in Fig. 5.8. Because of mixed conductivity of the electrolyte (ionic and electronic), two types of resistance are present in fuel cells: ionic resistance R_1 and electrical resistance R_2. Resistance R_3 is the external load

resistance of the fuel cell, for the electric circuit shown in Fig. 5.8, using both Ohm's and Kirchhoff's laws, a set of equations can be built as follows:

$$I_1 = \frac{E_{\max} - E}{R_1} \tag{5.9}$$

$$I_2 = \frac{E}{R_2} \tag{5.10}$$

$$I_1 = I_2 + I_3 \tag{5.11}$$

In order to correlate the electrical dependence with gas flows, the fuel utilization factor is used. This parameter defines the ratio of fuel, which is used in the electrochemical reaction producing electrical current, in relation to the total fuel flow delivered to the cell. It is sufficient to assume that the fuel utilization factor is zero when the fuel cell does not provide power to an external load. Nevertheless, because of the presence of the resistance R_2 it is impossible to obtain a zero fuel utilization factor even with completely disconnected from the external circuit ($R_3 = \infty$). To make the model more reliable, the fuel utilization factor is correlated with the current drawn from the cell by the following equation:

$$I_3 = (I_{\max} - I_2) \cdot \eta_f \tag{5.12}$$

Solving Eqs. 5.11 and 5.12, the equation for cell voltage is obtained:

$$E = \frac{E_{\max} - I_{\max} \cdot R_1 \cdot \eta_f}{\frac{R_1}{R_2}(1 - \eta_f) + 1} \tag{5.13}$$

The maximum current ($I_{\max}$) for a given fuel flow can be determined using the relationship:

$$I_{\max} = 2 \cdot F \cdot n_{\mathrm{H_2,\,equivalent}} \tag{5.14}$$

Fuel cells have different areas (from 1 to over 100 $\mathrm{cm^2}$), so in order to generalize relationships, the current drawn from the cells and the resistances are referred to as active cell surfaces and labeled in lowercase letters:

$$i_{\max} = \frac{2 \cdot F \cdot n_{\mathrm{H_2,\,equivalent}}}{A_{\mathrm{cell}}} \tag{5.15}$$

$$E_{\mathrm{SOFC}} = \frac{E_{\max} - i_{\max} \cdot r_1 \cdot \eta_f}{\frac{r_1}{r_2}(1 - \eta_f) + 1} \tag{5.16}$$

Solid oxide fuel cell voltage depends then on main five various parameters:

1. Maximum voltage—$E_{\max}$
2. Maximum current density—$i_{\max}$
3. Fuel utilization factor—η_f
4. Area specific internal ionic resistance—r_1
5. Area specific internal electronic resistance—r_2

Table 5.1 Maximum voltages for various reactions

Chemical reaction	Maximum voltage (E_{max} at 20°C)
$H_2 + \frac{1}{2}O_2 \rightarrow H_2O$	1.23
$CH_4 + 2O_2 \rightarrow CO_2 + H_2O$	1.06
$CH_3OH + \frac{3}{2}O_2 \rightarrow CO_2 + 2H_2O$	1.22
$C + O_2 \rightarrow CO_2$	1.03
$C + \frac{1}{2}O_2 \rightarrow CO$	0.72
$CO + \frac{1}{2}O_2 \rightarrow CO_2$	1.34

Those parameters are relatively independent of each other and can be investigated and described individually.

5.1.2.1 Maximum Voltage

The maximum voltage of the fuel cell depends on the type of reaction occurring on the electrode surfaces and is defined by the reaction of maximum work (see Sect. 2.1.3). The maximum voltages for various reactions are listed in Table 5.1.

From Table 5.1 it can be seen that various fuels in reaction with oxygen can give various maximum voltages. In the case of SOFCs, the reaction zone is placed at the anode side where mixtures of various components occur. Due to these circumstances the general form of the Nernst equation is used to estimate the voltage of the SOFC (see Eq. 2.38).

Adequate partial pressures can be calculated with the assumption that there is a state of chemical equilibrium at the anode side, which is mainly true only for hydrogen as a fuel. In the case of other fuels (e.g. hydrocarbons), the partial pressures should be obtained by kinetic (dynamic) calculation of reactions, for instance, at 800°C methane reacts 10^6 slower than hydrogen.

Both anode and cathode layer are made as porous layers—which causes an additional pressure drop across the layers and those phenomena should be taken into account by implementing adequate relationships for transport in porous media.

5.1.2.2 Maximum Current Density

The total current which can be drawn from the cell correlates strictly with the amount of either fuel or oxidant delivered. This means that it is a value of current for which the whole fuel is utilized—I_{max}. Then, the fuel utilization factor can be correlated with the current generated by the cell Eqs. 5.12 and 5.14.

The mixture of various fuels enters into the SOFC anode, so the fuel utilization factor is calculated based on an equivalent hydrogen molar flow. At elevated temperatures, hydrocarbon fuels are decomposed to hydrogen by steam

reforming reactions. Internal reforming reactions of hydrocarbons are mainly strongly endothermic, which means that heat is transformed into fuel by the decomposition of water molecules into hydrogen. So, assuming an internal reforming reaction, the equivalent hydrogen molar flow at the anode inlet for hydrocarbon containing fuel is defined by the following relationship:

$$n_{\mathrm{H_2,\,equivalent,\,out}} = n_{\mathrm{H_2}} + n_{\mathrm{CO}} + 3n_{\mathrm{CH_3OH}} + 4n_{\mathrm{CH_4}} \tag{5.17}$$

$$+6n_{\mathrm{C_2H_5OH}} + 7n_{\mathrm{C_2H_6}} + 10n_{\mathrm{C_3H_8}} \tag{5.18}$$

$$+13n_{\mathrm{C_4H_{10}}} \tag{5.19}$$

The design-point model can be used for selecting the fuel cell size according to other system elements (gas turbine, heat exchangers, etc.), and the value of maximum current density ($i_{\max}$) is constant this case. This means that in design point calculations the cell area is always fixed in relation to both inlet fuel and oxidant flows. A lower value of $i_{\max}$ means a larger cell area of the fuel cell for the same fuel utilization factor. In such cases, the fuel utilization factor is equivalent to current density and the fuel cell characteristic can be drawn as a voltage-fuel utilization factor curve ($E = f(\eta_f)$) instead of a voltage–current density curve ($E = f(i)$).

The value of maximum current density can be chosen arbitrarily depending on the results of technical economic analysis. For laboratory cells with relatively small areas ($1-2\,\mathrm{cm^2}$) the exemplary value of $i_{\max}$ was determined by the researchers' own calculations. This value equals to $4.58\,\mathrm{A/cm^2}$, which is based on data taken from [4, 5].

During off-design calculations, the area of the cell is fixed, which means that factor $i_{\max}$ has to be calculated based on the Eq. 5.15.

5.1.2.3 Fuel Utilization Factor

The real value of the fuel utilization factor is defined by the following relationship:

$$\eta_{f,\,\mathrm{real}} = 1 - \frac{n_{\mathrm{H_2,\,equivalent,\,out}}}{n_{\mathrm{H_2,\,equivalent,\,in}}} \tag{5.20}$$

In fact, due to the presence of area specific electronic resistance, real fuel utilization will never reach a value of 0. It is more convenient to use the fuel utilization factor defined by Eq. 5.27 because its value can be varied in the range 0–1, and the real value of η_f must be calculated iteratively based on the following relationship:

$$\eta_{f,\,\mathrm{real}} = \eta_f + E_{\mathrm{SOFC}} \frac{1-\eta_f}{r_2 \cdot i_{\max}} \tag{5.21}$$

It may happen that the oxidant utilization factor, not the fuel utilization factor, turns out to be the limiting factor. It should always be checked which one of those

two factors limits fuel cell current density. During normal operation, the fuel cell is cooled by air flow delivered to the cathode, which means that quantity of oxygen always exceeds the stoichiometric ratio. In other cases, the fuel utilization factor in the Eq. 2.38 should be replaced by the oxidant utilization factor.

5.1.2.4 Area Specific Ionic Resistance

The solid oxide fuel cell consists of electrolyte covered by anode and cathode layers. Those layers influence ionic conductivity (e.g. triple boundary phase processes). The material used, porosity and design of the electrodes exert a major influence over fuel cell voltage. Additionally, both electrolyte and electrodes can be built as multi-layers with varied compositions in the cross-section of the fuel cell. Then, the total area specific ionic resistance of the solid oxide fuel cell can be estimated by the following relationship:

$$r_{1,\,\text{total}} = \sum \frac{\delta_{\text{electrolyte}}}{\sigma_{\text{electrolyte}}} + \sum \frac{\delta_{\text{anode}}}{\sigma_{\text{anode}}} + \sum \frac{\delta_{\text{cathode}}}{\sigma_{\text{cathode}}} \tag{5.22}$$

The ionic conductivity of the solid oxide is defined as follows:

$$\sigma_1 = \sigma_0 \cdot e^{\frac{-E_{\text{act}}}{R \cdot T}} \tag{5.23}$$

where: σ_0, E_{act}—factors dependent on material used.

Ionic resistance of solid oxides is relatively well known and often published. Exemplary data gathered from many sources are presented in Fig. 5.9. Adequate factors of Eq. 5.23 can read directly from the presented graph.

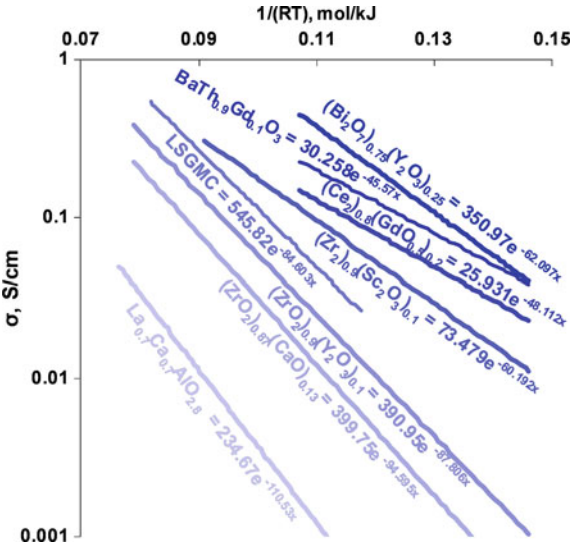

Fig. 5.9 Temperature dependence of ionic conductivity for solid oxides

5.1.2.5 Area Specific Electronic Resistance

In general, solid oxides are assumed to be only ionic conductors, but in fact electron conductivity is present as well [2]. On the other hand, gas leakage through the electrolyte has the same effect as electron (electrical) conductance and can be described in the same way.

The second type of internal resistance is electrical resistance—r_2. The influences of temperature and electrolyte thickness on electronic internal resistance of the electrolytes are not well known. The electronic conductivity values of solid oxide electrolytes are spread across a very wide range. They do not have a major impact on calculated cell voltage for high fuel utilization factors. It is hard to measure the electronic resistance of solid oxide electrolytes since they have both conductivities (ionic and electronic) simultaneously, which gives total electrical resistance. It should be noted that decreasing electrolyte thickness reduces ionic resistance (positive effect), but also probably reduces electronic resistance (negative effect).

The difference between calculated maximum cell voltage and related open circuit voltage can be explained by the electrical resistance. The presence of the resistance R_2, makes the open circuit voltage (E_{OCV}) lower than the maximum voltage $E_{\max}$. For given $r_1, E_{\max}$ and E_{OCV} (from experimental measurements) the value of electrical resistance of the cell can be described by using the following relationship:

$$r_2 = \frac{\delta}{\sigma_2} \tag{5.24}$$

The value of electronic resistance of the cell can be estimated from available experimental results. Substituting $\eta_f = 0$ into Eq. 5.16, the E_{OCV} can be defined by the following relationship:

$$E_{\mathrm{OCV}} = \frac{E_{\max}}{\frac{r_1}{r_2} + 1} \tag{5.25}$$

Substituting Eq. 5.24 into Eq. 5.25, the relationship for electrical conductivity of the cell is obtained:

$$\sigma_2 = \delta \cdot \frac{E_{\max} - E_{\mathrm{OCV}}}{r_1 \cdot E_{\mathrm{OCV}}} \tag{5.26}$$

The electronic conductivities of solid oxides were estimated by using Eq. 5.26 and based on experimental data published in [6–13]. The result of this estimation is shown in Fig. 5.10. Adequate factors of electronic conductivity can be read directly from the graph.

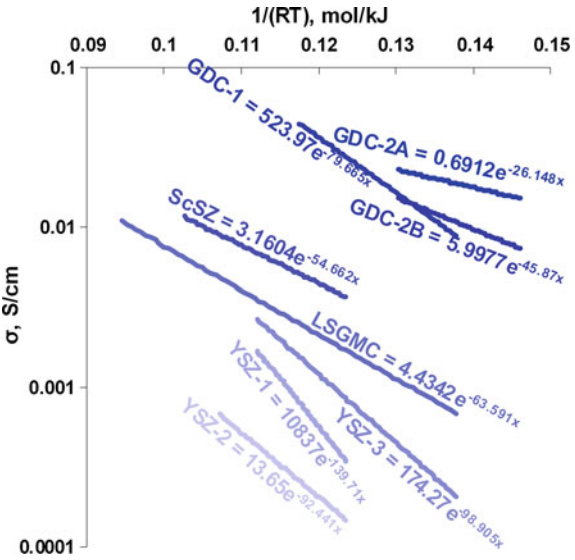

Fig. 5.10 Temperature dependence of electrical conductivity for solid oxide fuel cells

5.1.2.6 Off-Design Operation

In contrast to the calculation of the nominal point, during off-design operation, the given value is the current drawn from the cell instead of the fuel utilization factor. The correlation between current density and the fuel utilization factor is given by the following relationship:

$$\eta_f = \frac{i \cdot (r_1 + r_2)}{i \cdot r_1 - E_{\max} + i_{\max} \cdot (r_1 + r_2)} \tag{5.27}$$

In view of the fact that the voltage E is not initially known, meaning that the calculation procedure must be changed, and convergence should be obtained by an iterative process. Additionally, during off-design operation, the maximum value of current density is not constant and depends on the amount of fuel fed, according to Eq. 5.15. Finally, the fuel cell voltage during off-design operation calculations is defined by the following equation:

$$E_{\text{SOFC}} = \frac{E_{\max} - i \cdot r_1}{\frac{r_1}{r_2} \cdot \left(1 - \frac{i}{i_{\max}}\right) + 1} \tag{5.28}$$

5.1.2.7 Discussion

The main advantage of the advanced model is that all parameters used have physical explanations and can be varied over practically achieved ranges.

The model gives reasonable results for each case in which both material and thermal flow parameters are changed. Influences of many physical parameters of the SOFC are extracted from the current–voltage curve and can be investigated separately. The model is based on a combination of electric laws, gas flow relationships, solid material properties and electrochemistry correlations and is characterized by as low a number of requisite factors as possible. During calculations, the advanced model is very stable and can be used for both simulations and optimization procedures. In contrast, the classic model is very sensitive to input parameters and very often generates nonphysical results (e.g. for $i = 0\,\mathrm{A/cm^2}$).

The advanced approach is based on a clear division between design point modeling and off-design operation. The model can be relatively easily expanded to 2D/3D modeling by using finite element methods (see Sec. 5.1.2). Moreover, by knowing some new factors about used materials, the fuel cell characteristics can be obtained even without experiments, based merely on previous investigations. The disadvantage of the advanced model is that, to date, not all necessary parameters have been defined in depth.

Based on the advanced approach, fuel cell losses are estimated and are shown in Fig. 5.11. The maximum voltage calculated for partial pressures taken at both the anode and cathode outlets gives adequate shape according to both activation and concentration (diffusion) losses. The rest losses are generated by the two resistances represent. The influence of electrical resistance (r_2) occurs mainly at the start of the fuel cell operation curve. In the advanced model, the losses can be defined separately for each layer making up the cell. From Fig. 5.11, it is clear that

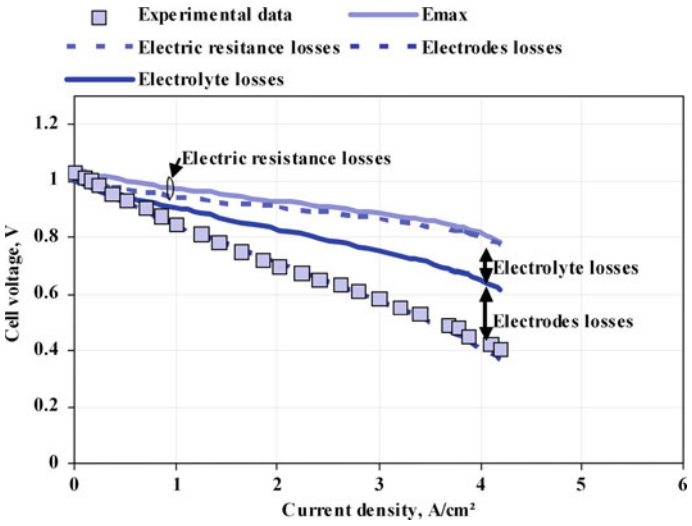

Fig. 5.11 Voltage-current density curve with indicated main cell losses—used experimental data are also shown

the main losses are generated across the cell electrodes (both anode and cathode). Electrolyte losses are only responsible for about 20% of total voltage loss.

5.1.2.8 Quasi-1D Model

The advanced approach is based on 0D modeling but can be expanded to higher dimension models by utilizing finite element methods. An example of 1D model based on equations presented previously is given. The model architecture is composed from 30 dimensionless finite elements (see Fig. 5.12), which describe flow gases along fuel cell channels parallel to the fuel cell surface. It is assumed that there is no pressure drop across either direction (parallel or perpendicular) in relation to cell area and there are no diffusion processes inside the cell channels. It was assumed that all values (e.g. concentration of species, temperature of electrolyte, etc.) along the direction of reactant and oxidant flows are at their average values for each finite element. Boundary conditions are as follows:

- Air flow at cathode inlet: 275 ml/min/cm^2
- Hydrogen flow at anode inlet: 150 ml/min/cm^2
- Temperature is constant along the channels and equals 800°C
- Total cell area: 1 cm^2
- Pressure: 1 bar

Each finite element has the same voltage, but varying electromotive forces. Increasing local current causes a drop in voltage from the value given by the electromotive force to the working cell voltage. From an electrical point of view, the finite elements of the cell are connected in parallel; at the same time they have various electromotive forces given by Eq. 5.16. During steady-state conditions, in parallel connection, output voltage is the lowest of all the elements. Assuming that each finite element has the same area, the current for the element is defined by the following equation:

$$I_{\text{local}} = I_{\text{total}} \frac{E_{\text{local}}}{\sum E_{\text{local}}} \tag{5.29}$$

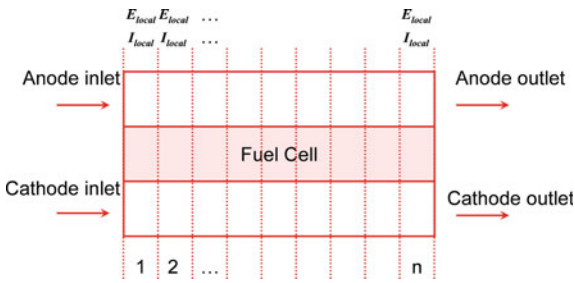

Fig. 5.12 1D model configuration

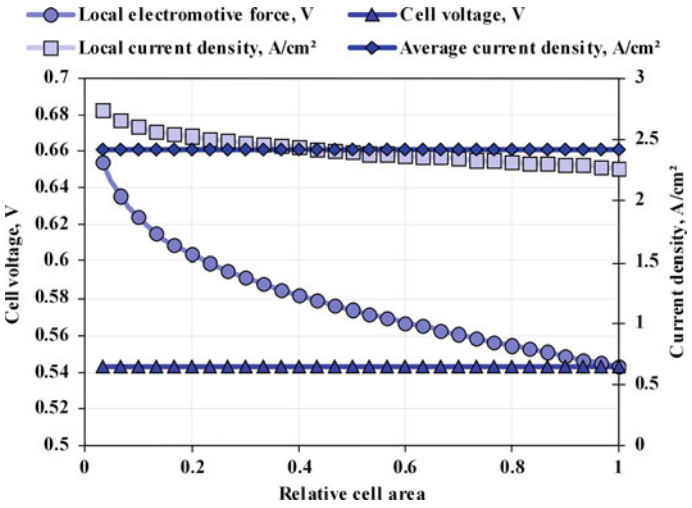

Fig. 5.13 Cell voltage, local electromotive force and local current density distribution along the cell for average current density 2.4 A/cm^2

The model was created in spreadsheet software, and the distribution of main fuel cell working parameters is presented in Fig. 5.13. The results refer to a singular point on the current–voltage curve for the current density at the level of 2.4 A/cm^2. Presented values contain four parameters: local voltage (local electromotive force), local current density, cell voltage (the lowest value of local voltage), and average value of current density. The last two parameters are included to show deviations between 1 and 0D models. It is shown that current density distribution varies in the range (−7 to +13%) of its average value whereas maximum local voltage is about 20% higher than the voltage generated by the cell. The results obtained by 1D model are more accurate; for the same conditions 0D model gives a voltage value of 0.51 V whereas 1D model gives 0.54—a difference of about 7%.

Figure 5.13 were not compared against experimental data, because the latter do not exist. The idea of presenting this graph is show that the model can be used for finite element calculation purposes, and hypothetical distributions of main cell parameters are presented.

5.1.2.9 Practical Example

Problem

Find the solid oxide fuel cell voltage for given: fuel (hydrogen) flow rate: 140 ml/min, oxidant (air) flow rate 550 ml/min, temperature 800°C, current density 1 A/cm^2, pressure 1 bar. Cell parameters: electrolyte made from YSZ with thickness of 8 μm,

total anode and cathode area specific ionic resistance 0.1291 cm^2/S (at 800°C) and the cell internal electronic resistance 5.5 cm^2/S (at 800°C), cell area 1.1 cm^2.

Solution

Firstly, the maximum current density is estimated. Because, the maximum current density can be limited by fuel flow or oxidant, those two values are calculated below.

$$\begin{aligned} i_{\max,f} &= \frac{2F \cdot n_{\mathrm{H_2}}}{A} = \frac{2F \cdot \frac{p \cdot V}{R \cdot T}}{A} \\ &= \frac{2 \cdot 96485 \cdot \frac{1 \cdot 10^5 \cdot 300 \frac{10^{-6}}{60}}{8.315 \cdot (800+273.15)}}{1.1} \\ &= 4.58 A/\mathrm{cm}^2 \\ i_{\max,o} &= 2 \cdot i_{\max,f} \cdot \frac{V_o}{V_f} \\ &= 2 \cdot 4.58 \cdot \frac{550 \cdot 0.21}{140} \\ &= 7.56 A/\mathrm{cm}^2 \end{aligned}$$

This means that the limiting factor is based on fuel flow delivered. Next, both fuel utilization factor and oxidant utilization factor are estimated based on adequate values of maximum current densities:

Fuel Utilization Factor

$$\eta_f = \frac{i}{i_{\max,f}} = \frac{1}{4.58} = 21.8\%$$

Oxidant utilization factor

$$\eta_o = \frac{i}{i_{\max,o}} = \frac{1}{8.28} = 13.2\%$$

Area Specific Internal Ionic Resistance By utilizing Eq. 5.22 and taking data from Fig. 5.9, the area specific ionic resistance equals:

$$\begin{aligned} r_1 &= \frac{\delta_{\text{electrolyte}}}{\sigma_{\text{electrolyte}}} + r_{1,\text{ electrodes}} \\ &= \frac{\delta_{\text{electrolyte}}}{\sigma_0 \cdot e^{\frac{-E_{\text{act}}}{R \cdot T}}} + r_{1,\text{ electrodes}} \\ &= \frac{8 \cdot 10^{-4}}{390.95 \cdot e^{\frac{-87.806 \cdot 10^3}{8.315 \cdot (800+273.15)}}} + 0.1291 \\ &= 0.0384 + 0.1291 \\ &= 0.1675\,\mathrm{cm}^2/\mathrm{S} \end{aligned}$$

For simplicity, it can be assumed that $\eta_{f,real} = \eta_f$, partial pressures of the anodic gases are

$$\begin{aligned} p_{H_2,\,\text{anode, out}} &= p_{H_2,\,\text{anode, in}} \cdot (1 - \eta_f) = 1 \cdot (1 - 0.22) = 0.78\,\text{bar} \\ p_{H_2O,\,\text{anode, out}} &= p_{H_2O,\,\text{anode, in}} + p_{H_2,\,\text{anode, in}} \cdot \eta_f \\ &= 0 + 0.22 = 0.22\,\text{bar} \\ p_{O_2,\,\text{cathode, out}} &= p_{O_2,\,\text{cathode, in}} \cdot (1 - \eta_o) \\ &= 0.21 \cdot (1 - 0.132) = 0.182\,\text{bar} \end{aligned}$$

Now, the maximum voltage of the SOFC can be estimated by utilizing Eq. 2.43:

$$\begin{aligned} E_{\max} &= 1.317 - 2.769 \cdot 10^{-4} \cdot T \\ &\quad + \frac{R \cdot T}{2F} \ln\left(\frac{p_{H_2,\,anode} \cdot p_{O_2,\,cathode}^{1/2}}{p_{H_2O,\,anode} \cdot p_{ref}^{1/2}}\right) \\ &= 1.317 - 2.769 \cdot 10^{-4} \cdot (800 + 273.15) \\ &\quad + \frac{8.315 \cdot (800 + 273.15)}{2 \cdot 96485} \ln\left(\frac{0.78 \cdot 0.182^{1/2}}{0.22 \cdot 1^{1/2}}\right) \\ &= 1.317 - 0.297 + 0.0191 = 1.04V \end{aligned}$$

And finally, the fuel cell voltage is obtained:

$$\begin{aligned} E_{\text{SOFC}} &= \frac{E_{\max} - i_{\max} \cdot r_1 \cdot \eta_f}{\frac{r_1}{r_2}(1 - \eta_f) + 1} \\ &= \frac{1.04 - 4.56 \cdot 0.1675 \cdot 0.218}{\frac{0.1675}{5.5}(1 - 0.218) + 1} \\ &= \frac{0.874}{1.024} = 0.854V \end{aligned}$$

5.1.3 Artificial Neural Network Based Model

The most extensive natural neural network is the human brain, having, on average, a volume of 1400 cm^3 and surface of 2000 cm^2 (a comparable sphere with the same volume has only 600 cm^2) and weighs 1.5 kg. The number of connections between cells is about 10^{15}. Nerve cells send and receive pulses with a frequency of 1–100 Hz, duration of 1–2 ms, voltage of 100 mV and speed of propagation of 1–100 m/s. The speed of the brain is estimated at 10^{18} operations per second (compared to the fastest computer in the world, which works at ETA10 10^{10} operations per second). In order to implement the typical reaction, the brain

performs no more than 100 elementary steps with a response time of less than 300 ms. Sensory channel capacity can be estimated at:

- Vision: 100 Mb/s;
- Touch: 1 Mb/s;
- Hearing: 0.015 Mb/s;
- Smelling: 0.001 Mb/s;
- Taste: 0.0001 Mb/s.

The neuron shown in Fig. 5.14, is a key element of the system. The neuron has a body with elements of cytology equipment called soma, which are located inside the nucleus. The neuron soma grow several tabs, which serve important roles in combination with other cells. There are two types of outgrowths: a series of thin and thick, and thicker dendrites bifurcate at the end of the axon.

Input signals are fed into the cell via a synapse (connection axon–dendrite), and the output is discharged by means of axon and its many branches, which after reaching the soma and dendrites of other neurons, create the next synapse.

In simple terms it can be assumed that the transmitted signal from one nerve cell to another is based on secretion under the influence of stimuli coming from the synapse in the form of special chemicals called neuro-mediators. These substances affect the cell membrane by changing its electrical potential. Individual synapses vary in size and the ability to collect the neuro-mediator near the synaptic membrane.

Cell inputs can be assigned numerical coefficients (weights) corresponding to the quantity of neuro-mediator evolved once at the individual synapses. Synaptic Weights are real numbers and may take positive values (an aphrodisiac effect) and negative values (inhibitory).

The neuron responds in accordance with the value of all the impulses accumulated in a short period of time, called the latent period of aggregation.

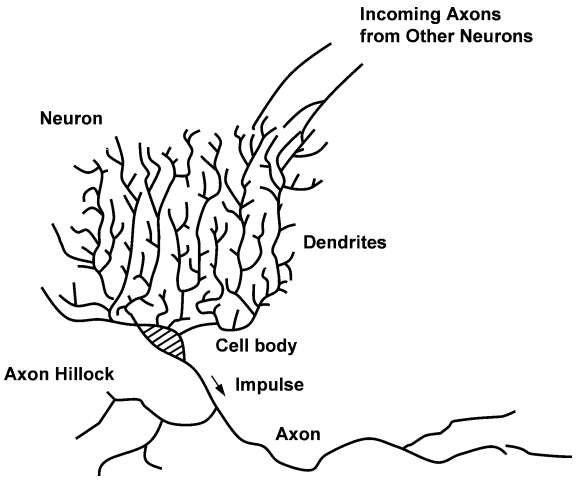

Fig. 5.14 Simplified diagram of a nerve cell

The neuron responds if the full potential of the cell reaches a certain level. After fulfilling its role the neuro-mediator is removed by absorption or distribution.

Artificial neural networks can be very effective as a computational tool in performing tasks that computers and common programs typically find problematic. Artificial neural network calculations are performed in parallel, and therefore the speed of neural networks can greatly exceed the speed of sequential computation. An ANN is able to obtain a solution without going through the stage of constructing an algorithm to solve the problem. Networks do not need programming, and, using existing methods of learning and self-learning, complete their target operation even in a situation where we have no knowledge of the algorithm which posed the problem. The network will always work as a whole and its individual components contribute to the implementation of all operations which implement the network. One consequence of the action network is its ability to function correctly, even after damage to some elements. ANNs have the ability to generalize knowledge, which means that, having been taught, the network is able to provide correct answers for similar but not identical questions to those already known.

Neural networks do not work in situations where there is a need for clear and precise results—i.e. with a variety of complex calculations, handling bank accounts, etc. ANNs may be used in situations where the problem demands multi-step reasoning. The network solves the problem in one step, even if during this process it comes up with some intermediate conclusions.

The Artificial Neural Network (ANN) can be applied to simulate an object's behavior without an algorithmic solution, merely by utilizing available experimental data. Utilization of ANNs for modeling singular SOFCs appears a very promising way to obtain an advanced model of SOFCs which makes rapid convergences (no iterations) and matches experimental data with a low degree of error. The ANN based model is very useful for rapid SOFC calculations, e.g. dynamic simulations, because it does not require iterations during the calculations. The ANN based SOFC model can be used for both cell and system simulations with timeless convergence. It gives results very close to the experimental data as well as for other working environments. This means the model predicts SOFC performances for various working conditions. The model can be used in control and monitoring of the real system to predict performance prior to changing the control parameters.

5.1.3.1 Neuron Structure

An ANN is a black-box model which produces certain output data as a response to a specific combination of input data. It can be trained to learn internal relationships and predict system behavior without any physical equations. ANNs consist of neurons gathered into layers. Information is delivered to the neurons by dendrites and the activation function is realized (by the nucleus). Then modified information is transferred forward by the axon and synapses (see Fig. 5.15) to other neurons.

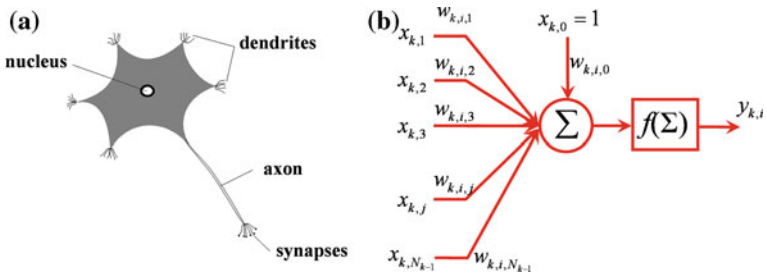

Fig. 5.15 Neuron scheme (**a**) and its mathematical model (**b**)

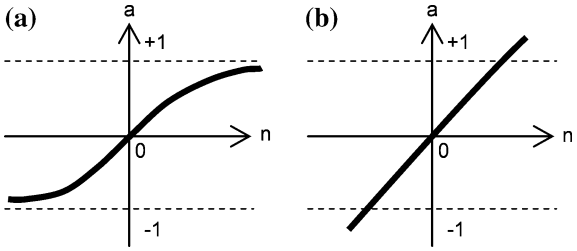

Fig. 5.16 Hyperbolic tangent sigmoid (**a**) and linear transfer functions (**b**)

Each neuron in the first layer takes input values, multiplies them by the corresponding weights ($w_{k,i,1}$) and summarizes all these multiplications. Bias ($x_{k,0}$) is added to the sum ($s_{k,i}$). The sum ($s_{k,i}$) is recalculated by the neuron activation function, giving the neuron answer: $y_{k,i}$. In this study, a hyperbolic tangent sigmoid transfer function was used as the neuron activation function in the first layer, whereas a linear transfer function was used in the output layer (see Fig. 5.16).

5.1.3.2 ANN Structure

There are many types of artificial neural networks, and they are used for different applications. The type of network used affects both the quality and speed of the learning process. They can be categorized by structure as follows:

- Networks are linear systems in the embryonic stage which mimic the real biological structure (which is certainly not linear). They are easy to build and learn well (provided that the model can be built on a linear model).
- MLP networks (multi-layer perceptron) are built from neurons with nonlinear (sigmoidal) characteristics arranged in multiple layers and performing different roles. Among them are: the input layer, the hidden layers accepting input signals that carry information about the task to be solved and mainly house the intelligence network, and the output layer, which provides the final result. This type of network was used to simulate solid oxide fuel cell behavior.

- RBF networks (radial basis functions) form a very extensive hidden layer in which neurons have non-monotonic characteristics, making input data grouping in clusters
- Kohonen networks (SOM—self organizing maps) have the ability to self-learn and can acquire knowledge without a teacher.
- Hopfield networks, unlike all the other networks discussed above, have feedback that connects the output layer to the input.

Networks with the wrong configuration will not be able to learn the relevant correlation. This may be caused by a configuration that is either too complex or too simple.

In addition to an appropriate reflection of the data used to teach it, the network also requires an appropriate generalization of the results, so that the network correctly corresponds to data previously never "seen".

Information proceeds step by step from the first layer to the last one. The answers of the neurons in the last layer are the output parameters of the ANN model (see Fig. 5.17).

5.1.3.3 Experimental Data for Training Procedures

For training procedures, the experimental data were taken from three papers: [4] (cell architecture variations), [5] (fuel composition variations), and [14] (oxidant composition variations). It was assumed that experimental result taken from both [4] and [14] were obtained from the same laboratory set. This assumption was made based on analysis of the cell voltage–current density ($E - i$) curve (H_2/Air, 800°C), which is presented as the same in both papers. The main parameters of the experimental data used for training procedures are listed in Table 5.2.

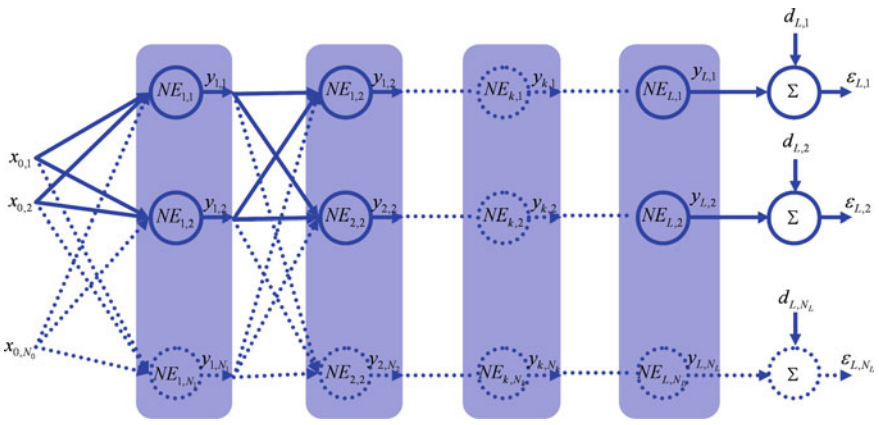

Fig. 5.17 Artificial Neural Network model

Table 5.2 Main parameters of experimental data used for training procedures

Experimental data source		Jiang et al.	Zhao et al.
Electrolyte	Temperature (°C)	800	550–800
	Thickness, μm	10	4–20
	Type	YSZ	YSZ/SDC
Anode	Thickness (mm)	1.1	0.5–2.45
	Porosity	0.54	0.48–0.76
	Type	n/a	Ni/YSZ
Cathode	Type	LSM	LSC/SDC
	Current Collector	n/a	LSC
	Thickness (μm)	50	n/a
Fuel	H_2 (ml/min)	30.8–140	300
	N_2 (ml/min)	0–109	0
Oxidant	O_2 (ml/min)	27.5–550	115
	N_2 (ml/min)	0–523	434
Area, cm^2		1.1	2

Data given in [4] contain mainly "architecture" parameters of the cell, whereas data given in [5] contain anode flow parameters. To make the model more general, data collected in [4] and [5] were merged into a database which was used to train the network with dependence on as many parameters as possible. The main differences between cells in [4] and [5] are listed in Table 5.2. Those parameters were not taken into consideration.

5.1.3.4 Training Procedures of the ANN

Usually, back-propagation is chosen as the learning process of the ANN. Back-propagation is the generalization of the Widrow–Hoff learning rule to multiple-layer networks and nonlinear differentiable transfer functions. The governing equations of the process are presented below.

$$s_{k,i} = \sum_{j=0}^{N_{k-1}} w_{k,i,j} \cdot x_{k,j} \tag{5.30}$$

$$y_{k,i} = f(s_{k,i}) \tag{5.31}$$

$$\varepsilon_{L,i} = d_{L,i} - y_{L,i} \tag{5.32}$$

$$\delta_{k,i} = \varepsilon_{k,i} \cdot \frac{\partial f(s_{k,i})}{\partial s_{k,i}} \tag{5.33}$$

$$\varepsilon_{k,i} = \sum_{N_{k+1}}^{m=1} \delta_{k+1,m} \cdot w_{k+1,m,i} \tag{5.34}$$

for $k = 1, 2, \ldots L - 1$

$$w_{k,i,j}^{n+1} = w_{k,i,j}^{n} + 2 \cdot \eta \cdot \delta_{k,i} \cdot x_{k,j} + \alpha \cdot (w_{k,i,j}^{n} - w_{k,i,j}^{n-1}) \tag{5.35}$$

where: η—learning rate; α—momentum parameter; for a description of the other parameters see Figs. 5.16 and 5.17.

Commercially available software [15] was used for the ANN calculations. The Levenberg–Marquardt algorithm was used to accelerate the training procedure.

One of the more adverse events occurring during the learning network is overfitting. This term means that the network closely resembles the model of the learner, but cannot generalize results. There are many ways to avoid this phenomenon, the most popular being:

- Timely arrest of the learning process (called early stopping),
- Application of learning algorithms that can generalize possible answers,
- Possible use of a small number of neurons and layers of the network so that it cannot be overtrained.

An overly complex network can be trained with extraordinary accuracy, which means that the network becomes noise dependent (overfitting). Overfitting means the network has memorized the training examples, but has not learned to generalize to new situations. If a small enough network is used, it has insufficient power to overfit the data. Thus, the simplest architecture of the network was found in each case so as to avoid overfitting.

The Levenberg–Marquardt algorithm can be used to accelerate the training procedure. An overly complex network can be trained with extraordinary accuracy, which means that the network becomes noise dependent (overfitting).

Further, optimal regularization parameters were applied in automated fashion (Bayesian). This approach does not require division of the database into two parts: training and testing. Bayesian regularization makes a model generalized, which is the main advantage of using this algorithm in the network teaching process. It means that the model can be validated by the same batches of data. The weights of the network were assumed to be random variables with specified distributions. The regularization parameters are related to the unknown variances associated with these distributions. Estimation of these parameters can be made using statistical techniques. A detailed discussion of the use of Bayesian regularization, in combination with Levenberg–Marquardt training, can be found in [16].

When using Levenberg–Marquardt training with Bayesian regularization, it is important to let the algorithm run until the effective number of parameters has converged. The training was stopped with the message "Maximum MU reached." This is typical, and is a good indication that the algorithm has truly converged. A detailed explanation of the training algorithm parameters can be found in [15].

Prior to network training the input parameters were conditioned to make the results more general. Usually, current is divided by cell area to make the results independent of the experimental probe. The same was done with volume flows of oxidant and fuel (see Fig. 5.18).

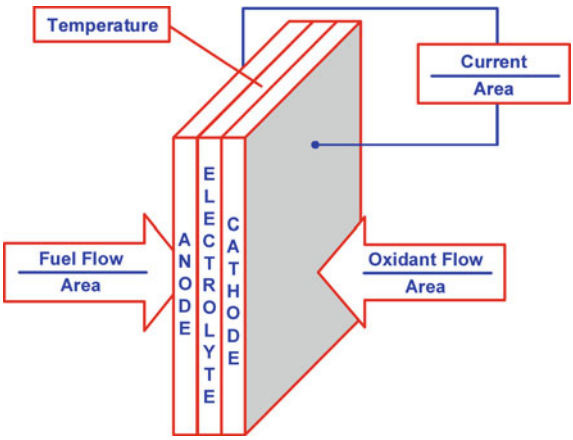

Fig. 5.18 The main input parameters of the ANN training procedure

The quantity of training epochs depends strongly on initial values of weight and input parameters. It is helpful to make the order of magnitude of input parameters similar to and comparable with the order of magnitude of the outlet parameters. To obtain relatively fast convergence, the temperature was reduced by a factor of 1000 (e.g. 800°C = 0.8) prior to network training: this reduces the training epochs from 600 k to 60 (10 k times); and volume flow densities were reduced by a factor of 100.

The network architecture is indicated in the following way: "number of inputs—number of neurons in the first layer— number of neurons in the second layer"; e.g. 9-7-1 means that the two-layer network consists of nine inputs, seven neurons in the first layer and one neuron in the second layer (the number of neurons in the last layer equals the number of outputs).

5.1.3.5 ANN as SOFC Model

There are many various parameters which can be modeled by ANNs and they are investigated one by one. Finally, the model of 13 input parameters was created, and additionally a few non-numerical parameters were added in hybrid-ANN model.

In total, 31 various voltage–current density curves (583 various experimental points—see Fig. 5.19) were used to train the network. The following network input parameters were used:

- Current density $(A/cm)^2$;
- Cathode inlet O_2 flow density $(ml/min/cm^2)$;
- Cathode inlet N_2 flow density $(ml/min/cm^2)$;
- Anode inlet H_2 flow density $(ml/min/cm^2)$;

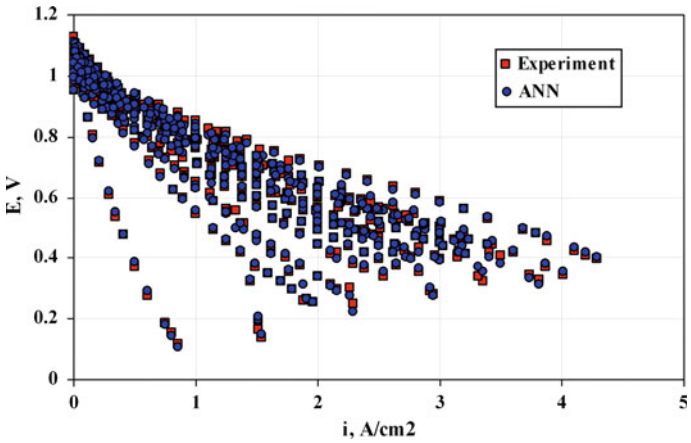

Fig. 5.19 All points used for network training (□) and ANN answers (◇)

- Anode inlet He flow density (ml/min/cm^2);
- Anode thickness (mm);
- Anode Porosity, unitless;
- Electrolyte Thickness (μm);
- Electrolyte Temperature (°C).

Cell voltage was the output parameter in each case, which means a singular neuron in the last layer. The numbers of neurons in the first layer as well as number of layers were increased until the network learned experimental data with an error level at below 1% (see Fig. 5.20).

Singular $E = f(i)$ Curve

The first case investigated was just a singular $E - i$ curve, which represents the simplest case of an SOFC model based on ANN.

The singular $E - i$ curve can be successfully modeled by a 1-2-1 network. The network had only one input parameter: current density, which was given in A/cm^2. The result of the training procedure is shown in Fig. 5.21. The network estimates the voltage of the cell with relative error of 0.7%.

Temperature Dependence

The experimental data of temperature dependence on the SOFC performance were taken from [4]. The network has two input parameters: current density (A/cm^2) and the cell temperature (°C). The minimum network architecture for this purpose is 2-3-1, which was taught with relative error of 0.7%. The result of the training

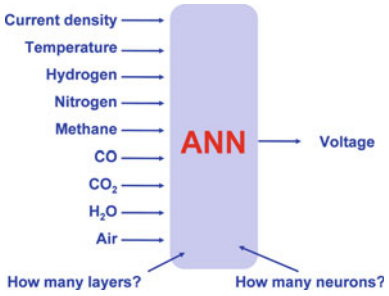

Fig. 5.20 Input parameters of ANN

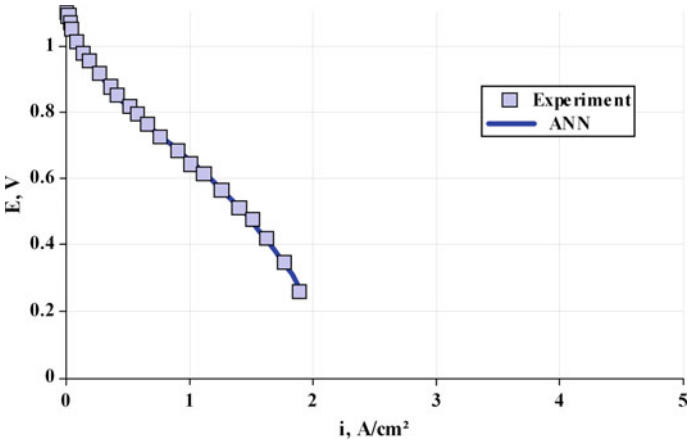

Fig. 5.21 Singular $E - i$ curve modeled by the 1-2-1 ANN for experimental data taken from [4]

procedure is shown in Fig. 5.22. The quality of the model was tested at four different temperatures 550, 650, 750 and 850°C). The network extrapolates the temperature dependence in a relatively regular way (see Fig. 5.22).

5.1.3.6 Electrolyte Thickness Dependence

SOFC electrolyte in the fuel cell forms a thin layer of varying thicknesses depending on the cell production technology and experience of the manufacturer. The most popular solutions lately is anode supported design with the electrolyte being a thinner element (see Fig. 5.23).

With existing experimental data the four current–voltage curves obtained for the same working conditions were selected. The thickness of the electrolyte was examined for the following size: 4, 8, 15 and 20 µm. Experimental data of the electrolyte thickness dependence on solid oxide fuel cell performance were taken

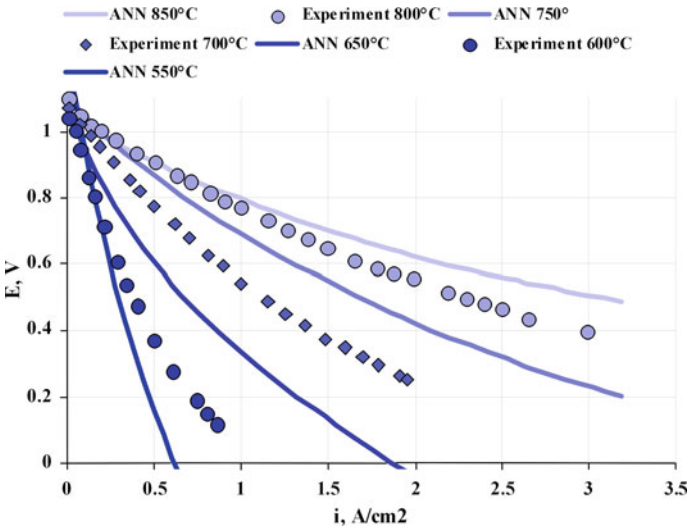

Fig. 5.22 Temperature dependence modeled by the 2-3-1 ANN for experimental data taken from [4]

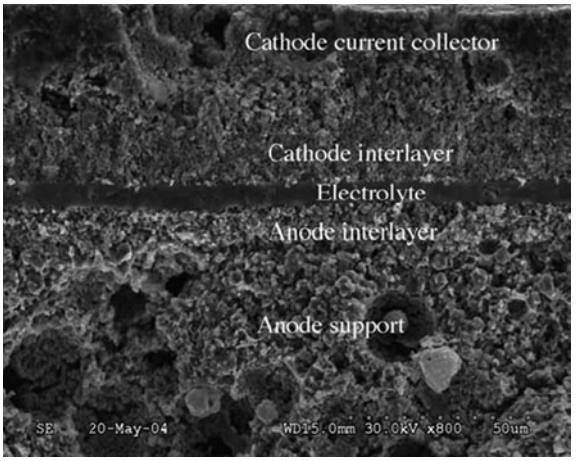

Fig. 5.23 Anode supported cell cross section [4]

from [4]. The network has two inlet parameters: current density, A/cm^2; and the electrolyte thickness, μm. A 2-3-1 network is the minimum network architecture allowing a reasonable level of relative error (0.7%).

The result of the training procedure is shown in Fig. 5.24. Three various electrolyte thicknesses were tested to check the network modeling quality. In fact, the change in electrolyte thickness has little impact on cell voltage. Consequently, there is limited impact when testing values of electrolyte thickness. The ANN gives few inaccurate results as regards extrapolation, where the model estimates

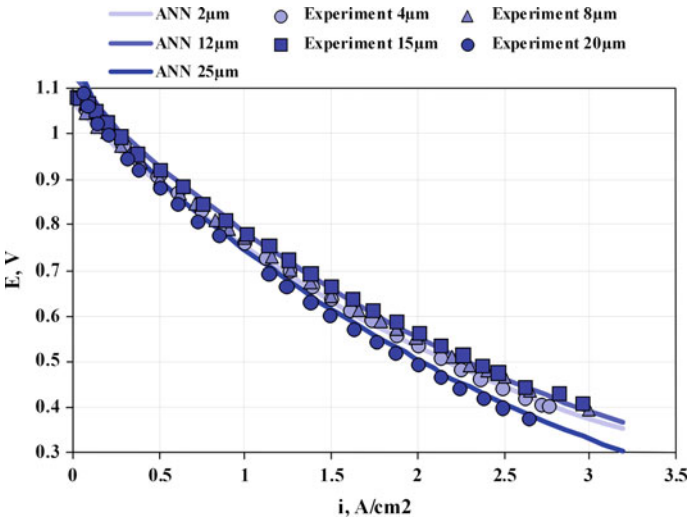

Fig. 5.24 Electrolyte thickness dependence modeled by the 2-3-1 ANN. Experimental data were taken from [4]

higher voltage for electrolyte thickness of 25 μm than for the electrolyte thickness of 20 μm (see Fig. 5.24).

5.1.3.7 Anode Thickness Dependence

The most often used solution is anode supported architecture (see Fig. 5.23), which results in anode thickness being much greater than the other layers. The available experimental data contain four current–voltage curves for the teaching. These curves were collected for the following anode thicknesses: 0.5, 1.0, 1.45 and 2.45 mm.

Experimental data of anode thickness dependence on solid oxide fuel cell performance were taken from [4]. The network has two inlet parameters: current density, A/cm^2; and the value of anode thickness, mm. A 2-2-1 network is the minimum network architecture allowing a reasonable level of relative error (0.4%). The result of the training procedure is shown in Fig. 5.25. Three various anode thicknesses were tested to check the network modeling quality. The network was observed to model the voltages appropriately.

5.1.3.8 Anode Porosity Dependence

The available experimental data contain four current–voltage curves for the teaching effect regarding porosity of the anode layer. These curves were collected for the following anode porosities: 0.32, 0.48, 0.57 and 0.76. The porosity

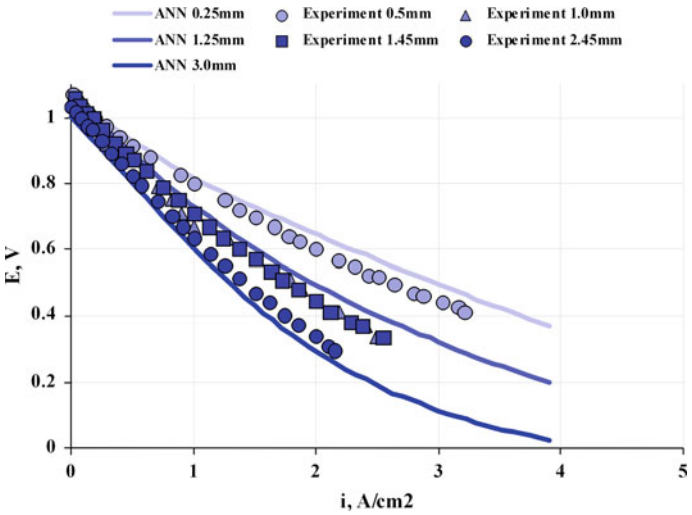

Fig. 5.25 Anode thickness dependence modeled by the 2-2-1 ANN. Experimental data were taken from [4]

measurement method was based on the Archimedes method and is described in detail in [4].

Experimental data of anode porosity dependence on solid oxide fuel cell performance were taken from [4]. The network has two inlet parameters: current density, A/cm^2, and anode porosity. A 2-5-1 network is the minimum network architecture allowing a reasonable level of relative error (0.3%). The result of the training procedure is shown in Fig. 5.26. The network was tested for three different anode porosities to check the network modeling quality. The network was observed to model the voltage appropriately.

5.1.3.9 Fuel Composition Dependence

Several various compositions were used for training and testing the ANN-based models of SOFC.

$H_2 + H_2O$: The influence of a mixture of hydrogen and steam as a fuel for fuel cell is the most basic characteristic of the fuel which can be made. Steam is one of the products formed during fuel cell work at anode side and consequently, its influence is very important (Fig. 5.27).

Among the data collected, the impact of steam content at anode side on fuel cell voltage is included in the following publications: [5, 8, 17]. The network has three inlet parameters: current density (A/cm^2); hydrogen flow density (ml/min/cm^2); and steam flow density (ml/min/cm^2). Five various data set were used for training procedures, and a 3-3-1 network gives acceptable error (1.4%). The model was tested for other data then used during training, and the next four curves were

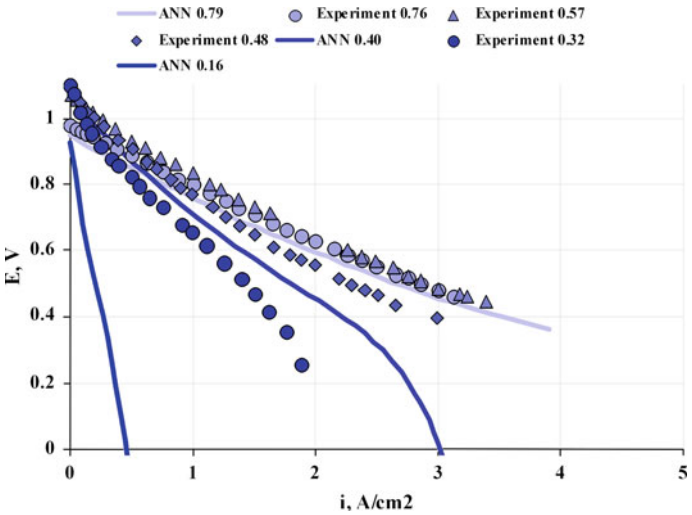

Fig. 5.26 Anode porosity dependence modeled by the 2-5-1 ANN for experimental data taken from [4]

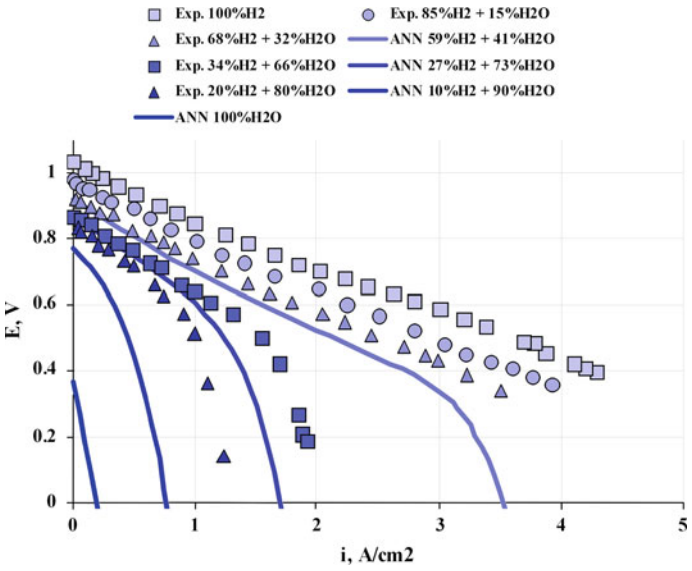

Fig. 5.27 Result of the 3-3-1 network simulation training data of H_2/H_2O (at constant flow rate of 127 ml/min/cm^2) taken from [5]

generated. With interpolation (e.g. 59% H_2), the model gives very accurate results. With extrapolation, the result for 10% H_2 can be accepted, whereas for 0% of H_2 the network gives a nonphysical result (generates current with no fuel delivered).

$H_2 + N_2$: The influence of inert gases at anode side was investigated for two diluents: N_2, and He.

Experimental data for training purposes of N_2 dependence on solid oxide fuel cell performance were taken from [5]. The network has three inlet parameters: current density (A/cm^2); hydrogen flow density (ml/min/cm^2); and nitrogen flow density (ml/min/cm^2). A 3-3-1 network is the minimum network architecture allowing a reasonable level of relative error (1.4%). The result of the training procedure is shown in Fig. 5.28. Three different fuel compositions were tested to check the network modeling quality. The ANN gives inaccurate results only for no hydrogen flow (0 ml/min), where it gives E_{OCV} = 0.6 V; fortunately the curve rapidly decreases to negative voltages. Other fuel compositions seem to be modeled acceptably by the network.

$H_2 + He$: A 3-3-1 neural network is the minimum configuration that gives a model that generates simulation results of fuel composed of hydrogen and helium with an accuracy of 1.3%. The network was tested for four data sets other than used during training, the results of the testing procedures are shown in Fig. 5.29. Similary to N_2, the network gives acceptable results for interpolations.

$H_2 + CO$: SOFC is often fed by a mixture of different compounds resulting from the processes of steam reforming of methane. Apart from diluents, the influences of other fuels at anode side on the quality of the ANN-based model were tested.

Figure 5.30 shows dependence of a fuel composition containing a mixture of hydrogen and carbon monoxide modeled by a 3-2-1 network; the training data also

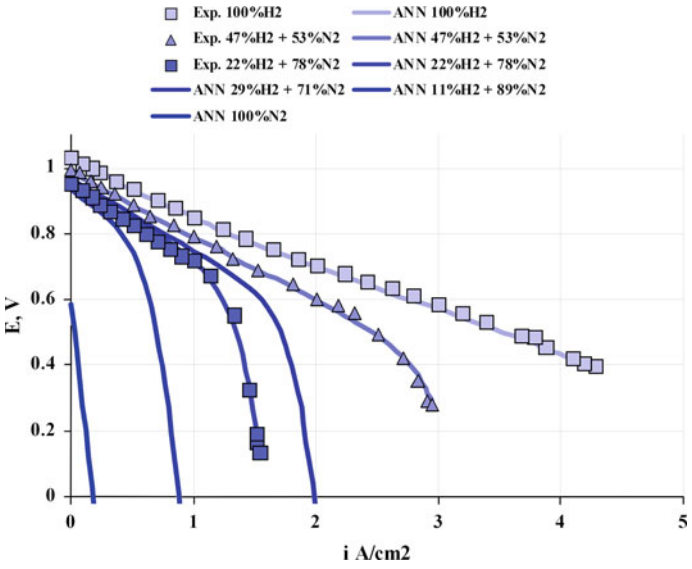

Fig. 5.28 Result of the 3-3-1 network simulation training data of H_2/N_2 (at constant flow rate of 127 ml/min/cm^2) taken from [5]

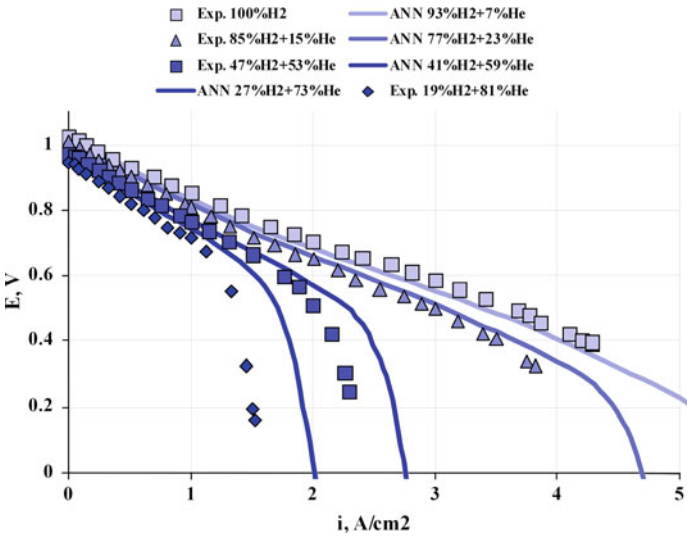

Fig. 5.29 Result of the 3-3-1 network simulation training data of H_2/He (at constant flow rate of 127 ml/min/cm^2) taken from [5]

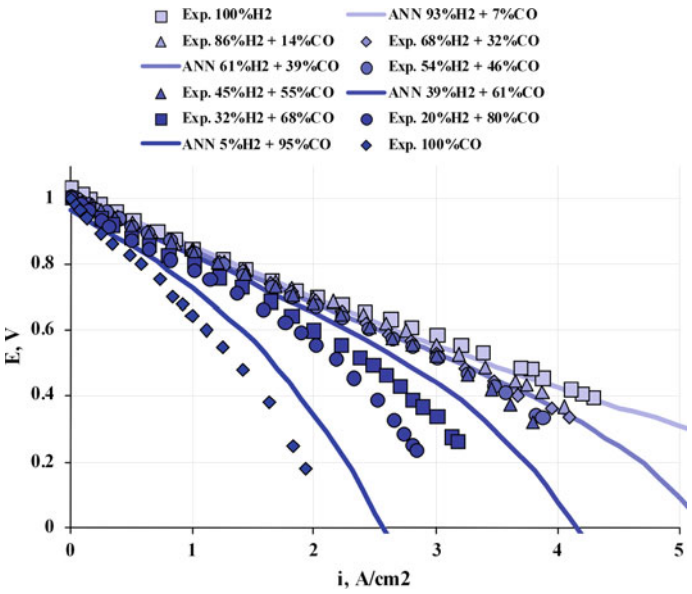

Fig. 5.30 Result of the 3-2-1 network simulation training data of H_2 and CO (at constant flow rate of 127 ml/min/cm^2)

contained dry hydrogen and dry carbon monoxide. It should be noted that the presented experimental data are in the carbon deposition region (s/c ratio = 0!), and the cell probably will not operate at those conditions in the long run.

$H_2 + CO_2$: Carbon dioxide is neither a fuel nor a diluent (it can react with hydrogen and causes carbon deposition).

Figure 5.31 shows a dependence of fuel composition containing a mixture of hydrogen and carbon dioxide modeled by a 3-2-1 network, the training data also contained dry hydrogen and dry carbon monoxide.

$CO + CO_2$: Simultaneous effects of carbon monoxide and carbon dioxide on voltage generated by the cell can be successfully achieved with the ANN model of 3-4-1 configuration, achieving an average error between the results of the model and the experimental data of 1.3%. Here, the same note is valid as for two previous results given, that fuel cell for those inlet composition works in carbon deposition region. Even for higher currents there is no steam generated, which may avoid cell degradation (Fig. 5.32).

5.1.3.10 Oxidant Composition Dependence

The most commonly used oxidant in SOFC is air. Air is composed primarily of nitrogen and oxygen, but as oxidant the mixture of N_2 and O_2 in different proportions was used in the networks' learning processes.

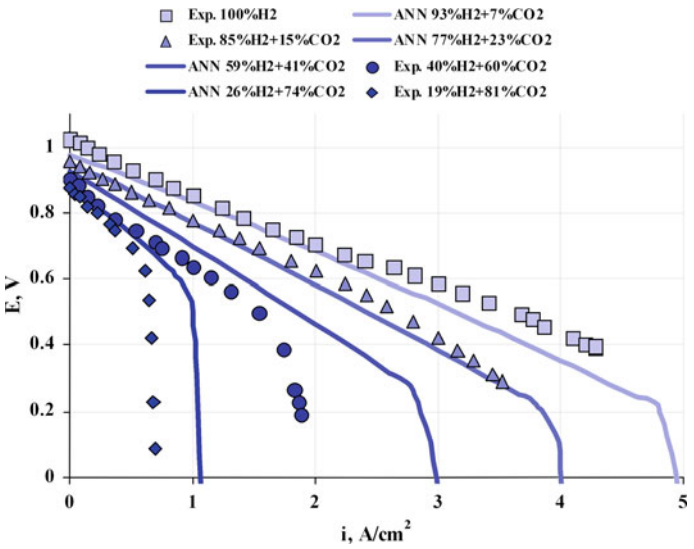

Fig. 5.31 Result of the 3-2-1 network simulation training data of H_2 and CO_2 (at constant flow rate of 127 ml/min/cm^2)

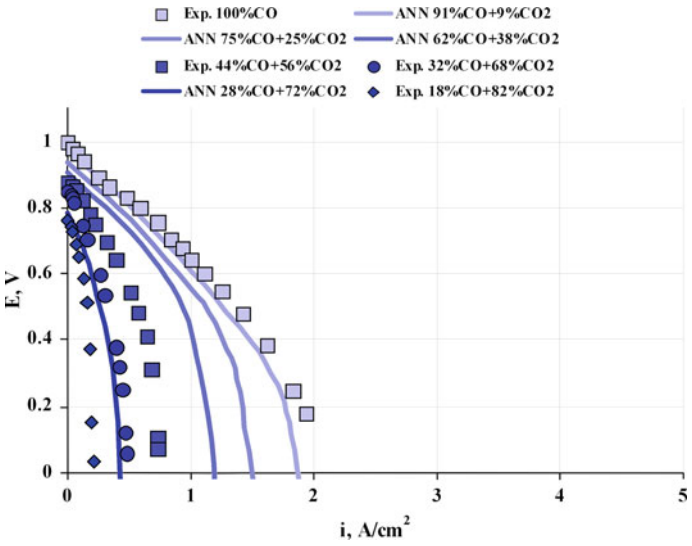

Fig. 5.32 Result of the 3-4-1 network simulation training data of CO and CO_2 (at constant flow rate of 127 ml/min/cm^2)

Experimental data of oxidant composition dependence on solid oxide fuel cell performance were taken from [14]. The network has three inlet parameters: current density, A/cm^2; oxygen flow density (ml/min/cm^2); and nitrogen flow density (ml/min/cm^2). A 3-5-1 network is the minimum network architecture allowing a reasonable level of relative error (2.1%). Two oxidant compositions were tested to check the network modeling quality. Oxidant composition dependence seems to be modeled acceptably by the network. The network was also tested for 0%O_2 and 100%N_2 but it gave negative voltages for all current densities analyzed (Fig. 5.33).

5.1.3.11 Hybrid-ANN Models

Parameters previously tested do have their own numerical representation, but there are SOFC features that either cannot to be expressed in numerical form or can only be expressed with great difficulty, i.e. electrolyte material, anode material, cathode material, cell type (planar, tubular), etc. In those situations a hybrid model can be applied which consists of the ANN model and additional mathematical expressions (hybrid model means a combination of known relationships and an ANN-based model). For instance, there are two options for accommodating the material type of electrolyte in an ANN-based model:

- To use a separate input to the model for each type of electrolyte used, it may be entering a 0/1 or the corresponding numerical value, for example the thickness of the layer;

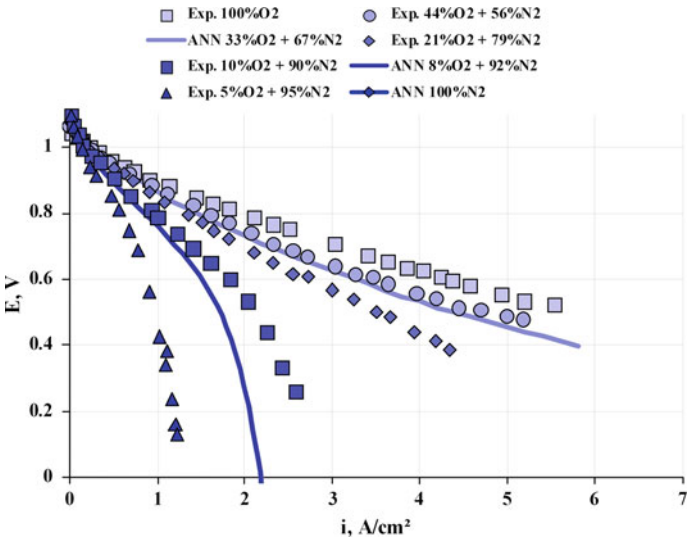

Fig. 5.33 Oxidant composition dependence modeled by the 3-5-1 ANN. Oxidant flow was kept at a constant value of 500 ml/min/cm^2. Experimental data were taken from [14]

- The use of a hybrid model, i.e. as an input to the model given electrolyte ionic conductivity calculated from the available dependency or resistance to ions through the electrolyte.

The first method increases the number of inputs of the model by the number of experimentally available types of electrolytes. In this solution, it is difficult to talk about any extrapolation of results. In practice, electrolytes materials other than those which were taken into account during the training process cannot be modeled. But, it seems relatively easy to make an interpolation; an electrolyte composed of many layers can be modeled by having experimental data collected separately for each type.

In the second method, some additional relationships are added to the model based on known conductivity formulas. Thus, it becomes possible to model electrolytes which were not used in the experiments but whose conductivity is known. On the other hand, it appears difficult to incorporate multi-layered electrolytes due to the difficulty in encompassing all the layers in the mathematical description.

The hybrid model allows for the use of fewer inputs in the model and the modeling of various electrolytes for which there was no experimental data. In turn, a model based solely on the artificial neural network would permit the modeling of multi-layer electrolytes. The hybrid model is used to model the impact of the type of electrolyte; in this case the number of neural network inputs (temperature, thickness of the electrolyte and the electrolyte material) can be reduced to one, expressed resistance of the electrolyte, while the overall quantity of inputs to the hybrid model remains unchanged.

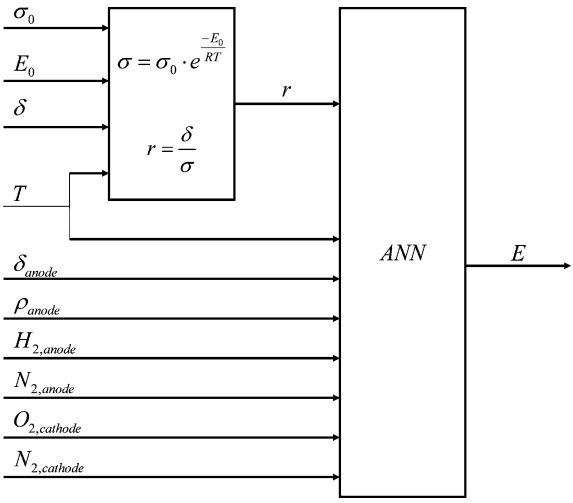

Fig. 5.34 Hybrid-Artificial Neural Network model

The hybrid model consists of the ANN model and mathematical expressions as shown in Fig. 5.34. The ionic conductivities of solid oxides as adequate equations (5.23) were applied, and the adequate factors for those equations are shown in Fig. 5.9.

5.1.3.12 Discussion

The presented results show that the influences of temperature, electrolyte thickness, anode thickness, anode porosity, fuel composition and oxidant compositions can be successfully modeled by an ANN. A relatively complex model of an SOFC can be modeled by a very simple ANN. The ANN generalizes SOFC behaviors across a relatively wide range of conditions—in some cases even an extrapolation mode is available. A 9-7-1 ANN can predict SOFC behavior dependent on nine various parameters, including working parameters (temperature, fuel composition, oxidant composition) and architecture parameters (electrolyte thickness, anode thickness and porosity). The relatively low number of neurons used does not allow overfitting of the network, as is indicated by proper accordance in both interpolation and extrapolation of the experimental data. The model can be implemented easily in commonly available software and/or in any other programming language.

A summary of the networks used is presented in Table 5.3. From use of ANN based models, both standard and hybrid, and based on investigations made, the following general conclusions can be drawn:

- In some cases extrapolation is allowed;
- No adequate amount of experimental data produces large mismatches in the results given;
- Inputs which are very far away from experimental data can generate nonphysical results;

Table 5.3 Main parameters of trained networks

Dependence	Number of inputs	Number of neurons in the first layer	Number of neurons in the second layer	Relative error (%)	Quantity of experimental Points
Singular $E - i$curie	1	2	1	0.7	23
Temperature	2	3	1	0.7	62
Electrolyte thickness	2	3	1	0.7	104
Anode thickness	2	2	1	0.4	102
Anode porosity	2	5	1	0.3	103
Fuel compositions(two components)	3	3	1	1.3–1.4	154–185
Oxidant Compositions (two components)	3	5	1	2.1	161
All investigated parameters	9	7	1	1.0	583
	10	3	1	1.4	677
	11	3	1	2.8	813
	12	3	1	3.1	971
	13	4	1	2.7	1026
Hybrid model	15	4	1	3.5	1026

- Back-propagation algorithm can be successfully used as the training procedure;
- The influences of temperature and fuel composition can be successfully modeled by the ANN of 9-4-3-4-1 architecture (21 neurons in total);
- ANN-based SOFC model can be used for both cell and system simulations with timeless convergence;
- ANN enables the simulator to adapt to new data—e.g. degradation.

Utilization of (H-)ANNs for modeling the singular SOFC looks a very promising way of obtaining an advanced model of SOFC and matches experimental data with little error—results derived from the (H-)ANN based SOFC model very closely match the experimental data and other working environments. This means that the model predicts SOFC performances for various working conditions. The model based on (H-)ANN is very useful for rapid calculation of SOFC values, e.g. dynamic simulations, because it does not require iterations during the calculations. The (H-)ANN based SOFC model can be used for both cell and system simulations with timeless convergence. The model can be used in control and monitoring of the real system to predict performance before changing the control parameters.

5.2 Fuel Cell Module

The singular fuel cell is characterized by relatively low voltage in the range from 1.1 to 0.4 V. Those values are very impractical, and cells are connected in series to obtain more convenient voltages ($\approx$100 V). This construction makes a fuel cell

stack, which cannot work completely alone, and other devices are required for proper operation. The auxiliary devices together with the stack make up a fuel cell module. The fuel cell module is a basic element, characterized by independent operation.

An example of an SOFC Module proposed by Siemens is shown in Fig. 5.35. The module is composed of the following main devices:

- Fuel cell stack,
- Combustion chamber,
- Recycle plenum,
- Ejector,
- Pre-reformer, and
- Heat exchanger.

The SOFC module is fed by methane rich natural gas. Methane is supplied from the network to an ejector inside, mixed with anode recycle and increased in pressure and this mixture is directed into a pre-reformer. Inside the pre-reformer the conversion of hydrocarbons into hydrogen begins. From there, the gas mixture is directed to the anode channel of the fuel cell stack. At the anode, following further reforming of methane and carbon monoxide to hydrogen, hydrogen ions combine with $O^{=}$ to create water vapor and release electrons which flow up the external electric circuit. Then, the mixture of gases (with the lower content of methane and hydrogen) is directed to a recycle plenum. In the recycle plenum one part of the gas is directed to the ejector and the other part to the combustion chamber. Gas recirculation is associated with the processes involved in the reforming of methane. The second part of the anode gas is directed into the combustion chamber where it is mixed with air. Previously un-oxidized gases

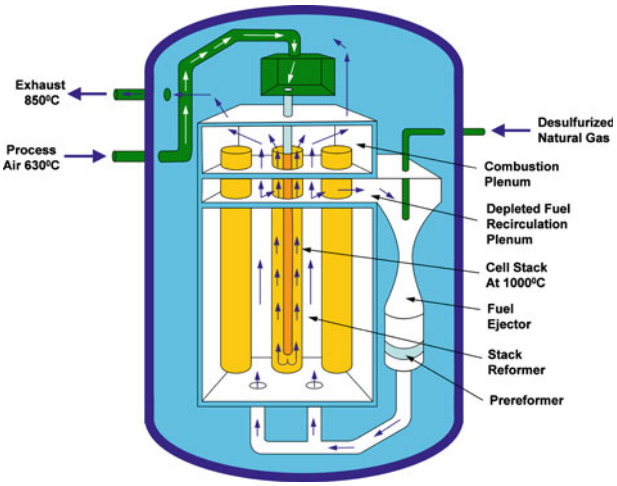

Fig. 5.35 Siemens–Westinghouse SOFC module [48]

(methane, hydrogen, carbon monoxide) are now burned before leaving the fuel cell module. Circulation in the anodic gas flow is enforced by either an ejector powered by methane from the grid at a relatively high pressure or a μ-fan. The air flow through the cathode channels is forced by an external compressor which does not form part of the fuel cell module.

The air, mostly from behind the compressor, is directed to a regenerative heat exchanger inside the fuel cell module. Then air taken from the pipe system passes through the combustion chamber and the recycle plenum, entering the cathode side of the fuel cell stack. An outlet of the cathode ends in the combustion chamber, where the air mixes with the anodic gases.

Electricity generated by the entire SOFC module is determined by the following equation:

$$P_{\mathrm{SOFC}} = \sum_{j=1}^{m} \left(I_j \cdot \sum_{k=1}^{n} E_{\mathrm{SOFC,\,k,\,j}} \right) \tag{5.36}$$

5.2.1 Fuel Cell Stack

The fuel utilization factor of fuel for each stack depends on the load and the number of cells in the stack. In general, in a series connection of stack cells, the current flowing through each cell has the same value. The relationship for computing the fuel utilization of the stack is given by the following equation:

$$\eta_f = \frac{\eta_{f,\,\mathrm{stack}}}{n - \eta_{f,\,\mathrm{stack}} \cdot (k-1)} \tag{5.37}$$

In fact, the relation (5.37) ignores the resistance R_2. During real calculations, the fuel utilization factor should be calculated iteratively. The value of current density is the same for each of the cells connected in series.

5.2.2 (Pre-)Reformer

Methane can be reformed into hydrogen in several ways. One method is steam reforming, which is based on methane decomposition to carbon monoxide and hydrogen, and the water gas shift process which is based on the further decomposition of the water molecule and the composition of carbon dioxide:

$$\mathrm{CH_4 + H_2O \rightarrow 3H_2 + CO} \tag{5.38}$$

$$\mathrm{CO + H_2O \leftrightarrow H_2 + CO_2} \tag{5.39}$$

Table 5.4 Factors used for steam content determination to avoid carbon deposition

Fuel type	Factor name and reference	Definition (by molar fractions)	Value assumed during calculations
CH_4, CO	Steam to carbon ratio [36]	$\frac{H_2O}{CH_4 + CO}$	1.4
Methanol	Steam to methanol ratio [45]	$\frac{H_2O}{CH_3OH}$	1
Ethanol	Steam to ethanol ratio [46]	$\frac{H_2O}{C_2H_5OH}$	3

Overall, steam methane reforming reactions (5.38 and 5.39) are endothermic in summary with the heat process dependent on the reaction temperature: ΔH = 165–247 kJ/mol (see 4.2 and 4.3 for details). It means that thermal energy is converted into the form of fuel (mainly water molecule decomposition into hydrogen).

Carbon deposition is a harmful process that causes very rapid degradation of fuel cells and the reformer. For safe fuel cell operation, steam is added to carbon-containing fuels to prevent carbon deposition on the cell surfaces. Various kinds of factors are used to describe adequate steam content in hydrocarbon fuel to avoid carbon deposition. For gaseous hydrocarbon fuel, the most commonly used factor is the steam-to-carbon ratio (s/c ratio). Mostly, the s/c ratio is set at about 2 and above this value no carbon deposition takes place. Boundary values of the s/c ratio are dependent on temperature. Drawn from a review of the literature, typical factors and their definitions for various fuels are listed in Table 5.4.

The s/c ratio at which no carbon deposition occurs is temperature dependent, as shown in Fig. 5.36.

If fuels other than methane are delivered, there are other factors which define adequate steam content during reforming processes. Exemplary data for methanol and ethanol are presented in Figs. 5.37 and 5.38, respectively.

5.2.3 *Anode Recycle*

The steam needed for reforming processes is delivered by looping in part of the anode gas. Usually, the amount of recycled gas is varied to achieve a constant steam-to-carbon ratio, and the recycle ratio is defined by the following equation:

$$\eta_{\text{recycle}} = \frac{m_{m_{\text{recycled}}}}{m_{\text{anode, out}}} \tag{5.40}$$

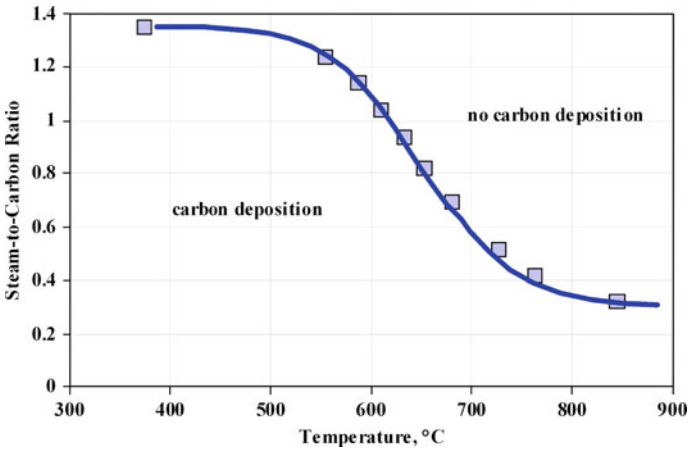

Fig. 5.36 Minimum temperature and corresponding required ratios of steam-to-carbon (s/c ratio) above which no carbon deposition occurs thermodynamically [36]

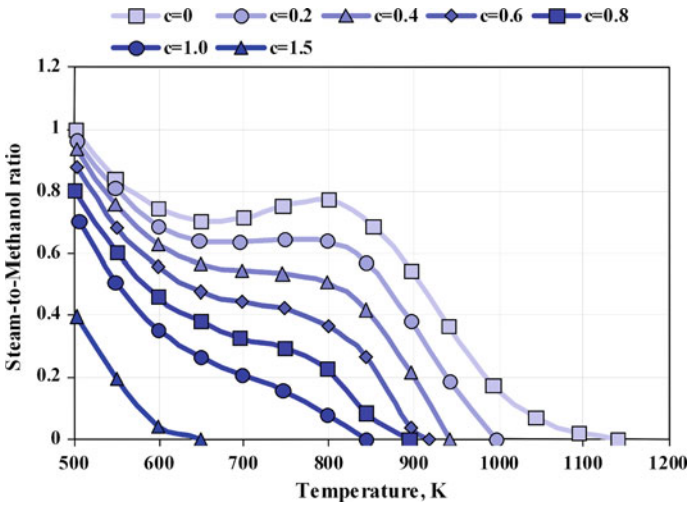

Fig. 5.37 Minimum temperature and corresponding required ratios of steam-to-methanol (S/MeOH) above which no carbon deposition occurs [45]

Mainly, the re-circulation is forced by the ejector, in which the working medium is a fuel (methane) supplied to the system (Fig. 5.35). The presence of the ejector substantially restricts the range of possible operating conditions.

The design and off-design performance evaluation of an anodic recirculation system based on ejector technology for solid oxide fuel cell hybrid system

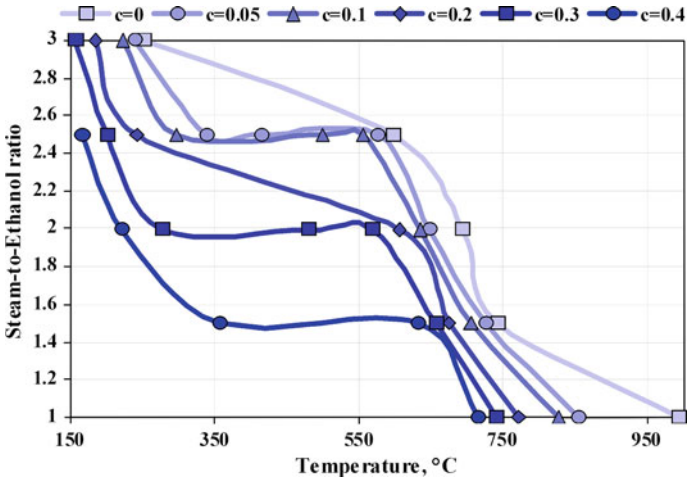

Fig. 5.38 Minimum temperature and corresponding required ratios of steam-to-ethanol (S/EtOH) above which no carbon deposition occurs [46]

application was done by Marsano et al. [18] and Ferrari et al. [19]. They found that the ejector has no stable characteristics during off-design operation and additionally, it demands high methane pressure level for proper operation. If methane is not delivered through an external pipeline, a methane compressor is needed. They found that the off-design performance of the anodic recirculation system integrated with the SOFC could be crucial during system operation. A variable fuel utilization factor brings the steam-to-carbon ratio close to its lower limit, which could be dangerous for the fuel cell stack and the reformer. Additionally, use of an ejector to force anode gas recirculation entails the following difficulties:

- Inability to control gas recirculation flow, as it relates to the specified quantity of fuel, which in turn sets the power system,
- Extremely difficult start-up and shutdown operations, during which fuel cell maintenance requires continued recirculation by other means than the ejector,
- Inability to operate fuel cells in distributed generation systems using natural gas directly from the public network, due to the very low gas pressure available (close to zero). Pressure of 9–15 bar is required for the working fluid of the ejector to enforce and maintain recirculation in the fuel cell channels of the stack,
- Low load of the SOFC Module requires a reduction in fuel supply, which decreases anode gas recirculation.

Gas velocities at anode side are relatively low, which means low pressure drops across anode channels. Pressure drop values of 1–1.5% have been found [18].

High pressure inside SOFC–M increases fuel cell efficiency as well as the installation cost of air compressor and gas turbine devices. A technical-cost analysis provides the adequate pressure ratio for the SOFC–GT hybrid system. Most advanced SOFC–Ms work at pressures of around 9 bar, giving pressure drops across anode channels of between 0.09 and 0.135 bar. In those cases, the range of the "pressure ratio" of the ejector is from 1.01 to 1.015. These values are relatively low, meaning that theoretically it is possible to use a compressor/fan instead of an ejector. The temperature of the recycle fluid is high (800°C), which will probably present additional difficulties.

5.2.3.1 μ-Fan

The essence of using the μ-fan is to use a fan to force the flow of gases directly into the recirculation system. The advantages are as follows:

- Recirculation is independent of the quantity of fuel injected gas, controls the parameters of the recycle gas stream easily and takes optimization of the work cell into account,
- Ability to sustain recycling, even without a working gas (fuel),
- Ability to work with very low fuel cell load (even at zero),
- Ability to generate electricity in a range from zero to full power,
- Easy to start up and shut down fuel cells in distributed generation fueled directly from a low-pressure gas supply network.

There are two ways to input the fuel (methane) into the stack: fuel is inserted before μ-fan or after it. The first gives a lower temperature of inlet gas to μ-fan, the second one gives a lower mass flow through this device. When methane is injected before μ-fan the work demanded by the external fuel compressor decreases by 24% compared with the ejector based solution. The work demanded by the μ-fan together with fuel compressor work means a total decrease in consumed work of about 9%. When methane is injected after μ-fan the work demanded by the fuel compressor decreases by 23%. Together works demanded by the μ-fan and fuel compressor decrease the work needed to deliver by about 8%.

The μ-fan operates in a reduced environment and at high temperatures, which will probably present additional difficulties. The concept for technical realization of this device is shown in Fig. 5.39. The μ-fan is driven by an external rotating electromagnetic field, which enables control of part of the recycle flow.

Design point as well as off-design operation of the μ-fan can be modeled in a similar way to the compressor (see Sect. 5.3.3). The efficiency benefits of using a μ-fan are relatively small. A better solution is to apply methane injection before the μ-fan, which decreases the demand for electricity by about 9%. It delivers almost the same total efficiency of the SOFC–M. If the μ-fan has higher adiabatic efficiency, marginally higher total efficiency can be achieved—the

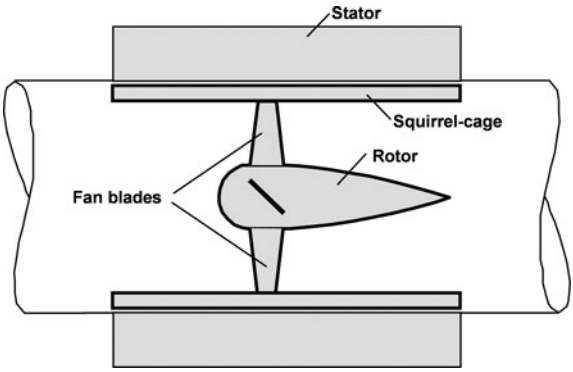

Fig. 5.39 Scheme of μ-fan driven by external rotating electromagnetic field

influence of μ-fan efficiency is negligible from the whole system efficiency point of view.

From a thermodynamic point of view the hybrid system with SOFC should operate at higher pressures than the systems currently in use. The optimal pressure ratio for TIT = 1160°C is 18 [20]. Evidently, increasing the SOFC Module operating pressure means higher installation costs. Increasing the working pressure of the SOFC Module to 18 bar causes efficiency to rise to 65% (5% higher). In this case the pressure of inlet gas to the ejector is about 24 bar. The use of the μ-fan in this case results in a fall in electricity consumption of about 22%.

CFD based simulations have been done to estimate the technical solution of the μ-fan, and the resulting design is shown in Figs. 5.40 and 5.41.

5.2.3.2 Ejector

The aim of using the ejector is to raise its inlet gas pressure (anode) by utilizing a stream of working fluid (fuel), but the degree of compression must be sufficiently large to force the anode gas recirculation in the channels of the fuel cell stack. The effectiveness of suction and compression of anode gases depends on the mass flow of the injected fuel. The algorithm given in [21] can be used to describe the behavior of this element during off-design operation (Fig. 5.42).The ejector model has the following input parameters:

- Inlet pressure of stream to be compressed —anode off-gas pressure (p_z),
- Inlet pressure of working fluid—methane inlet pressure (p_r),
- Mass flow of stream to be compressed—anode off-gas mass flow (m_z),
- Mass flow of working fluid—methane inlet mass flow (m_r),
- Temperature of working fluid—methane inlet temperature (t_r),
- Temperature of stream to be compressed—anode off-gas temperature (t_z),
- Cross section areas: the diffuser, mixing chamber, and confuser.

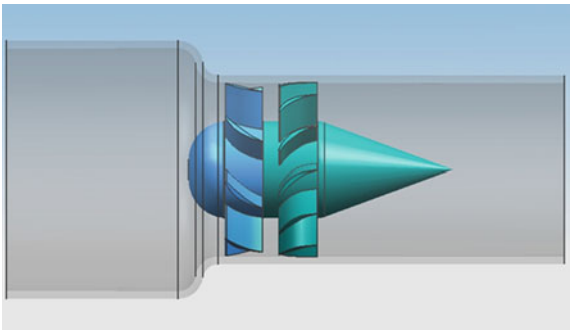

Fig. 5.40 3D view of a possible μ-fan

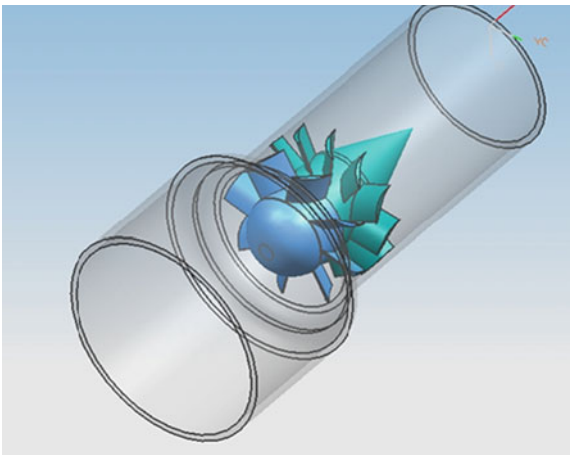

Fig. 5.41 3D view of a possible μ-fan

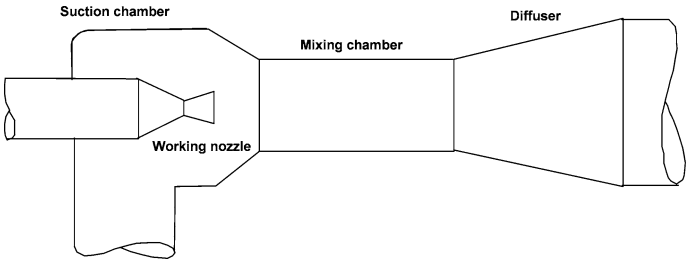

Fig. 5.42 Ejector scheme

The main parameter characterizing ejector operation is the ejection ratio given by the following formula:

$$u = \frac{m_z}{m_r} \tag{5.41}$$

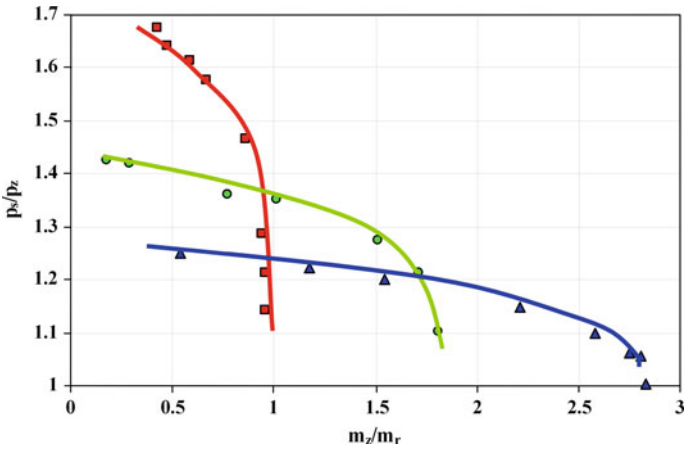

Fig. 5.43 Off-design performance curves of three different ejectors

In cases of an ejector installed inside an SOFC–M, the nominal value of this parameter is roughly 4.

Ejector outlet pressure is given by the following equation:

$$p_s = p_z + \Delta p_s \tag{5.42}$$

The difference between ejector inlet pressure and outlet pressure is given by the relationship [21]:

$$\Delta p = \frac{\left(K_1 \cdot a_{rm} \cdot \lambda_{r_2} + u \cdot K_2 \cdot \sqrt{2 \cdot g \cdot v_z \cdot \Delta p_k}\right)^2}{2 \cdot g \cdot v_s \cdot K_3^2 \cdot (1+u)^2} \tag{5.43}$$

Adequate factors of Eq. 5.43 ($K_1\, K_2\, K_3$) are depend on ejector geometry and define ejector performances.

Figure 5.43 shows a few of the ejector characteristics generated by the presented model and adequate experimental data for validation purposes.

Research into efficient and reliable control systems for the SOFC–GT hybrid system is still ongoing. Use of a μ-fan instead of an ejector could deliver more accurate control of processes inside the SOFC–M through varying the rotational speed of the μ-fan . In this case, lower mass flow of fuel (during part load operation) will not affect the stack working conditions, and the lower pressure ratio of the gas turbine subsystem will not affect the recycle ratio.

5.2.4 Heat Exchanger

5.2.4.1 Design Point

A heat exchanger is a device which transfers heat from one fluid to another. A basic diagram of a heat exchanger is shown in Fig. 5.44, fluid on the hot side of the heat exchanger warms fluid on the cold side. Generally, there are three main designs of heat exchangers:

- Co-flow,
- Counter-flow, and
- Cross-flow.

The most efficient heat exchangers have a counter-flow design. During design point calculation only the following values are required: heat exchanger effectiveness and pressure drops. Heat exchanger effectiveness is defined by the following relationship:

$$\eta_{\mathrm{HX}} = \frac{T_{\mathrm{outlet,\ cold}} - T_{\mathrm{inlet,\ cold}}}{T_{\mathrm{inlet,\ hot}} - T_{\mathrm{inlet,\ cold}}} \tag{5.44}$$

Heat exchanger effectiveness varies in a range from 0 to 1, the higher value meaning more heat transferred and simultaneously a larger heat exchanger area (higher costs). The definition of heat exchanger effectiveness is based only on its inlet and outlet parameters. In cases with state changes (evaporation, condensation) it is necessary to check that there is no temperature crossover during the heat

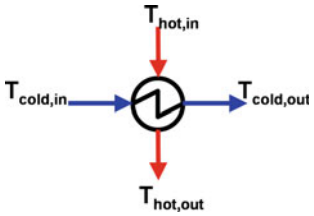

Fig. 5.44 Basic diagram of a heat exchanger

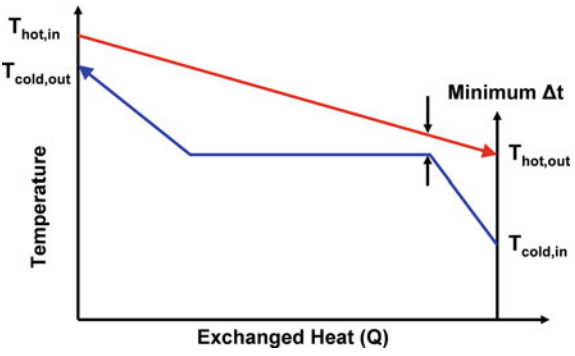

Fig. 5.45 Typical T–Q diagram of heat exchange process during evaporation (cold stream)

exchange. Adequate temperature-heat exchange (T–Q) diagram must be prepared (see Fig. 5.45). The lowest distance between the hot and cold side (minimum Δt) is called the "pitch point" or "minimum approach". Those values vary from a few degrees to hundreds of degrees.

During design point calculation, pressure drop across the heat exchanger can be kept at a constant value and is defined by the following coefficient:

$$\xi_{\mathrm{HX}} = \frac{\Delta p}{p_{\mathrm{inlet}}} \tag{5.45}$$

The heat exchanger outlet pressures can be calculated by the formula:

$$p_{\mathrm{outlet}} = p_{\mathrm{inlet}} - \Delta p \tag{5.46}$$

5.2.4.2 Off-Design Operation

During off-design operation calculations, temperatures of fluids can be calculated based on Backman's equation for known mass flows at heat exchanger inlets. Cold stream temperature can be estimated at the heat exchanger outlet ($T_{\mathrm{outlet,\ cold}}$) by the following equation:

$$\frac{\Phi}{\Phi_0} = \frac{T_{\mathrm{outlet,\ cold}} - T_{\mathrm{inlet,\ cold}}}{T_{\mathrm{inlet,\ hot}} - T_{\mathrm{inlet,\ cold}}} \tag{5.47}$$

where:

$$\frac{\Phi}{\Phi_0} = \left(\frac{m_{\mathrm{hot}}}{m_{\mathrm{hot,\ 0}}}\right)^{u_1} \cdot \left(\frac{m_{\mathrm{cold}}}{m_{\mathrm{cold,\ 0}}}\right)^{u_2} \cdot \left(\frac{T_{\mathrm{inlet,\ hot}}}{T_{\mathrm{inlet,\ hot,\ 0}}}\right)^{v_1} \cdot \left(\frac{T_{\mathrm{inlet,\ cold}}}{T_{\mathrm{inlet,\ cold,\ 0}}}\right)^{v_2} \cdot \tag{5.48}$$

The pressure drop coefficient (at both sides—cold and hot) during the off-design operation can be determined based on knowledge of its value at design point and reduced mass flows at both nominal and off-design conditions.

$$\xi_{\mathrm{HX}} = \xi_{\mathrm{HX,\ 0}} \cdot \bar{m}^2_{\mathrm{inlet,\ red}} \tag{5.49}$$

$$\bar{m}_{\mathrm{inlet,\ red}} = \frac{m_{\mathrm{inlet,\ red}}}{m_{\mathrm{inlet,\ red,\ 0}}} \tag{5.50}$$

$$m_{\mathrm{inlet,\ red}} = \frac{m_{\mathrm{inlet}} \cdot \sqrt{j_{\mathrm{inlet}}}}{p_{\mathrm{inlet}}} \tag{5.51}$$

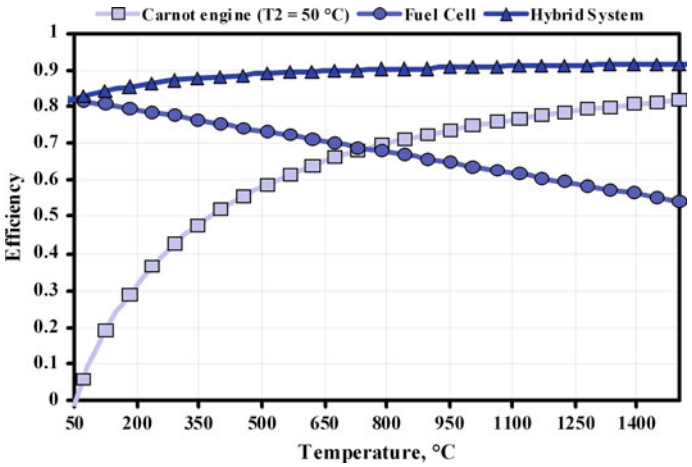

Fig. 5.46 Theoretical efficiency of fuel cell-hybrid system

5.2.5 Combustion Chamber

A combustion chamber can be calculated either based on kinetic theory (reaction rate equations) or a chemical equilibrium constant. Knowledge about the exact value of partial pressures of the reactants is unnecessary this time, and simple calculations based on minimize of Gibbs free energy can be used.

Usually, the combustion chamber works with a high ratio of oxidant (O_2) to fuel, thus it can be assumed that all fuel is utilized completely. In this case the combustion chamber model can be simplified to a mass and energy balance calculation for knowing the higher heating value (HHV) for a fuel.

During off-design calculation, knowledge of the pressure drop across the combustion chamber is needed. The same relationships can be used as for a heat exchanger model (see Eq. 5.46).

5.3 Fuel Cell–Gas Turbine Hybrid System

The main advantage of combining the fuel cell with a classic power plant system is that one can create a binary system which can potentially achieve ultra-high efficiencies (see Fig. 5.46). This task is fulfilled through the other system using the fuel cell exhaust heat.

A typical Solid Oxide Fuel Cell–Gas Turbine Hybrid System (SOFC–GT) consists of the following elements:

- Air Compressor,
- Fuel Compressor,

- Gas Turbine; Air Heater,
- Fuel Heater, and
- SOFC Module.

The SOFC–M is not the only power source in the SOFC–GT hybrid system (additional power is produced by the gas turbine subsystem). SOFC–GT hybrid system efficiency is defined by the following relationship:

$$\eta_{\mathrm{HS}} = \frac{P_{\mathrm{SOFC}} + P_T - P_C - P_{\mathrm{fuel}} - P_{\mu fan}}{m_{\mathrm{fuel}} \cdot LHV} \tag{5.52}$$

SOFC–GT hybrid systems can be classified based on fuel cell module operational pressure. Systems in which the gases leaving the fuel cell are comparable to atmospheric pressure are called atmospheric SOFC systems. The second group consists of systems in which the pressure of the exhaust gas leaving the fuel cell is significantly higher than atmospheric; those kinds of systems are called systems with pressurized SOFC.

This classification determines the location of the fuel cell in a power system. Generally, the fuel cell can perform a similar function in the system to that of a combustion chamber, i.e. to oxidize fuel supplied to the system, which results in relatively large quantities of electricity being taken from the fuel cell itself. The combustion chamber works with lower amounts of fuel and does not require a large excess of air in order to reduce the temperature of gas getting to the turbine.

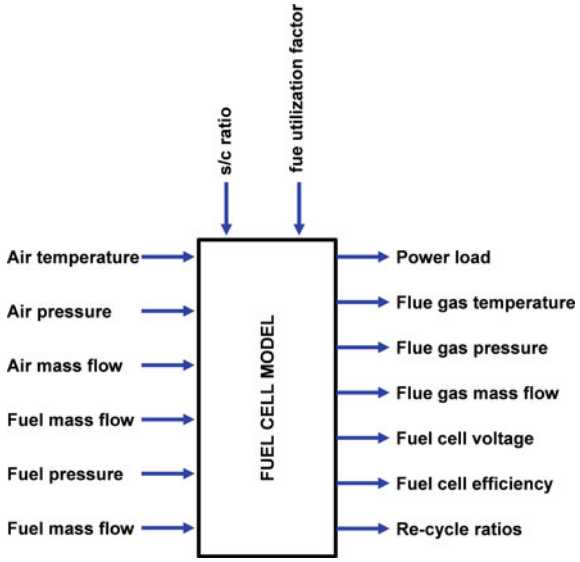

Fig. 5.47 The main parameters of fuel cell model

Exemplary inlet and outlet fuel cell model parameters that are important from the whole hybrid system point of view are presented in Fig. 5.47.

Due to the properties of the electrolyte used in the SOFC–M, the temperature of the working fluids inserted into the module should be relatively high, i.e. 600–900°C. However, too high a working temperature does not significantly increase electrolyte conductivity, and decreases the maximum voltage.

Delivered fuel (mainly methane) has to maintain the flow of gas on the anode. As mentioned earlier, this is done using the gas ejector. Higher pressure methane means more favorable working conditions for the SOFC–M. Natural gas pressure available from the transfer pipeline is up to 30 bar, but the SOFC–M may also operate at lower pressures (minimum of 9 bar). If the μ-fan is used, methane pressure can be even lower.

The air pressure should be high enough to maintain the flow through successively: the SOFC–M (cathode side), combustion chamber and the regenerative heat exchanger(s). After adding all related pressure drops, the minimum air pressure required at SOFC–GT inlet is approximately 3 bar, which means that some kind of blower is needed. With a pressurized SOFC–M, air should be delivered at significantly higher pressure, and compressed by an air compressor.

5.3.1 SOFC–GT Hybrid System Evaluation

The fuel cells used in laboratories are typically characterized by weaker performance than the fuel cells used commercially. On the other hand, laboratory test cells are relatively well described and there is an appropriate amount of data needed to find appropriate model coefficients.

The laboratory fuel cell generates electricity at very low efficiency: ≈18% with a 46% fuel utilization factor. Those values are very impractical for power generation purposes, and adequate scaling up procedure is proposed to evaluate the hybrid system performances. The system evaluation is started from the SOFC–M as a stand-alone unit. The SOFC only represents a device which generates power by utilization of the SOFC stack only, without any additional devices. Next, a few

Table 5.5 Main factors used in the SOFC model

Factor	Value
Anode thickness (μm)	1020
Cathode thickness (μm)	70
Electrolyte thickness (μm)	8
Electrodes ionic conductivity (S/cm)	2.75
YSZ σ_0 (S/cm)	390.95
YSZ E_0 (kJ/mol)	87.806
Electrodes σ_0 (S/cm)	1567.1
Electrodes E_0 (kJ/mol)	67.22
Area Specific Electrical resistance (cm^2/S)	5.50

system configurations were analyzed for both pressurized and atmospheric types of SOFC–M.

The presented evaluation is based on an SOFC model validated on experimental data. The SOFC model main parameters are listed in Table 5.5. Those factors are needed for determining current density–voltage curves.

The SOFC has to fulfill the tasks associated with generating electricity. To establish an optimal nominal point, the variables responsible for electricity generating efficiency were selected. The SOFC–M as part of the system is characterized by the following parameters:

- Fuel cell working temperature,
- Fuel cell working pressure,
- All inlets delivered to the fuel cell,
- All outlets taken from the fuel cell,
- All maxima and minima limits of all parameters delivered to and taken from the fuel cell,
- Technical realization of electric load output,
- current–voltage characteristics of the fuel cell,
- Factors depend on fuel cell operation characteristics.

5.3.1.1 SOFC Only Case

The simplest SOFC is to use SOFC–M in stand-alone mode fuelled by hydrogen; there is no need (no carbon deposition risk) to use either anode or cathode recycle flows. A diagram of the SOFC–M Stand-Alone unit is shown in Fig. 5.48.

There is a possibility to add the recycles on both the anode and cathode sides of the fuel cell (see Fig. 5.49). The anode side recycle gives an opportunity to work the fuel cell stack with a low fuel utilization factor and utilize the large amount of fuel delivered to the system at the same time (the quantity of fuel at stack inlet is

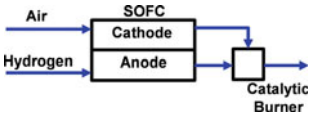

Fig. 5.48 The configuration of the SOFC only case

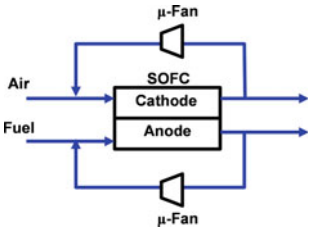

Fig. 5.49 The configuration of the SOFC-only case with recycle at both anode and cathode

much higher than the quantity of fuel delivered to the system). This considerably boosts system efficiency; in contrast, the cathode side recycle has a slightly negative effect on cell voltage (decreases oxygen partial pressure) but helps temperature management in the cell by elevating the cathode inlet temperature. The hydrogen fueled laboratory scale SOFC generates electricity at 18% efficiency. Implementation of both the anode and cathode recycles increases efficiency to 37%, with a fuel utilization factor of 26%. Apart from the increase in efficiency, those recycles bring the required heat balance to the cell.

5.3.1.2 Pressurized SOFC–M Systems

Figure 5.53 schematically shows a gas turbine system consisting of an air compressor, combustion chambers and a gas turbine. Compressed air is delivered to the combustion chamber. Flue gases at elevated temperature and pressure, expand through the gas turbine. The gas turbine drives the air compressor (which takes about 2/3 of the turbine's power) and the remaining power is converted to electricity by a generator.

From the gas turbine system point of view, the pressurized SOFC–M can be placed between the compressor and combustion chamber. There are two possible solutions: first, the SOFC–M simply replaces the combustion chamber, and second, the SOFC–M is located directly in front of the combustion chamber.

The first hybrid system (Case 1) consists of an SOFC stack fueled by hydrogen, and a gas turbine subsystem. Both anode and cathode recycle streams were added.

Simple addition of a gas turbine subsystem to the SOFC–M raises efficiency to 57%. The efficiency increase is mostly caused by the anode recycle process, which allows the cell to be worked at a low fuel utilization factor (21%) while simultaneously utilizing 75% of the fuel delivered to the system. The power generated by the gas turbine subsystem represents about 30% of the total system power.

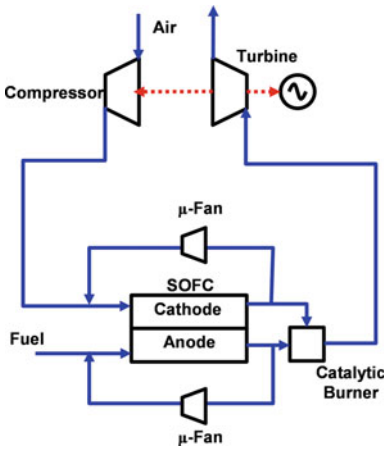

Fig. 5.50 SOFC–GT hybrid system where the combustion chamber has been replaced by a fuel cell. The system configuration is labeled Case 1 (for hydrogen as fuel) and Case 2 (for methane as fuel)

Hydrogen is not readily available in uncombined form and a more practical fuel is natural gas (NG), which consists mainly of methane. The second hybrid system (Case 2) has the same configuration as Case 1, but is fueled by methane. The internal reforming reactions convert the thermal energy generated inside the SOFC to the form of fuel by decomposing methane and steam to hydrogen. This raises efficiency to 63%; this is mostly caused by the process of heat recuperation through internal steam reforming reactions of methane. Other system parameters are: gas turbine pressure ratio of 19 with TIT of 1100°C. There are two recycle streams: on the anode and cathode sides. The anode side recycle is crucial to obtaining high efficiency and should be kept as high as possible.

Systems with a pressurized fuel cell replacing the combustion chamber (see Fig. 5.50) has significant limitations related to the operating temperature of the fuel cell. The temperature of gases at gas turbine inlet is determined by the operating temperature of the fuel cell. Theoretically, this temperature can be raised by reducing the fuel utilization factor, but it is associated with significantly worse performances.

The next solution is presented in Fig. 5.51. Application of the combustion chamber allows for greater independence of the gas turbine operation from the fuel cell itself. In extreme cases the fuel cell does not work at all, and all power is produced by the gas turbine. This system seems to be a natural application of a high temperature fuel cell.

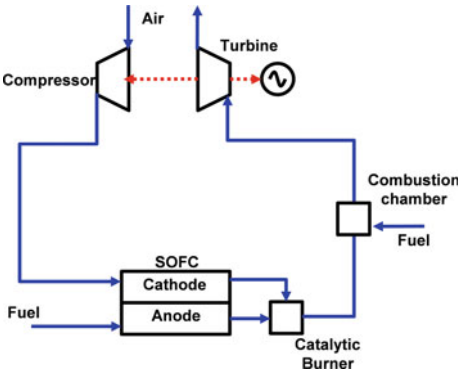

Fig. 5.51 SOFC–GT hybrid system with the fuel cell placed before the combustion chamber

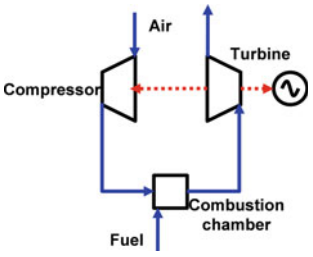

Fig. 5.52 Scheme of gas turbine system

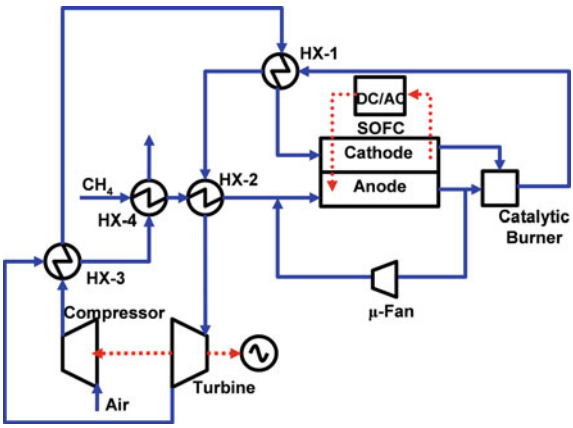

Fig. 5.53 SOFC–HS general scope

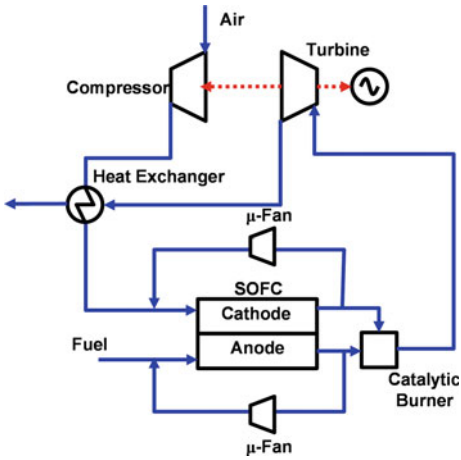

Fig. 5.54 The system configuration of Case 3

A stand-alone gas turbine system in the configuration shown in Fig. 5.52 has a relatively low value of generating efficiency (≈20%). This value can be raised (to 30%) by adding a recuperative heat exchanger, which is usually placed between the air compressor and combustion chamber and fed by turbine exhaust.

The next upgrade of the SOFC-based system is the addition of a heat exchanger, which is placed between the fuel cell stack and the air compressor, similarly to upgrade the open cycle gas turbine system. The heat exchanger is fed by the gas turbine outlet stream. The systems labeled Cases 3 and 4 have only a singular heat exchanger located in the same place as in the gas turbine system (just after the air compressor and fed by the gas turbine outlet stream). The only difference between those systems is that the fuel cell area of Case 4 is twice the size.

In Case 3, an adequate heat exchanger can increase efficiency by recovering part of the heat from the gas turbine outlet. This solution increases efficiency to 66% and decreases the gas turbine pressure ratio to 8.2. TIT is still very high at

Table 5.6 Results of the pressurized SOFC–GT system evaluation

Parameter	SOFC	SOFC	1	2	3	4
Fuel	H_2	H_2	H_2	CH_4	CH_4	CH_4
Efficiency (%)	18	37	57	63	66	68
Fuel utilization Factor (%)	46	26	21	27	26	34
Anode recycle (%)	0	90	90	90	85	90
Cathode recycle (%)	0	70	40	43	43	42
i_{max} (A/cm^2)	5.4	5.4	5.4	5.4	5.4	2.77
TIT (°C)	–	–	1100	1100	1100	1025
GT pressure ratio	–	–	13	19	8.2	9.6
s/c ratio	–	–	–	4.1	2.5	5.0
Heat exchanger effectiveness (%)	–	–	–	–	90	62
Fuel cell area (cm^2)	2.9	2.9	680	610	463	780
Maximum current density (A/cm^2)	5.4	5.4	5.4	5.4	5.4	2.77
Power given by GT in relation to total system power (%)	–	–	31	23	33	22

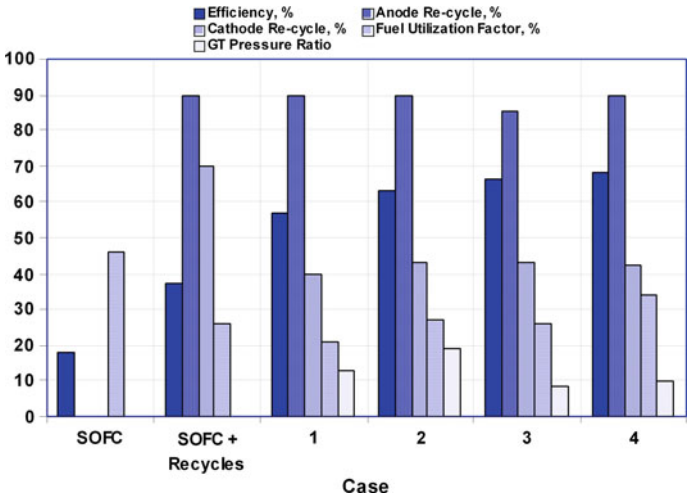

Fig. 5.55 Main parameters of the analyzed cases

1100°C. The volume of the heat exchanger is relatively large, because 90% effectiveness is needed. In Case 4, increasing the fuel cell area by a factor of two causes efficiency to rise by only 2%. Any technical investigation must be performed together with an economics-based analysis to obtain the most favorable system configuration from the financial point of view.

A sole heat exchanger was installed in previous cases, but in the SOFC–GT hybrid system there are four possible locations for placing the heat exchangers, all of which are indicated in Fig. 5.53. The regenerative heat exchangers can be used

to reduce exhaust losses, the heat exchangers draw part of the energy from the exhaust flow and increase the temperature of streams directed to the fuel cell (Fig. 5.54).

The system with the structure shown in Fig. 5.53 has been optimized to find the optimal values of all parameters, and then to find the design point of the SOFC–GT hybrid system.

A summary of all parameters obtained during evaluation of hybrid system with a pressurized SOFC–M is shown in Table 5.6 and Fig. 5.55.

A hydrogen fueled laboratory scale fuel cell can achieve efficiency of 37% by adding recycles at both the anode and cathode sides. The addition of a gas turbine subsystem (Case 1) can boost efficiency to 57%. By changing the fuel from hydrogen to methane efficiency is increased to 63% (Case 2) due to reforming reactions which convert thermal energy into the chemical energy of fuel. The addition of a heat exchanger gives increased efficiency, rising to 66% (Case 3).

The previously presented model contains the factor i_{max}, which introduces a correlation between the cell voltage, cell area and quantity of delivered fuel. This means that a larger fuel cell will generate relatively higher voltages along with lower current densities. Then the fuel cell size can go through an optimizing procedure. For the selection of cell size the value of i_{max} is optimized in Case 4 where an additional 2% efficiency is achievable. The 2% increase is obtained through almost doubling the size of the fuel cell.

Energy path flows in a pressurized SOFC–GT hybrid system are shown in the form of a Sankey diagram in Fig. 5.56.

Selection of the size, design and working parameters of the SOFC is crucial when seeking to obtain a highly efficient hybrid system. Additionally, both a gas turbine and an air compressor should be designed for operation with SOFC.

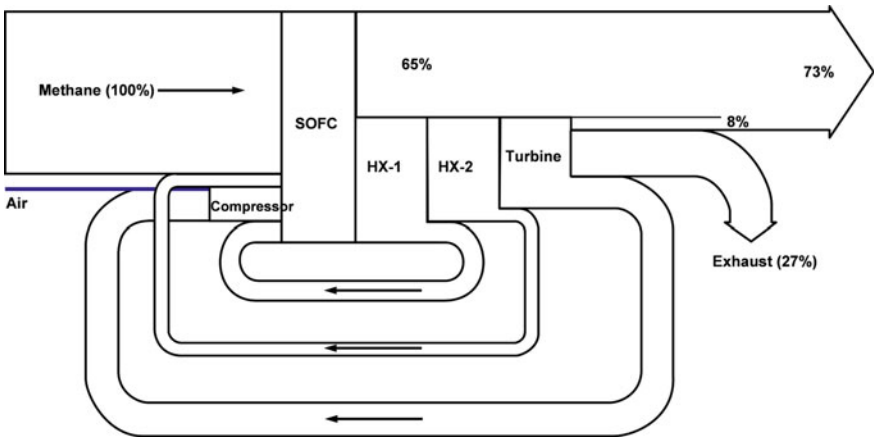

Fig. 5.56 Sample Sankey's diagram of energy flows of SOFC–GT hybrid system

5.3.1.3 Atmospheric SOFC–M systems

In the cases with an atmospheric SOFC–M, increased system efficiency can be achieved only by heat recuperation through a bottom cycle. In systems containing an atmospheric SOFC, the use of additional equipment is needed to recover part of the exhaust heat. The simplest bottom cycle is based on an air turbine subsystem (composed of an air compressor and air turbine). This solution is shown in Fig. 5.57. Heat is transferred to the bottom cycle by adequate heat recuperative heat exchangers. In this case, SOFC flue gas is considered as the upper heat source for the air turbine cycle.

Regenerative heat exchangers can be used both on the air and fuel flows. One limitation in this solution is the air compressor, because the temperature of compressed air is increased. Therefore, the desirability of a regenerative heat exchanger at the flow depends on the temperature of the exhaust leaving the gas turbine. This problem can be solved by introducing an additional combustion chamber, located before the exchangers. This causes an independent fuel cell operation from temperature rise before the heat exchangers.

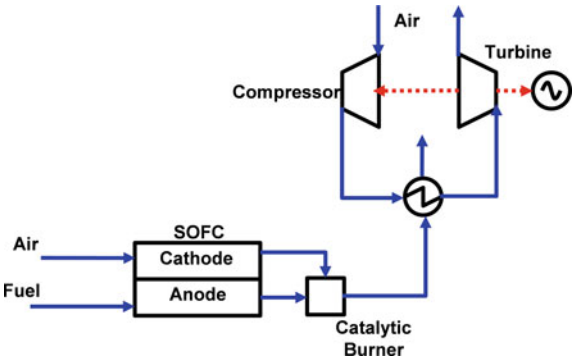

Fig. 5.57 Diagram of an atmospheric SOFC with a bottom cycle based on an air turbine

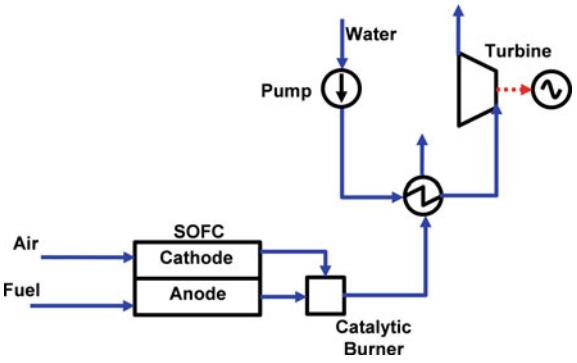

Fig. 5.58 Diagram of an atmospheric SOFC with bottom cycle based on an open steam cycle

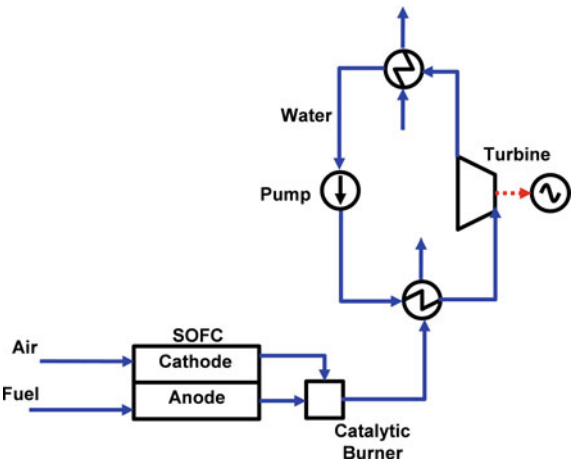

Fig. 5.59 Diagram of an atmospheric SOFC with bottom cycle based on a closed steam cycle

This system suffers from relatively low efficiency due to the relatively large amount of power consumed by the air compressor. To increase the efficiency of the system, water (steam) can replace the role of compressed air. Much less energy is required to raise water pressure than to compress air to the same pressure. The system is illustrated in Fig. 5.58. The system with a bottom cycle based on an open steam turbine cycle has better performances than the one based on an air turbine due to the reduced compression and better conduction of heat in the heat recovery steam generator (HRSG).

Steam at a temperature of more than 100° leaves the system. Firstly, the system in this configuration will utilize huge amounts of water. Secondly, all the heat of vaporization of water is lost to the environment. Part of this heat can be recovered using a system working in the Rankine cycle. This solution is presented in Fig. 5.59 and is comparable to the classic gas turbine combined cycle (GTCC) in which the SOFC is placed instead of a gas turbine.

5.3.1.4 Optimization Procedures

The system configuration with the most general structure (see Fig. 5.53) was optimized to find the system optimal point (design point). System efficiency was chosen as an optimizing objective function. Efficiency is defined by Eq. 5.52. Optimization calculations were performed through use of the BOX method [22], based on a sequential search technique for the best value objective function. The method concerns nonlinear problems with nonlinear constraints. The following system parameters were subjected to an optimization process (ranges shown):

1. Gas Turbine pressure ratio (1–30);
2. SOFC fuel utilization factor (η_f), (%) (0–90);

3. SOFC anode recycle ratio (%) (0–90);
4. SOFC cathode recycle ratio (%) (0–90);
5. Heat Exchanger Effectiveness (η_{HX}) (%) (0–90);
6. Maximum current density (i_{max}) (A/cm^2) (2.7–10);
7. Turbine inlet temperature—TIT (°C), (500–1100).

Optimizing procedures were carried out with several constraints. They mainly regarded specific operational conditions of the fuel cell. The following constraints should be applied during optimizing procedures:

- Steam-to-carbon ratio >1.4
- Fuel cell voltage > 0.4 V
- Oxygen utilization ratio < 0.9

Some parameters were fixed at constant values, and they are

1. Heat transfer effectiveness inside the singular cell: 30%;
2. Isentropic efficiency of the air compressor: 81%;
3. Isentropic efficiency of the gas turbine: 87%;

As a result of optimizing procedures, a structure (at maximum efficiency) was determined for the SOFC–GT hybrid system. This system consists of a fuel cell

Table 5.7 Optimization results for the SOFC–GT hybrid system

Parameter	Value of optimization result
Fuel utilization factor (%)	84
Air compressor pressure ratio	7.3
Anode recirculation ratio (%)	46
Maximum current density (A/cm^2)	1.12
The effectiveness of the heat exchanger HX-1 (%)	0
The effectiveness of the heat exchanger HX-2 (%)	0
The effectiveness of the heat exchanger HX-3 (%)	85
The effectiveness of the heat exchanger HX-4 (%)	45
TIT (°C)	1000
System efficiency (%)	72.3
GT power/system power (%)	21.4
SOFC power/system power (%)	80.1
Fuel compressor power/system power (%)	1.4
Fuel pressure (bar)	7.66
SOFC operating temperature (°C)	900
Exhaust gas temperature leaving the system (°C)	355

module, two heat exchangers (regenerative), and a gas turbine. The results of the optimizing process are shown in Table 5.7. They show that there are no technical barriers to achieving system efficiency of higher than 70% when utilizing the SOFC–GT hybrid system. Nevertheless, all devices should be specially designed and manufactured for the fuel cell based hybrid system.

5.3.2 Control Issues of SOFC–GT Hybrid System

It should be underlined that, in the case of a system which contains both a pressurized SOFC–M and a gas turbine, varying the amount of fuel injected is not the only way of changing the system power output. Fuel cell voltage and current are quite dependent on the variable rotational speed of the compressor-turbine unit. This is accompanied by varying system efficiencies. Hence there is a need to formulate an appropriate control concept (control strategy logic) and its approach for technical realization.

Control strategy is an important element in designing any system of this kind and it constituted a significant part of the modeling works done. Off-design (part-load) analysis is an important issue for any type of system involving an SOFC–GT hybrid system and should be taken into account when designing and defining the operational characteristics. A proper off-design map of performance underscores control strategy design. Results drawn from system behavior analysis under part-load conditions should aid in defining the system structure and its nominal parameters, as well as the constructional solution and characteristics of a given subsystem.

Part-load operation characteristics research regarding SOFC–HS can be reduced mainly to study of the conditions of co-operation among the SOFC, turbo machines and other equipment. A specific feature of this study is the existence of many bonds and limits. Bonds are defined mainly by the system configuration and properties of devices that make up the system, together with their characteristics. Limits usually result from boundary values of working parameters. Thus, studying the conditions of co-operation of the SOFC–GT can be reduced to describing and analyzing all possible operational stages. Part-load and over-load performance characteristics of SOFC–GT were calculated and analyzed to show control possibilities of the cycle.

Off-design (part-load) analysis is an important issue for any type of system including an SOFC–GT and should be taken into account during designing and defining operational characteristic. Results of the system behavior analysis under part-load conditions should aid in defining the system structure and its nominal parameters, as well as the constructional solution and characteristics of a given subsystem.

5.3.2.1 Background

Off-design operation of a solid oxide fuel cell hybrid system was analyzed previously by many authors and a few notes on chosen works are set out below.

Bessette et al. [23] investigated the prediction of on-design and off-design performance for a solid oxide fuel cell power module. In this study, the SOFC module was investigated separately from turbo-machinery. The SOFC module consisted of tubular cells and worked at 1000°C. They found that the linear scaling of single cell results does not give an accurate assessment of the whole stack's performance.

Costamagna et al. [24] investigated design and part-load performance of a hybrid system based on a solid oxide fuel cell reactor and micro gas turbine. This study contains models of a centrifugal compressor and inflow expander. There is no ejector model analyzed in this paper. The hybrid system operated at 0.38 MPa and 800–1000°C, and generated about 290 kW at 60% efficiency.

Chan et al. [25] modeled a part load operation of a solid oxide fuel cell-gas turbine hybrid power plant. This paper contains a centrifugal compressor model and axial turbine. The system generated 1.7 MW at 60% efficiency. The turbine inlet temperature was 1036°C at a pressure ratio of 3. This paper contains no detailed model description of an SOFC module and ejector.

Marsano et al. [18] investigated the influence of ejector performance on a solid oxide fuel cell recirculation (recycle) system. This investigation concerned a 240 kW power system. They found that the ejector plays a key role during off-design operation.

Ferrari et al. [19] investigated the influence of anodic recirculation transient behavior on performance of an SOFC hybrid system. Generally, they confirmed the results obtained in the previous study [18].

Stiller et al. [26] investigated the safe operation of a simple SOFC/GT hybrid system. They presented a set of maps of hybrid system performance during off-design operation. The main parameters are shown as a function of two parameters: relative shaft speed and relative fuel flow. This paper contains no description of the models used.

Stiller et al. [27] investigated a control strategy for a solid oxide fuel cell and gas turbine hybrid system. This work contains similar results to the previous paper [26].

Calise et al. [28] investigated the design and partial load exergy analysis of a hybrid SOFC–GT power plant. In this paper the system has no ejector device. The temperature of the SOFC is about 1000°C. The turbine inlet temperature and pressure ratio are 1002°C and 7.4, respectively.

Stiller [29] focused his thesis on modeling-based design, operation and control of solid oxide fuel cell and gas turbine hybrid systems. He described the models used and examined three different hybrid cycles. The objectives for highly efficient and safe system design are formulated and its design parameters are associated. The analyzed system is a 220 kW unit with efficiency of 63%. Control strategy and part-load performances are very similar to those which were described previously [27].

Milewski et al. [20] analyzed the off-design operation of an SOFC hybrid system. Descriptions of the models used are presented in this paper. The algorithm of SOFC–HS off design calculation is presented as well. The following control parameters of the system are specified: fuel mass flow, stack current and rotational shaft speed. Adequate maps of system performance were given and described. The main system parameters are shown as a function of reduced system power and reduced stack current.

This section presents the off-design study of SOFC–HS performance based on the methodology and experience of the Institute of Heat Engineering (Warsaw University of Technology). In particular, this methodology was utilized in the mathematical modeling of the "classic" system elements (e.g. compressor, turbine, heat exchanger, ejector, etc.).

Analyses of external conditions of operation of SOFC–GT hybrid systems have shown that the currently available power outputs of those kinds of system are too low for future applications in DG, which should be in the 4–7 MW range. Analyses have identified the following primary targets for supply by hybrid systems: office buildings, hospitals, large retail units (supermarkets, shopping centers) and military structures. By logical extension, detailed examination was focused on power output of the SOFC–GT hybrid system in the region of 6 MW. In those cases, the axial turbine can be used instead of the radial one for this range of power. This is the main difference between the results presented in this paper and results taken from the literature, additionally an advanced mathematical model of an SOFC is utilized.

5.3.2.2 Control Strategy for an SOFC–GT Hybrid System

Implementation of a control system depends on its structure, which is subject to regulatory processes at work in varied conditions. Two sources of electricity may exist in hybrid systems. Usually one of these sources is to provide the main energy flux while the other plays auxiliary functions. There is therefore a need to identify possible structures for systems analysis of power distribution to the various subsystems. A multi-stage procedure is used to determine the control strategy of SOFC–GT hybrid systems, as follows:

1. Internal constraints of the system are determined based on the chosen structure and parameters of the nominal SOFC–GT systems (i.e. mechanical, flow and electrical connections between the elements and characteristics of specific elements).
2. Mathematical model of the system is built at the level of off-design operation.
3. Based on the model all possible working conditions are determined. A database is made of those steady-state points of the system.
4. Based on the database an adequate searching algorithm is used to find the most convenient operation line of control strategy for chosen criteria (e.g. highest system efficiency).

5. The control strategy is realized by the first level of the multi-layer control system.

The control strategy of the system should allow one to quickly and accurately follow the load profile, while maintaining good system efficiency. Safe operation of the system is an obvious requirement. Based on mathematical modeling and numerical simulations, the control strategy for an SOFC–GT is presented.

An SOFC–GT hybrid system has three degrees of freedom, and having regard to μ-fan up to four; which means that at least three free parameters (see Fig. 5.60) can vary independently within certain ranges. Any combination of them should define a certain state of the system. An SOFC–GT hybrid system has only one control variable, which is generated power, and three manipulated variables, i.e. the current cell module, the flow of fuel and the electric generator load. The dependencies and relationships occurring in the hybrid system can be divided into four groups:

1. Correlations defined by a mechanical scheme of the system (mechanical linkage of turbines, compressors, generators
2. Correlations defined by the flow chart, (i.e. flow relationship between the compressor, turbine, fuel cell, heat exchangers and other components of the system and the order of the working flow direction through system elements)
3. Depending on specific characteristics of turbines and compressors (average parameters at the inlet and outlet of the rotating machine are closely linked through its characteristics)

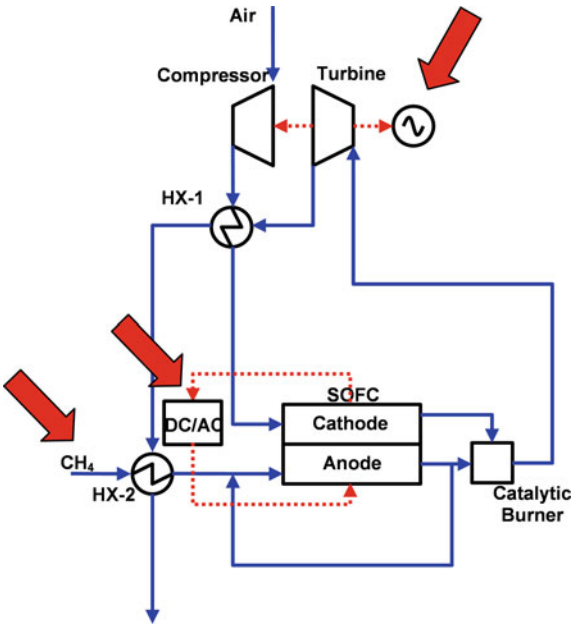

Fig. 5.60 SOFC–GT hybrid system with control variables indicated

4. Depending on the characteristics associated with other system elements.
5. Depending on specific electrical connections inside the system.

SOFC–GT hybrid system can be controlled using the following parameters:

- Electric current taken from SOFC stack by external resistance (load),
- Fuel mass flow by valve, and
- Rotational speed of the compressor-turbine subsystem by power output of electric generator with adequate power electronic converter.

The responses of an SOFC–GT to these three main parameters were investigated. Calculations revealed the working conditions of the SOFC–GT in off-design operation to range over several thousand different points in relation to its design point. Approximately 16,000 system operation points (state points) were found for the SOFC–GT. Every state point is defined by three independent parameters: delivered fuel flow, rotational speed of compressor-turbine subsystem, and stack current. The other flows and electric parameters were taken for these three parameters.

The following limitations were applied when gathering those points: maximum temperature (1000°C), minimum gas turbine subsystem power (0 kW), minimum total system power (0 kW), and minimum cell voltage (0 V). That means all physically possible points were collected.

This data set for the SOFC–GT was extremely large and difficult to analyze, so adequate maps of parameter changes were constructed to present the most important results. An appropriate control strategy should keep the system at its optimal point for the determined external power demand. The optimal operation point often means the point of highest possible efficiency, but not always. Adequate control strategy should avoid a work system that tolerates either unsafe conditions or conditions which may shorten the lifespan of a system device. It was found that the best system performances are obtained at various fuel utilization factors—see Fig. 5.61. The graph shows only general relationships between various fuel utilization factor surfaces and main system parameters (total power, efficiency, rotational shaft speed); hence axis values are not shown.

It can be seen that various fuel utilization factor surfaces give various maximum power values generated and various levels of system efficiency. In aggregate, many more fuel utilization factors surfaces were calculated than are shown in Fig. 5.61. So, the points with highest system efficiency with various fuel utilization

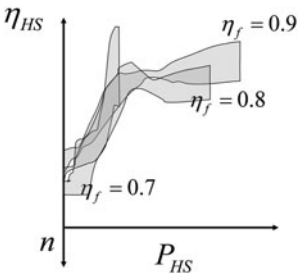

Fig. 5.61 SOFC–GT hybrid system efficiency layers for three different fuel utilization factors

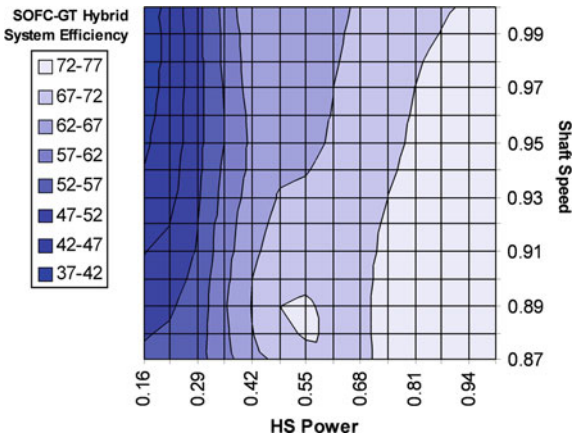

Fig. 5.62 SOFC–GT hybrid system's highest possible efficiency points

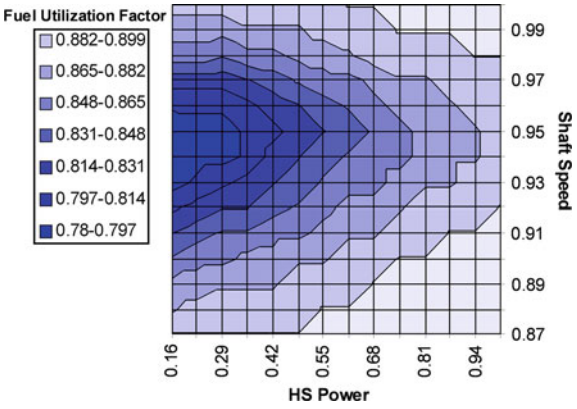

Fig. 5.63 Fuel utilization factor collected for highest efficiency points

factors were separated and collected. The map for highest possible efficiency of the SOFC–GT hybrid system is shown in Fig. 5.62.

The map of performance for the fuel utilization factor is presented in Fig. 5.63. In general, the lower the SOFC–GT load forces, the lower the fuel utilization factor. The highest fuel utilization factor is 0.9 whereas the lowest value is 0.8. This means there is little distance between the maximum and minimum values.

The next important parameter of SOFC–M operation is the temperature difference between the fuel cell stack inlet and outlet. Good thermal management of the stack is very important for the dynamic operation of the whole system—mainly start-up and shutdown of the unit. There should be little difference between those temperatures. An adequate map of performance is presented in Fig. 5.64. The stack temperature differences are relatively high (reaching values above 300°C) for low rotational speed of the gas turbine subsystem. This is due to the lower quantity of air delivered, resulting in worse cooling of the stack.

SOFC–M operation influences the gas turbine subsystem, and the most crucial parameter of the gas turbine is the turbine inlet temperature (TIT). If there are no

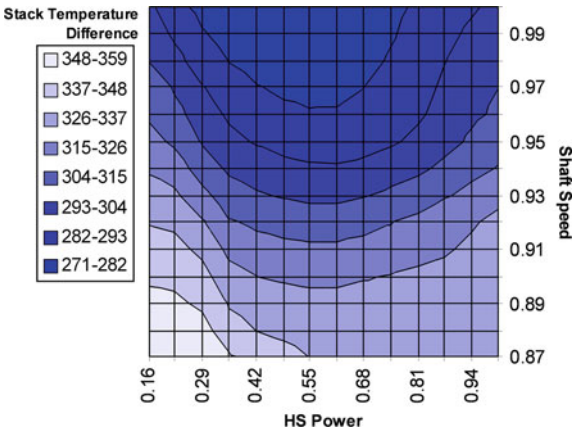

Fig. 5.64 Stack temperature difference (°C) for highest system efficiency points

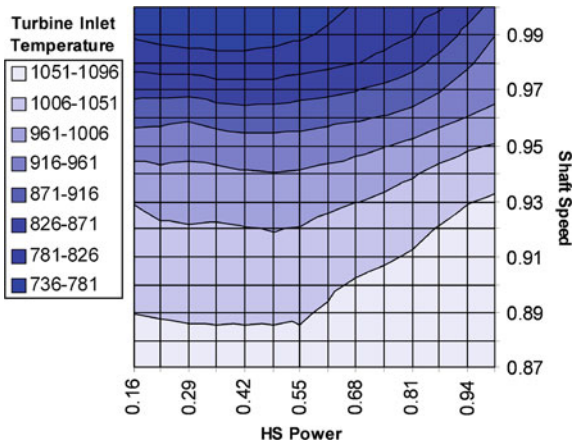

Fig. 5.65 Turbine Inlet Temperature (°C) for highest system efficiency points

cooling blades in the turbine, the temperature should be kept at a relatively low level (≈900°C). Changes in TIT are shown in Fig. 5.65.

The presented maps of performances cover all physically possible operation points of the SOFC–GT system. Technical realization and further exploitation of the system requires additional limitations. Specific restrictions on hybrid system operation depend on many factors, including: the materials used, construction, catalysts, etc. Such restrictions allow all technically possible points of system operation to be obtained; however, specific design solutions impose additional constraints.

Ensuring safe operation of the system requires the elimination of events (operating conditions) that could damage the system or its components. This represents at the same time a limit on the scope of permissible working conditions (states) of the system. Typical constraints normally are a result of

- Acceptable working fluid parameters (mainly the highest temperature and pressure)
- Acceptable electrical parameters
- Compressor limits (surge line)
- Critical frequencies of rotating machines
- Acceptable torques

Those limitations can be chosen arbitrarily, and the values presented below are only exemplary. Adequate ranges for safe operation of the SOFC–GT hybrid system were indicated on the system efficiency map. Based on data calculated for all technically possible conditions, additional limits and bounds were applied on the system efficiency map, and they are as follows:

- Average cell temperature $<1000°C$;
- SOFC stack temperature difference $<320°C$;
- Turbine Inlet Temperature (TIT) $<1000°C$;
- Air compressor surge limit curve.

Other conditions reflect the more general requirement to maintain fuel cell stability, fostered by keeping the cell temperature as constant as possible and reducing (limiting) charged current (limited local heat source). The amount of steam at the anode inlet must be monitored to avoid carbon deposition during reforming processes. Deposition takes place when the temperature is too low and/or there is too little steam at the inlet to the stack (low s/c ratio). A reverse flow of gases from the combustion chamber to the anode channels can result in anode coming into contact with oxygen—anode reverse flow can occur with rapid increases in pressure, hence the need to limit the increase in pressure over time. And finally, too low a fuel cell voltage can result in unstable fuel cell stack operation.

The limitations listed above were applied on the map with the highest possible efficiency points. Thus, restricted areas are indicated and a safe operation line can be obtained. It seems the obvious choice that the line passes points of highest efficiencies and should be generated as shown in Fig. 5.66. This line must be

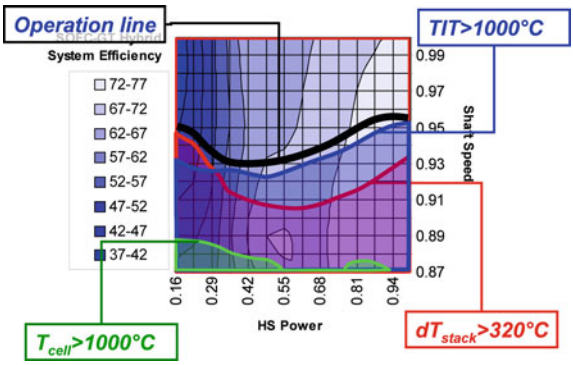

Fig. 5.66 Example of an SOFC–GT hybrid system efficiency map with applied limits and indicated operation line

realized by the control system. The aim is to achieve maximum efficiency of power generated within those constraints. It should be underlined that the presented operational line of the system is given in coordinates matched to parameters which can be closely controlled (e.g. by a valve), whereas other works (e.g. [27]) propose controlling parameters which can be difficult to control (e.g. compressor air flow). Taking into account controllable parameters, the control strategy can be based on the following three functional relationships:

$$m_{\text{fuel}} = f(P_{\text{HS}}) \tag{5.53}$$

$$n = f(P_{\text{HS}}) \tag{5.54}$$

$$I_{\text{SOFC}} = f(P_{\text{HS}}) \tag{5.55}$$

Choosing the highest possible efficiency of the system, the relevant functional dependencies (5.55) of all controllable parameters take the form of adequate functions of the system power.

Based on the operation line indicated in Fig. 5.66 and using the database of all system points, three control parameters were determined as functions of external power demand. The controllable parameters of the system as a function of system power are presented in Fig. 5.67. The figures were normalized to their maximum values. It is evident that both the current cell stack and the amount of fuel supplied are close to the linear trend. The rotational speed of the gas turbine is relatively constant (+/−10%), reaching a maximum of 50% system load.

It can be seen that the fuel cell stack current should be increased more rapidly than the fuel mass flow. The shaft speed should be increased until system power

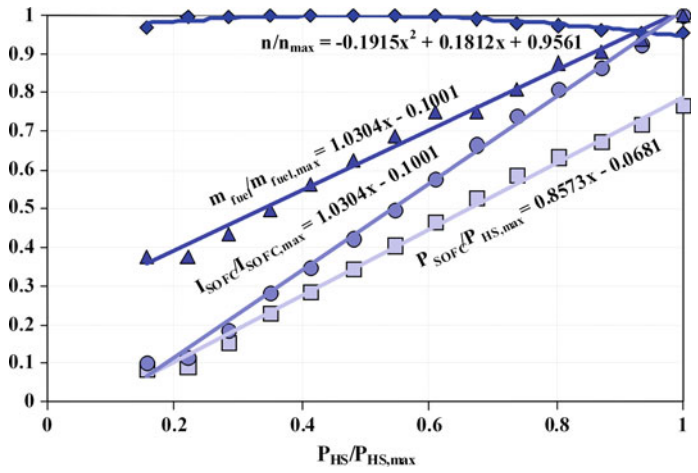

Fig. 5.67 Relationships of steering parameters of SOFC–GT. Legend: n —GT shaft rotational speed, I —SOFC stack current, m —fuel mass flow, P —system power

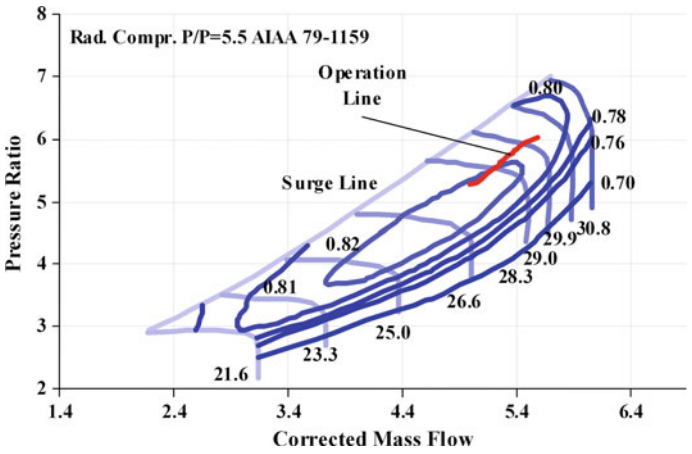

Fig. 5.68 Operation line of control strategy indicated on air compressor map [30] used during simulations

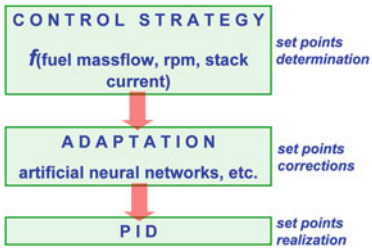

Fig. 5.69 The structure of triple-layer control system

reaches 50% and, thereafter, the shaft speed has to be decreased. The SOFC–GT hybrid system maintains good efficiency even at partial loads. For example, while reducing the system load to about 40% the efficiency is still over 80% of the nominal value.

Normal operation of the system is possible in a wide power range from approximately 17% of the rated power. The average temperature of the cell varies in the range 720–800°C and the temperature difference in the stack is in the range 300–340°C, which can be regarded as acceptable. The operation line is located preferably on the characteristics of the compressor—far from the surge limit (see Fig. 5.68).

The presented results indicate that the analyzed SOFC–GT Hybrid System possesses a high operation and control flexibility while at the same time maintaining stable thermal efficiency. Operation of the system is possible over a wide range of parameter changes. The essential internal conditions of the hybrid system impose structure and nominal parameters of the system chosen for detailed analysis. There are mechanical, flow and electrical connections between the elements and characteristics of the same (specific) components.

The proposed control system is divided into three layers, which clearly separates the "static" control strategy objective function from its dynamic realization. The proposed three-layer control system has a first layer of control responsible for setting the operation point (in terms of a specific objective function), the second layer has the task of adapting to the changing characteristics of the individual components (e.g. degradation of the system elements can be taken into consideration), and the third layer is responsible for implementing the relevant dynamic adjustment (transitions) (Fig. 5.69).

The first layer is responsible for issues relating to overall safety and possibly the effective functioning of the whole system. Properly selected functional dependencies between all adjustable parameters and limits should be included in this layer. The first layer, depending on the required load variable, sets values of all manipulated parameters. These values are then addressed to the PID controllers, which are the lowest third layer of control, virtually eliminating the dynamics of the process, from the viewpoint of the first layer.

The data referred to in the first layer of control may require adjustment or adaptation in respect of operation of the system or changes in circumstances. The second layer (adaptive) is responsible for amendments made to the first layer due to changes in device characteristics that make up the system (e.g. owing to degradation of equipment, etc.).

The final layer implements the control strategy in the dynamic mode. The time needed for convergence of one operation point of the SOFC–GT is much longer than the dynamic response of the system. Through cooperation between two faculties at Warsaw University of Technology (Faculty of Power and Aeronautical Engineering, Faculty of Electrical Engineering) an adequate simulator of SOFC–GT has been made to investigate possible realization of the third layer of the control system. The simulator is composed of three main modules (see Fig. 5.70):

1. Software based models of SOFC–M, heat exchangers, and combustion chamber;
2. Hardware based model of gas turbine subsystem;
3. Control unit (real device).

The structure of the simulator is presented in Fig. 5.71. Main mass and energy flows, control signals and information paths are indicated for each layer of the control strategy. The control unit is composed of two main controllers, separate for the SOFC–GT and the power conditioning unit.

SOFC–GT hybrid system operational characteristics were applied to the simulator as a data set (previously presented as maps of performances) with adequate searching algorithm. The operational characteristics of the software were entered into a desktop computer.

The model of the gas turbine subsystem is composed of an electric motor and electric generator, as is shown in Fig. 5.72. The purpose of the device is to simulate dynamic behavior of rotating equipment and, more importantly, adjustment of the power ratio between the SOFC–M and gas turbine generator, and adequate sets of rotational speed are given from the main simulator.

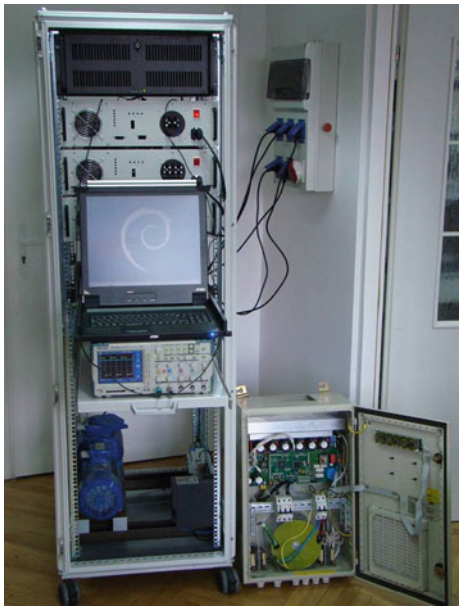

Fig. 5.70 Simulator together with measurement and recording instrumentation (oscilloscope, computer) and the inverter

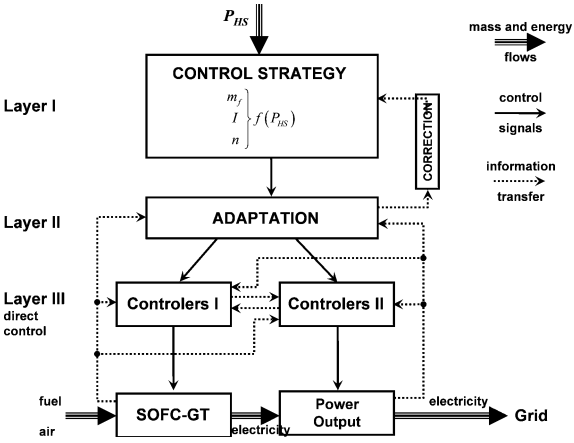

Fig. 5.71 Structure of the control system, P_{HS} —set power of the hybrid system, m_f —inlet fuel flow, I — current, n —rotational turbine shaft speed

The control unit was built as a ready-for-commercial-use device which realizes the control strategy given by obtained functional relationships (see Eq. 5.55). The control unit is shown in Fig. 5.73.

In this section, the first layer (control strategy) of the control system was proposed and described. The second layer (adaptation) can be achieved by deep analysis of aging processes occurring at the SOFC stack and other devices. This issue has not been analyzed to date. The third layer of the control system (regulation) should be realized by adequate PID controllers. This layer is responsible for

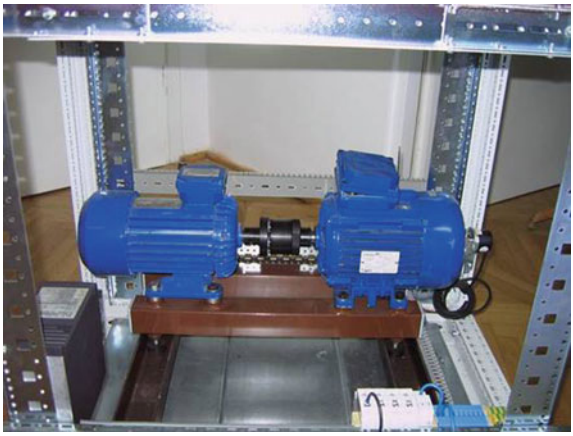

Fig. 5.72 Hardware based model of gas turbine subsystem for simulator—part of gas turbine subsystem

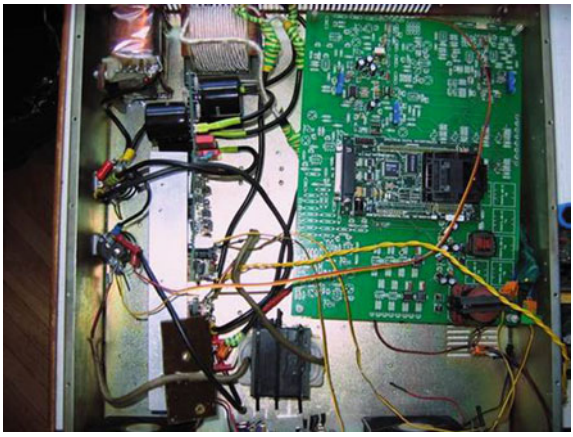

Fig. 5.73 Hardware of the control unit

dynamic operation of the whole hybrid system as well as for keeping system parameters within safe limits during transient operations.

A 3D view of the operation curve of the control strategy is shown in Fig. 5.74. There is still room for discussion about choices made during calculations of the system working points as well as applied limits on the map of performances. The main task is to propose a general structure of the control system which can be applied to a hybrid system where two (or more) sources of electricity are present—thereby giving rise to multiple options as to system exploitation procedure.

5.3.3 Rotating Equipment

Determination of reasonable parameters (due to optimized efficiency) of an SOFC–GT hybrid system also sets the necessary parameters of rotating

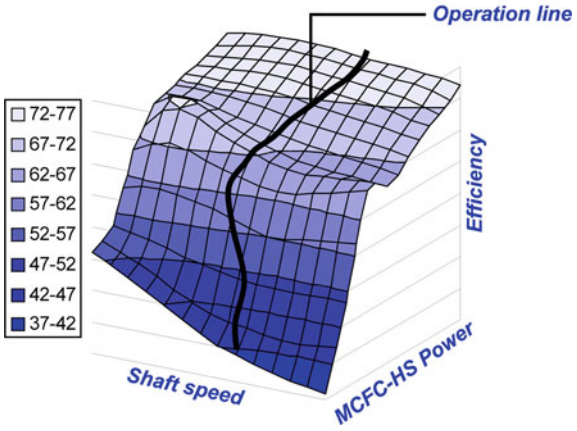

Fig. 5.74 Operation line of the control system indicated on the map of system efficiency

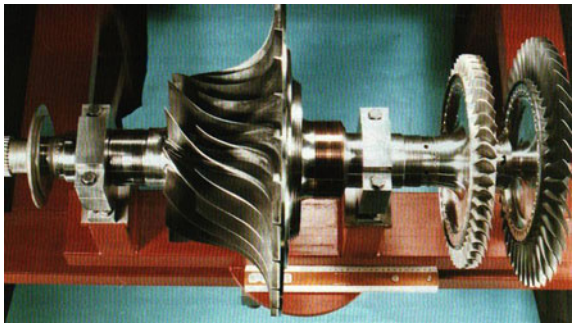

Fig. 5.75 The rotating machinery of HURRICANE 1.7 MW gas turbine, nominal mass-flow 6.8 kg/s, pressure ratio 8.5 (manufacturer's prospect)

machinery and other system components. Need mass flow of both compressor and turbine is in the range 5–9 kg/s at a pressure ratio (both compression and expansion) of 5–6.2.

The parameters of rotating machinery needed for the SOFC–GT can be achieved by a single-stage radial compressor and a two-stage axial turbine. A similar construction with very similar parameters is presented in Fig. 5.75; an exemplary compressor rotor is shown in Fig. 5.76.

5.3.3.1 Air Compressor

Calculations on off-design operation of air compressors are based on real device characteristics presented in the form of maps (for a single stage radial compressor see [30]) with parameters corresponding to the conditions of the SOFC–GT hybrid system concerned. Exemplary characteristics (map) of a compressor are shown in Fig. 5.77.

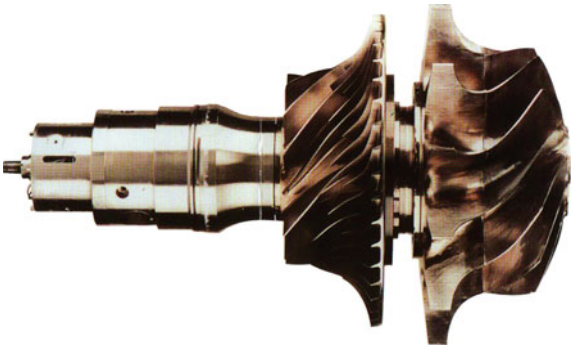

Fig. 5.76 Compressor rotor (*left*), with mass flow of 8 kg/s, pressure ratio 6.7—part of gas turbine OPRA-OP-16 (manufacturer's prospect)

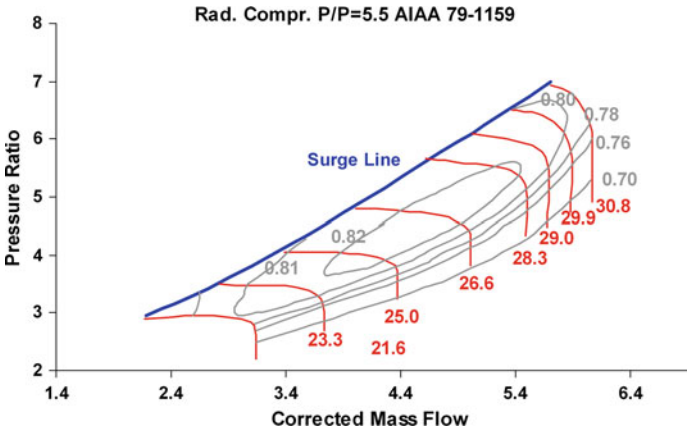

Fig. 5.77 Air compressor map [30]

The map presents the following parameters:

1. Reduced pressure ratio:

$$\overline{\Pi} = \frac{\Pi}{\Pi_0} \tag{5.56}$$

where pressure ratio is given by

$$\Pi = \frac{p_{\text{outlet}}}{p_{\text{inlet}}} \tag{5.57}$$

2. Reduced mass flow:

$$\overline{m} = \frac{m}{m_0} \cdot \frac{p_{\text{outlet}}}{p_{\text{inlet}}} \sqrt{\frac{j_{\text{inlet}}}{j_{\text{inlet, 0}}}} \tag{5.58}$$

where corrected mass flow: $m = \overline{m} \cdot m_0$

3. Reduced efficiency:

$$\overline{\eta} = \frac{\eta}{\eta_0} \tag{5.59}$$

4. Reduced rotational shaft speed:

$$\overline{n} = \frac{n}{n_0}\sqrt{\frac{j_{\text{inlet, 0}}}{j_{\text{inlet}}}} \tag{5.60}$$

Normal enthalpy (j) can be approximated by the following relationship:

$$\sqrt{\frac{j_{\text{inlet, 0}}}{j_{\text{inlet}}}} \approx \sqrt{\frac{T_{\text{inlet, 0}}}{T_{\text{inlet}}}} \tag{5.61}$$

The SOFC–GT works with a lower air excess factor than does the standard gas-turbine unit. This specific requirement means that the air compressor has a lowered flow capacity than is the case for the gas turbine standalone.

5.3.3.2 Gas Turbine

It seems that the SOFC–GT hybrid system should not be equipped with advanced cooling systems for the turbine. 950°C, the adopted highest temperature at the inlet to the turbine (TIT), is admissible for the blade material in the near term.

Unlike the simple properties of the gas turbine, the efficiency of the SOFC–GT hybrid system does not grow here in linear fashion with increasing temperature, but has a maximum, depending on the type of electrolyte. In the case of electrolyte with the highest ionic conductivity (LSGMC), the optimum TIT is about 1050°C, which is close to the material chosen for non-cooling blades (950°C).

The analytical correlations can be applied for multistage turbines instead of turbine characteristics given by a map. In those cases, a group of turbine stages is described by the following equation:

$$\frac{m}{m_0} = A \cdot \frac{p_{\text{inlet}}}{p_{\text{inlet, 0}}}\sqrt{\frac{T_{\text{inlet, 0}}}{T_{\text{inlet}}}}\frac{E}{E_0} \tag{5.62}$$

where $A = f(\bar{n})$—coefficient dependent on shaft rotational speed (n): $\bar{n} = \frac{n}{n_0}\sqrt{\frac{T_{\text{inlet, 0}}}{T_{\text{inlet}}}}$ $E = \sqrt{1 - \left(\frac{\Pi - \beta \cdot B}{1 - \beta \cdot B}\right)}$ $\Pi = \frac{p_{\text{outlet}}}{p_{\text{inlet}}}$—pressure ratio, β—critical pressure ratio, $B = f(\bar{n})$—coefficient, $_0$—means the nominal parameters of a group of stages.

For $\beta \approx 0$ with low values of Π_0, the equation can be re-written as follows:

$$\frac{m}{m_0} = A \cdot \frac{p_{\text{inlet}}}{p_{\text{inlet, 0}}}\sqrt{\frac{T_{\text{inlet, 0}}}{T_{\text{inlet}}}}\sqrt{\frac{1 - \Pi^2}{1 - \Pi_0^2}} \tag{5.63}$$

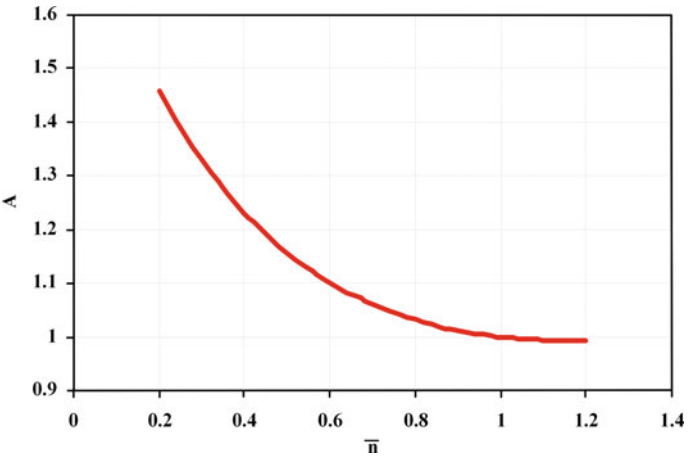

Fig. 5.78 Coefficient A of the characteristics of a group of turbine stages

and finally:

$$p_{\text{inlet}} = \sqrt{p_{\omega}^2 + \left(\frac{m}{m_0}\right)^2 \cdot p_{\text{inlet},\,0}^2 \cdot \sqrt{\frac{T_{\text{inlet},\,0}}{T_{\text{inlet}}}} \cdot \left(1 - \pi_0^2\right) \cdot A^{-2}} \tag{5.64}$$

Additionally, the following relationships should be applied:

$$\overline{n} = \frac{n}{n_0} \cdot \sqrt{\frac{j_{\text{inlet},\,0}}{j_{\text{inlet}}}} \qquad \overline{\eta} = \frac{\eta}{\eta_0} \qquad X = \frac{\Pi - 1}{\Pi_0 - 1}$$

$$\Pi = \frac{1}{\pi} \qquad \pi = \frac{p_{\text{outlet}}}{p_{\text{inlet}}} \qquad \sqrt{\frac{j_{\text{inlet},0}}{j_{\text{inlet}}}} \approx \sqrt{\frac{T_{\text{inlet},0}}{T_{\text{inlet}}}}$$

$$\overline{\overline{n}} = \frac{\overline{n}}{\overline{n}opt} \qquad \overline{\overline{\eta}} = \frac{\overline{\eta}}{\overline{\eta}_{\max}}$$

$$\overline{\overline{\eta}} = 1 - \left(1 - \overline{\overline{n}}\right)^{a_1} \qquad for \qquad \overline{\overline{n}} < 1$$

$$\overline{\overline{\eta}} = 1 - a_3 \cdot \left(1 - \overline{\overline{n}}\right)^{a_2} \qquad for \qquad \overline{\overline{n}} < 1$$

For the turbine working in the SOFC–GT, exemplary factors which can be used in the equations given above are $a_1 = 4.2$ $a_2 = 1.7$, and $a_3 = 0.14$. Coefficients $A = f(\overline{n})$, $\overline{\eta}_{\max} = f(X)$, and $\overline{n}_{\text{opt}} = f(X)$ are shown in Figs. 5.78, 5.79 and 5.80.

5.4 Triple-Generation Applications

In addition to the classical concept of co-generation, which usually regards the common generation of electricity and heat, there is the notion of tri-generation or triple-generation referring to the production of electricity, heat and cold and the logical extension of poly-generation.

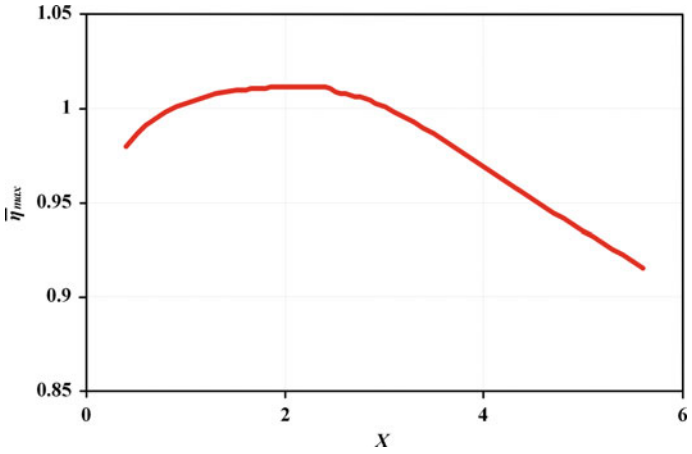

Fig. 5.79 Coefficient $\overline{\eta}_{\max}$ of the characteristics of a group of turbine stages

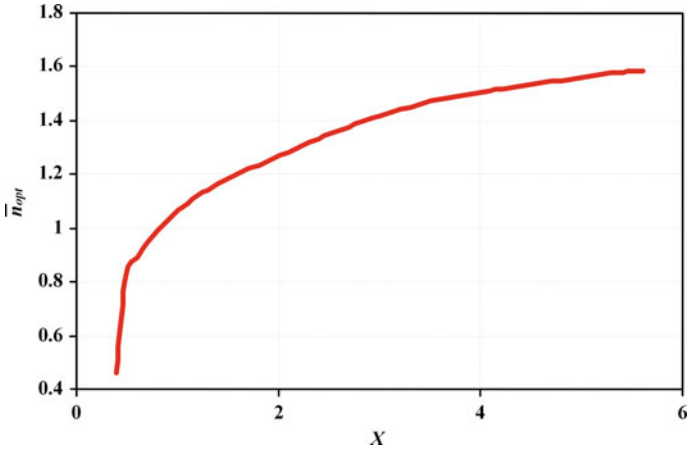

Fig. 5.80 Coefficient $\overline{n}_{opt}$ of the characteristics of a group of turbine stages

The main advantage of triple-generation is that it covers the annual demand for heating and cooling (Fig. 5.81). Cold (in the form of ice-water), can be produced either in a centralized system— directly in the plant and sent to customers or in a distributed system—or produced directly by customers using the hot water network. Tri-gen systems may be used in small scale applications—for instance in an office building, supermarket or even a small house.

Tri-gen is the simultaneous generation of electricity, heat and cooling. It is a technology derived from the known technology of combined heat and power generation (CHP). This combination enjoys lower fuel consumption than separated

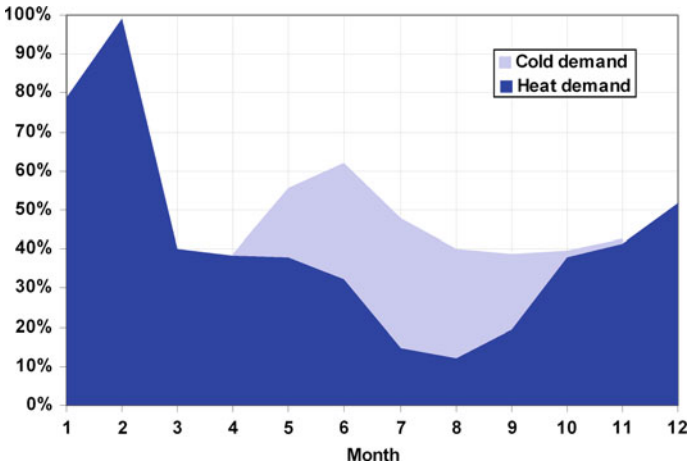

Fig. 5.81 Typical heat and cold demands change during a year

Fig. 5.82 The idea of a triple-generation unit

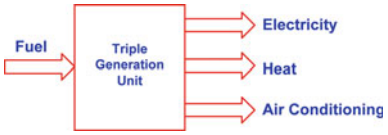

Fig. 5.83 Scheme of realization of triple-generation system

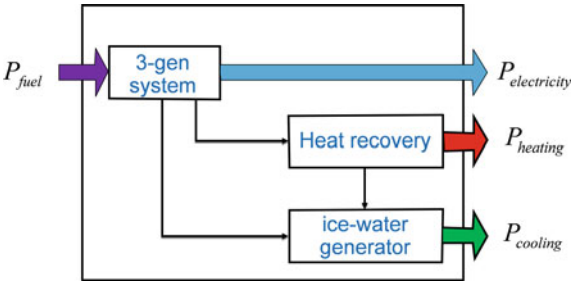

generation, which translates into increased energy conversion efficiency. The triple-generation concept is shown in Fig. 5.82.

Fuel cells generate electricity during electrochemical processes. Simultaneously, they emit flue gases and a range of high temperatures. This source of heat can be used for additional generation, both heating and cooling water (see Fig. 5.83).

High temperature fuel cells, like SOFC or MCFC, can be used both for generating electricity and for tri-gen. Their distinctive feature is relatively high temperature flue gas, which allows heat to be recovered both for the district heating water and chilled water production. An exemplary scheme of such a system is shown in Fig. 5.84.

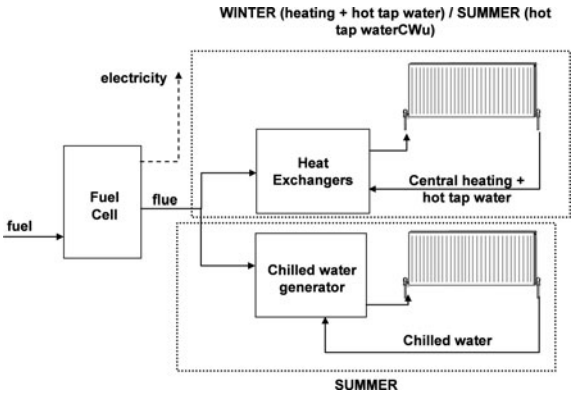

Fig. 5.84 Simplified scheme of a tri-generation system with a high-temperature fuel cell

A tri-gen system based on a high temperature fuel cell module is best-suited to supply the energy needs of office buildings because it meets 50% of total energy consumption of the building. The remaining heat is used for heating in the winter season and cooling (air-conditioning) in the summer season. The fuel cell produces electricity with 50% efficiency, the rest of the thermal energy being directed to a heat exchanger for water heating purposes.

In winter, water from the heat exchanger is used for space heating through radiators or warm air ducts. The typical water temperature required for radiators in winter is 70°C with a return temperature of 40–50°C. It is possible to heat the ice-water generator directly using exhaust gas from the fuel cell but this solution needs two different heat exchangers: gas-fluid for water heating in winter and a second gas-fluid heat exchanger for ice-water generation. A gas-fluid heat exchanger needs a larger heat exchange area than a fluid–fluid heat exchanger. It is better to use one gas-fluid heat exchanger (for water heating only) plus two fluid–fluid heat exchangers than to use two gas-fluid heat exchangers.

In summer, hot water is directed to an ice-water generator which produces ice-water (with temperature of 6°C) directed to radiators and/or cool air delivered to accommodation areas. Absorption chiller based ice-water generators need temperature ranges of inlet water of: 110°C and 160°C for a one stage or two stage ice-water generator, respectively. Returning water has a temperature of 75°C. An ice-water generator can be based on a standard compressor based chiller.

5.4.1 Chillers

5.4.1.1 Absorption Chiller

In the absorption chiller, the vapor of the refrigerant produced in the evaporator is not compressed mechanically as it is in commonly used vapor-compression chillers, but is absorbed instead by a lean solution under low pressure inside

the absorber, thus producing a rich solution. Two substances are used in the absorption machine: the refrigerant and a relatively non-volatile solvent. The temperature difference between the source of heat (regenerator) and the heat sink (absorber) is obtained by maintaining a different concentration of refrigerant in the solvent in the two parts of the apparatus. Heat is absorbed in the regenerator by evaporating the refrigerant from a concentrated solution of the non-volatile solvent. Heat is rejected at a lower temperature by absorbing the refrigerant from the refrigerator coils in the low-concentration solution from the regenerator. The temperature of the condensing refrigerant in the condenser determines the pressure in the regenerator, and similarly the temperature of evaporating refrigerant in the refrigerator coils fixes the pressure in the absorber. The pressure will be higher in the regenerator, and a pump is needed to circulate the concentrated solution from the absorber to the regenerator. The temperatures of the available cooling water and heat supply determine the temperatures in these two pieces of equipment (Fig. 5.85).

The refrigerant of the absorption systems should meet the following requirements:

- Good solubility in absorbent in the absorber's temperature range;
- Poor solubility in absorbent in the desorber's temperature range;
- Inability to react irreversibly with the absorbent in the operational temperature range.

The corresponding requirements for the absorbent are: low saturation pressure compared to the refrigerant and low thermal capacity. Currently, no known substance fulfills all above requirements. The absorbent/refrigerant pairs most frequently encountered in the absorption chillers are: water/ammonia and lithium bromide aqueous solution/water. The thermal characteristics of the water/ammonia mixture are shown in Fig. 5.86.

Absorption chillers utilize pairs: silica gel/ammonia, activated carbon/ammonia, activated carbon/methanol and molecular sieves (zeolites)/water. The above substances display the best sets of properties available thus far, but research on

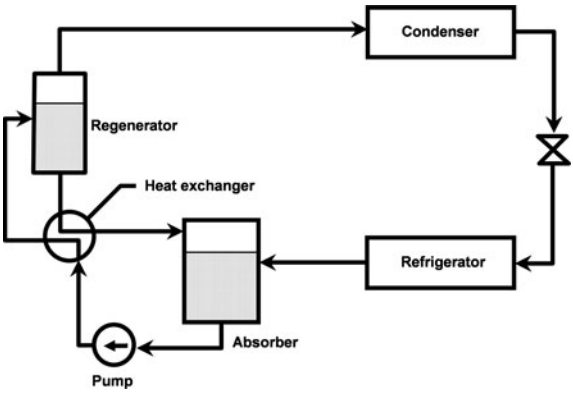

Fig. 5.85 Schematic diagram of an absorption refrigeration machine [47]

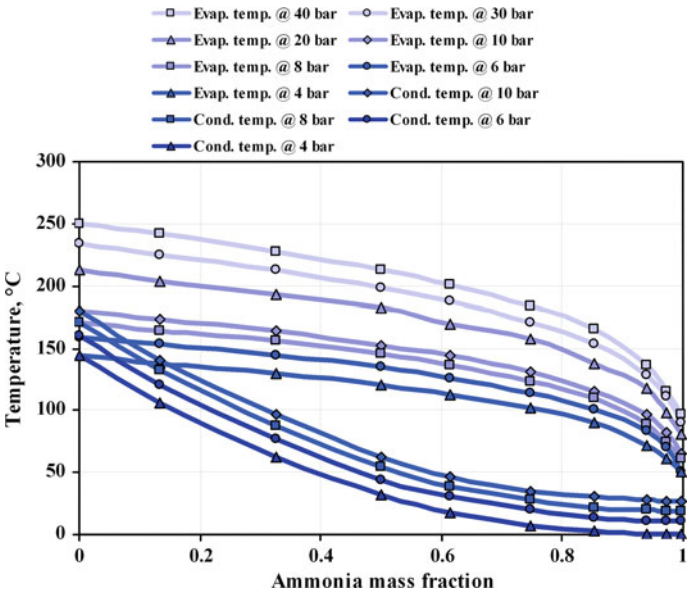

Fig. 5.86 Ammonia/water mixture characteristics

finding better pairs continues. For instance, the pairs lithium chloride/water or lithium bromide + lithium nitride + lithium iodide + lithium chloride/water are being considered for use in absorption solutions.

The boiling pot is powered by hot water, steam or hot flue gas to degasify the refrigerant from the solution. A typical T–Q (Temperature–Heat) diagram of the evaporation process is shown in Fig. 5.87. From the boiling pot the lean solution is throttled and sprayed in the absorber in order to increase the surface, which absorbs the refrigerant vapors again.

During the absorption process heat is generated and recovered by the cooling water flowing through the absorber's piping. Refrigerant vapor created in the boiling pot is liquidized in the condenser, while the heat is recovered by the cooling water, already warmed up by the absorber's heat. An exemplary T–Q diagram of the condenser is shown in Fig. 5.88. After being expanded in a valve, the refrigerant flows to the evaporator, where it collects heat from the chilled water. The refrigerant vapor created is delivered to the absorber, where it is again absorbed by the solution.

In order to improve the performance of the absorption chiller, a counter-current heat recovery exchanger is used (see T–Q diagram presented in Fig. 5.89 for details), where the rich solution pumped to the boiling pot is warmed up by the lean solution flowing to the absorber. When the water/ammonia mixture exchanges heat with the water it generates very non-linear T–Q charts with the heat transfer equipment. In contrast, T–Q has linear characteristics when the heat exchanger works with the mixture at both sides.

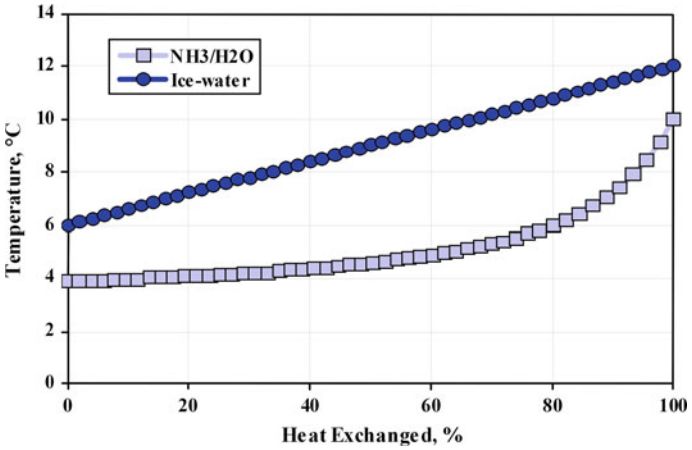

Fig. 5.87 T–Q chart of the evaporator

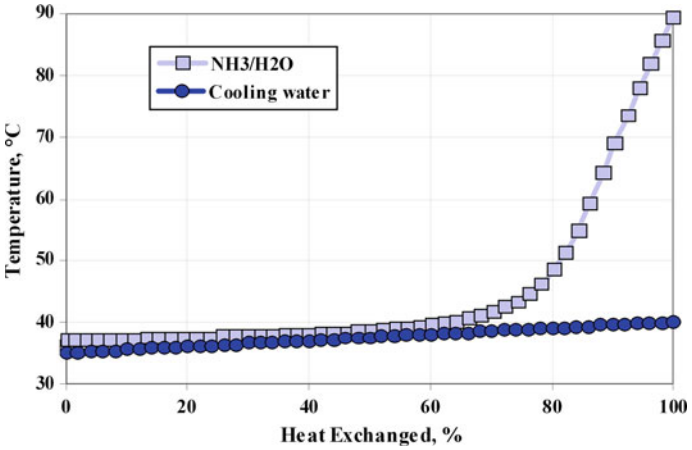

Fig. 5.88 T–Q chart of the condenser

The main heat exchangers of an absorption chiller are: condenser, boiling pot (desorber), evaporator and absorber. These elements can be installed inside a single or double jacket, depending on the type and size of device (see Fig. 5.90). Large plants incorporate the double jacket solution, which enables easier transportation and installation. Additional elements of a chiller are: a counter-current heat exchanger (for heat recovery), solution circulation pump, refrigerant circulation pump and valves, and a control expansion valve (throttle).

A model of an absorption chiller working on a water–ammonia mixture should subsequently be optimized to achieve the highest possible coefficient of performance (COP):

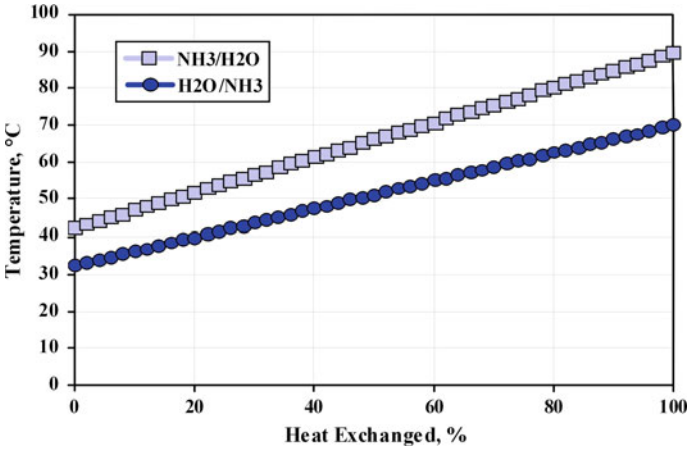

Fig. 5.89 T–Q chart of the heat exchanger

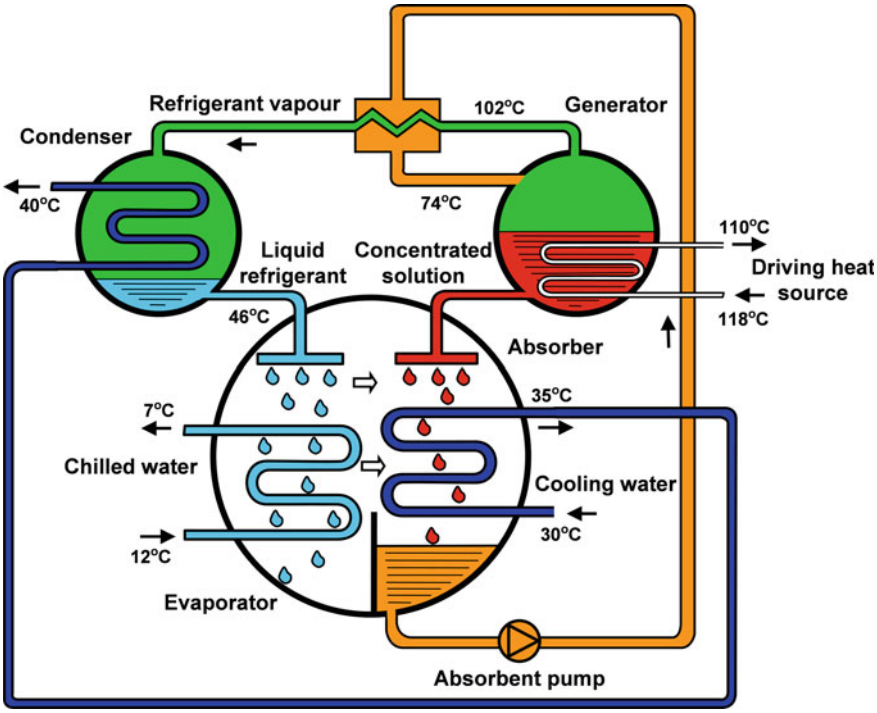

Fig. 5.90 General scope of absorption chiller

$$COP = \frac{Q_{\text{Chilledwater}}}{Q_{\text{Heat}}} \tag{5.65}$$

The optimized parameters are: pressures of the working agent before and after the expansion valve. The absorber refrigeration machine achieves a COP of 1.41. Optimization should be carried out separately for each type of heat source (e.g. fuel cell type) connected to the chiller, due to the different composition and temperature of the flue gas delivering the heat to the chiller in each case.

5.4.1.2 Compressor based Chiller

The parameters of the chiller vary depending on the substances used. They have an impact on the temperature of the refrigerant, coefficient of performance and dimensions of the device (Fig. 5.91). Desirable values can be determined. So the most desirable refrigerant in vapor chillers should have the following properties:

- Low thermal capacity to maximize circulation;
- Low specific volume to minimize chiller dimensions;
- Good transferring properties in the appropriate temperature range–low viscosity;
- High surface film conductance during condensation and boiling (small heat exchangers);
- Overpressure in the evaporator at the lowest required evaporation temperature (prevents air and water contamination of the system);
- Non-corrosive in the required temperature range;
- Allowing for easy detection of leaks in the system;
- Atoxic;
- Harmless for the environment;
- Incombustible and inexplosive;
- Low solidification point and high critical point;
- Low price.

In the case of compressor based chillers, the most popular working agent was Freon R-22 ($CHClF_2$), currently replaced by R-134 ($C_2H_2F_4$).

A model of the compressor based chiller should be subsequently optimized in order to achieve the highest possible COP:

$$C.O.P = \frac{Q_{\text{Chilledwater}}}{P_{\text{Compressor}}} \tag{5.66}$$

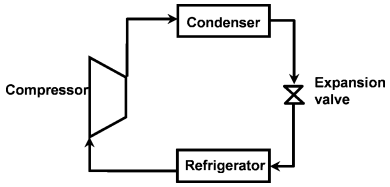

Fig. 5.91 Scheme of compressor based chiller

5.4.2 SOFC Based Triple-Generation System

Performance of the tri-generation system is closely related to the object to which the media are delivered, mainly the ratio between electricity and heat/cooling. The same tri-generation system can display good parameters when delivering media to one object and simultaneously have poorer performance while cooperating with a different facility. Therefore the performance of the tri-generation systems was presented in a way allowing their key parameters to be determined for any facility with known electricity, heat and cooling demands (Table 5.8).

An SOFC-based tri-generation system was analyzed under two working regimes: summer and winter. The system was designed to work with an office building (A-class) with electricity demand of 6 MW. During the summer (see Fig. 5.92) the tri-generation system meets all electricity demand and additionally produces 720 kW (10%) of ice-water. During winter (see Fig. 5.93) the tri-generation gives the same power and 4.3 MW (40%) of warm water with inlet and outlet temperatures 60°C and 90°C, respectively.

As an example of a commercially available unit, a SOFC based triple-generation module made by Siemens is located on the premises of TurboCare in Turin. A chart of the system is presented in Fig. 5.94. This unit has a relatively long history and has operated at a few locations in Europe. A photo of the device and operational data of the unit are presented in Fig. 5.95 and Table 5.9, respectively.

Table 5.8 Main parameters of the compressor based chiller

Parameter	Value
C.O.P	3.24
The pressure in the evaporator (bar)	5.1
The pressure in the condenser (bar)	19.0

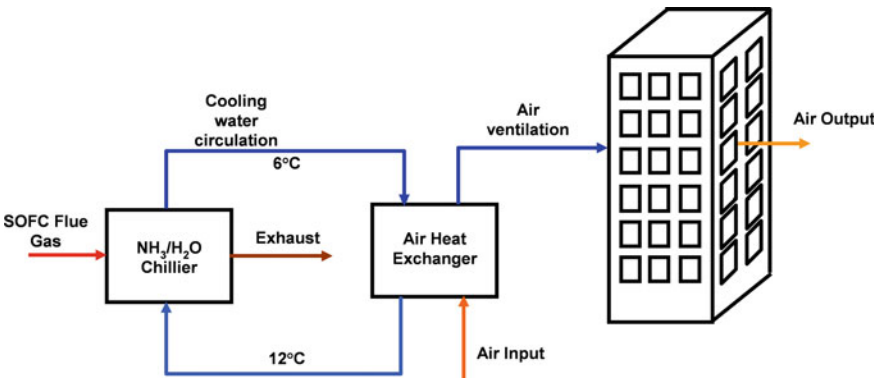

Fig. 5.92 Tri-generation system during summer

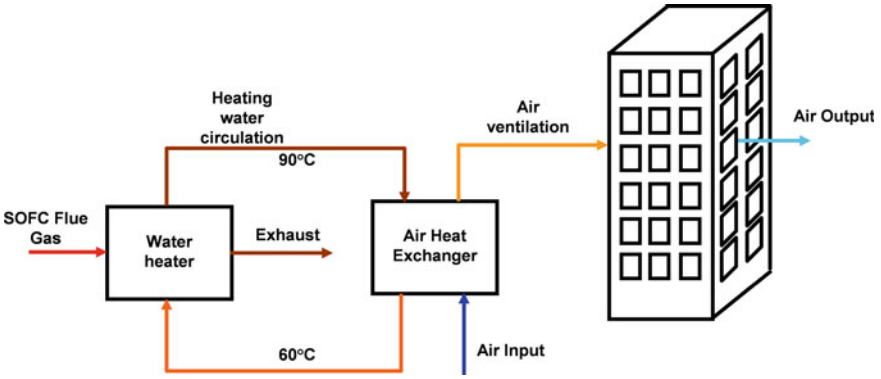

Fig. 5.93 Tri-generation system during winter

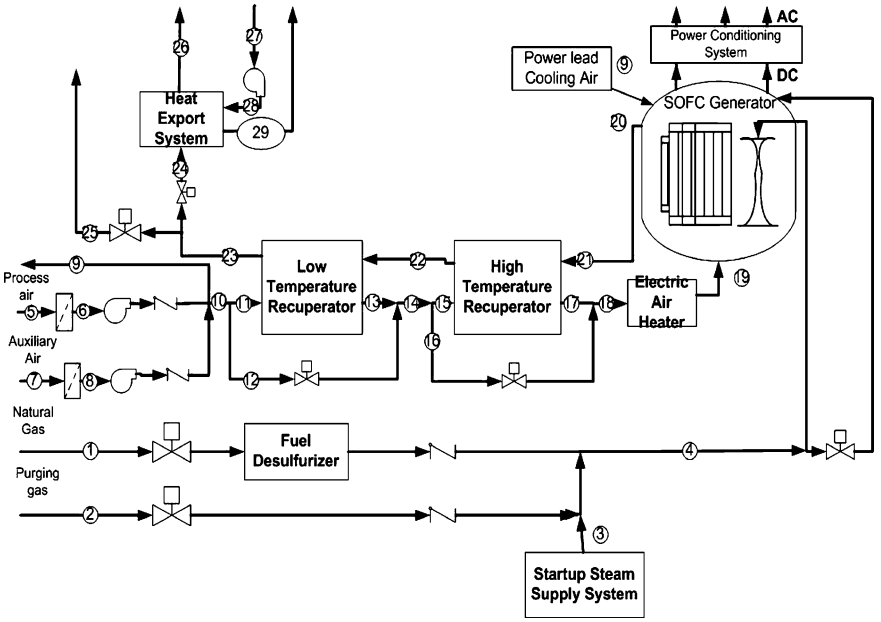

Fig. 5.94 Flow chart of the CHP 100 SOFC Generator by Siemens at turbocare in Turin

5.5 Simulation of Bio-Fuels as Fuel for SOFC

Hydrogen and Natural gas are currently considered to be the main fuels for fuel cells. Hydrogen is an ideal fuel in terms of fuel cell working conditions. Unfortunately, hydrogen is not present in the environment in an uncombined form and there are difficulties with production, transportation and storage. Natural gas,

Fig. 5.95 The CHP 100 SOFC generator by Siemens at turbocare in Turin

Table 5.9 CHP-100 SOFC Generator operational data

Parameter	Value
Run hours in EOS test room	16 410
Total Run hours (Netherlands and Germany)	36 890
Generated energy, AC, to date in TurboCare (MW h)	1 662
Voltage, DC (V)	250
Current, DC (A)	500
Power, DC (kW)	125
Average stack temperature (°C)	925
Heat generation (hot water at 80°C) (kW)	60–70
Ice-water temperature (°C)	7
Availability (%)	99.1
Electric efficiency (AC) (%)	42–44
CHP efficiency (%)	70–75

meanwhile, is considered to be an interim fuel due to limited resources. The most plausible future scenarios in the power markets are as follows:

1. Abandoning gas/liquid/solid fuels in favor of electricity generated by renewable sources and/or nuclear plants. In this case, the energy distribution role will be provided by the power grid, and the storage role by consumers,
2. Production of plant-derived gas/liquid fuels based on the cultivation of plants and shrubs, such as Salix Viminalis, and their conversion into fuel, e.g. alcohols.

Since using electricity alone would be problematic (e.g. airplanes), the cultivation of energy seems to be one of the most possible scenarios for the future. Hence, one of the most plausible future scenarios in the power markets is the production of gas/liquid fuels, such as alcohols, derived from specially cultivated plants and shrubs, such as Salix Viminalis. The advantages of this approach include: easy storage, existing distribution network, easy to implement in the transport industry (especially in airplanes) and potential eco-friendly aspects.

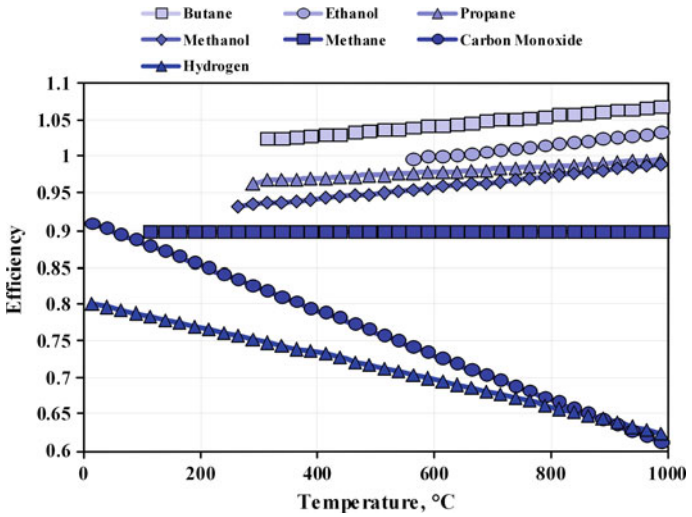

Fig. 5.96 The theoretical maximum efficiency of fuel cells, depending on the fuel used

Hydrogen and methane are being considered as fuels for fuel cells at present. The use of biogases in fuel cells is relatively poorly investigated. Some data can be found in [31–33]. Most developments regard singular cell tolerance on impurities or biogas content. Mainly, the investigations are focused on biogas taken from sewage treatment plants or gasifiers. In many cases the biogas is first reformed to hydrogen and the hydrogen is then delivered to the cell.

The use of bio-fuels as a fuel in fuel cells has been relatively poorly explored. A few results have been obtained from simulations and experiments for SOFC in [31–40]. The main consideration in these studies of bio-fuel is bio-gas from sewage or gasifier. In many cases, bio-fuel is subjected to hydrogen reforming processes [41, 42], and only hydrogen is supplied to the cells. Theoretical analysis [43] was also carried out with regard to reforming of bio-fuel for a phosphoric acid fuel cell (PAFC).

In a fuel cell electrochemical reactions take place leading to the direct conversion of chemical energy to electricity. The type of reaction that takes place plays a crucial role and, depending on its course, the fuel cell can achieve higher or lower efficiency. Exothermic reactions are characterized by the fact that the heat generated is put into the environment, whereas endothermic reactions absorb heat from the environment. Fuel cell efficiency is often based on only the chemical energy of the fuel delivered; with such a definition, the heat supplied from the environment may result in the achievement of efficiency values above unity. Fig. 5.96 shows the theoretical efficiency of fuel cells from the supply of various compounds.

Long hydrocarbon chain bio-fuels are characterized by a relatively high potential for efficiency. However, there is a lot of chemical reaction on the fuel cell

at any time, which generates various voltages, and the efficiency level is the result of these reactions.

5.5.1 Bio-Fuels

Bio-fuel is defined as a solid, liquid or gaseous fuel obtained from relatively recently lifeless or living biological material and differs from fossil fuels, which are derived from long dead biological material. Based on mathematical modeling, the analysis considers bio-fuels obtained from biomass gasification as well as fermentation processes. Taken into consideration were the following bio-fuels: biogases (Anaerobic digester gas—ADG, Landfill gas—LFG); bio-liquids (methanol, ethanol, canola oil); solids—wood. Hydrogen and methane were used as reference fuels.

5.5.1.1 Gaseous Biofuels

Anaerobic digestion gas (ADG) is the end-product of a series of processes in which micro-organisms break down biodegradable material in the absence of oxygen, and is produced mainly by waste-water treatment plants. ADG is highly corrosive, with a calorific value of about 60% of the calorific value of natural gas, or approximately 25% propane. Due to its low calorific value and high corrosiveness ADG storage is not practiced, so all plant using this power source must be located close to the place of production.

Landfill gas (LFG) is produced by wet organic waste fermentation under anaerobic conditions in a landfill site. The waste is covered and compressed both mechanically and by the weight of the material that is deposited above. This material prevents oxygen from accessing the waste, thereby encouraging anaerobic microbes to thrive and produce gas, which slowly escapes and is captured. This gas may contain trace amounts of nitrogen, oxygen, ammonia, sulfates, hydrogen, carbon monoxide and highly toxic compounds such as tri-chloride ethylene, benzene, vinyl chloride. LFG is highly corrosive and is therefore difficult to transport. The amount of gas from the mining deck depends to a large extent on the type of waste and numerous environmental factors such as the O_2 content in the seams, moisture content and temperature.

ADG and LFG consist mainly of methane and carbon dioxide, exemplary compositions are listed in Table 5.10.

Table 5.10 Biogas composition

Component (%)	Landfill gas	Anaerobic digester gas
CH_4	54	63
CO_2	33	35
Other	13	2.0
Initial s/c ratio	0.15	0.02

5.5.1.2 Liquid Biofuels

The following liquid biofuels as fuel for fuel cells are mostly considered: alcohols (bio-methanol, bio-ethanol) and rapeseed oil.

Alcohols are organic compounds and hydrocarbons, in which hydrogen atoms are replaced by a hydroxyl group. The most common alcohols are mono-hydroxy with a homologous series of the general formula $C_nH_{2n} - OH$. Alcohols contain only single bonds and are obtained by hydration of olefins, hydrogenation of aldehydes, ketones, carboxylic acids, and biochemical methods (fermentation).

Two types of alcohols were investigated: bio-methanol and bio-ethanol. Methanol (methyl alcohol) is used as a solvent (soluble in fats, resins and varnishes), also used in the pharmaceutical component of fuel for aircraft (the main component of fuel), explosives (e.g. C4), as fuel in internal combustion engines such as speedway motorbikes, used with caustic solutions or acids to obtain methyl esters, a basic raw material for polyoxymethylene (polyoxymethylene, polyformaldehyde). Ethanol (ethyl alcohol) is widely used in food and pharmaceutical industries (alcoholic fermentation) and cosmetics; it is also used as a solvent. Alcohol may also be used to fuel diesel engines if there are good lubrication injector nozzles and the alcohol is mixed with a small (5–20%) amount of oil.

Canola is a cultivar of oilseed rape (*Brassica campestris*). Canola oil is considered an alternative fuel to diesel and is termed a bio-diesel. The oil is extracted from the seeds usually at an elevated temperature and consists mainly of long-chain hydrocarbon fatty acids (see Table 5.11 and Fig. 5.97). It is seen that canola oil is composed mainly of three fat acids: oleic, linoleic and alpha-linoleic.

Oleic acid (molecule scheme is shown in Fig. 5.98) is a pale yellow oily liquid, darkening when left in contact with air and insoluble in water. Oleic acid is mixed with organic solvents and reacts with hydroxides. In nature, it occurs as glycerol ester in large quantities in vegetable and animal fats.

Linoleic acid (see molecule shown in Fig. 5.99) belongs to a group of omega-6 unsaturated fatty acids. It too occurs in the form of glycerol ester in vegetable fats, and to a lesser extent in animal fats.

Alpha-linoleic acid (molecule structure is shown in Fig. 5.100) belongs to a group of omega-3 polyunsaturated fatty acids. It occurs as an ester of glycerol in small amounts in vegetable fats, especially flaxseed oil, and animal fats.

Table 5.11 Canola oil composition

Component	Chemical structure	Molar fraction (%)
Oleic acid	$CH_3 - (CH_2)_7 - CH = CH - (CH_2)_7 - COOH$	75
Linoleic acid	$CH_3 - (CH_2)_4 - CH = CH - CH_2 - CH = CH - (CH_2)_7 - COOH$	15
α-Linolenic acid	$CH_3 - CH_2 - CH = CH - CH_2 - CH = CH - CH_2 - CH = CH - (CH_2)_7 - COOH$	10

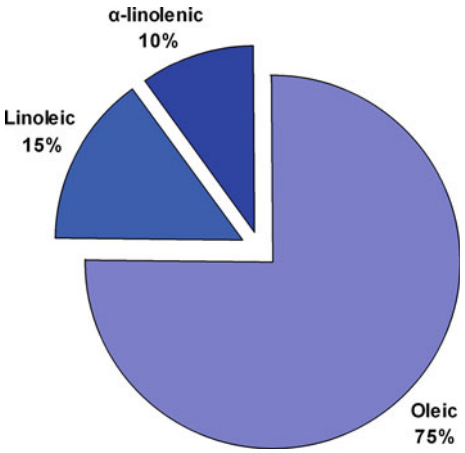

Fig. 5.97 Canola oil composition

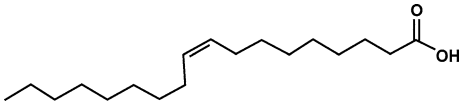

Fig. 5.98 Construction of oleic acid molecules

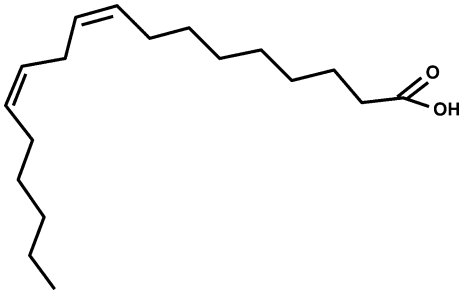

Fig. 5.99 Linoleic acid molecule

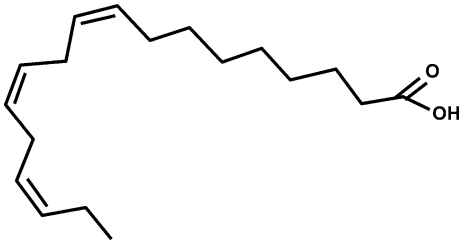

Fig. 5.100 Alpha-linoleic acid molecule

Schematic equations of fatty acid molecules used in the model as well as parameters obtained by model and comparisons against their real values are presented in Table 5.12.

A comparison of canola oil parameters against other fuels is presented in Table 5.13.

Table 5.12 Comparison of fat acid models against their real values

Parameter	Value given by the model	Real value	Difference (%)
Oleic acid			
Molecule equation	$CH_3 - (CH_2)_7 - CH = CH - (CH_2)_7 - COOH$		
Molar mass (kg/kmol)	282.5	282.5	0
Density (kg/m^3)	895	892	0.3
Boiling point (K)	633	487	20
Specific heat (kJ/kg)	2.1	1.9	9.5
Linoleic acid			
Molecule equation	$CH_3 - (CH_2)_4 - CH = CH - CH_2 - CH = CH - (CH_2)_7 - COOH$		
Molar mass (kg/kmol)	280	280	0
Density (kg/m^3	902	931	3.2
Boiling point (K)	502	764	52
Specific heat (kJ/kg)	n/a	1.9	n/a
alpha-linoleic acid			
Molecule equation	$CH_3 - CH_2 - CH = CH - CH_2 - CH = \cdots$ $\cdots = CH - CH_2 - CH = CH - (CH_2)_7 - COOH$		
Molar mass (kg/kmol)	278	278	0
Density (kg/m^3)	916	907	1.0
Boiling point (K)	184	281	21
Specific heat (kJ/kg)	n/a	1.9	n/a

Table 5.13 Canola oil as fuel

Parameter	Canola oil	Methyl ester of canola oil	Diesel oil
Density (kg/m^3)	886	880	860
Viscosity (mm^2/s (20°C)	74	7	3.5
Surface tension (kg/s^2) (20°C)	0.048	n/a	0.025
Calorific value (MJ/kg)	≈38	38.8	43
Flash point (°C)	>300	170	70

5.5.1.3 Solid Biofuel—Wood

Wood for power generation purposes is obtained directly or indirectly from forests in the form of wood, bark, needles and leaves. It can also be obtained from construction waste. Detailed sources:

- Forest wood, not previously used, composed mainly of leftovers from felling and cutting: tree stumps, waste wood and wood by-products such as bark, sawdust and wood chips;
- Recycled wood—container, formwork, construction material (from the demolition of houses).

The water content in wood varies from 20 to 60% and significantly affects its heating value. The water content of fresh wood depends mainly on tree species and is

Table 5.14 The average content of essential elements in wood (%)

Component	Wood origin	
	Softwood	Hardwood
Carbon	50.3	49.0
Oxygen	43.0	44.3
Hydrogen	6.00	6.00
Nitrogen	0.20	0.20
Minerals	0.50	0.50

Table 5.15 Wood composition

Component	Chemical structure	Molar fraction (%)
Cellulose	$\ldots - OH - CH_2 - (CH - O)_2 - (CH_2O)_2 - CH - \ldots$	50
Hemicelluloses	$\ldots - OH - CH_2 - (CH - O)_2 - (CH_2O)_2 - CH - \ldots$	24
Lignin	$\ldots - OH - CH_2 - CH = CH - (CH = C)_2 - OH - CH = C - CH_3O - \ldots$	23

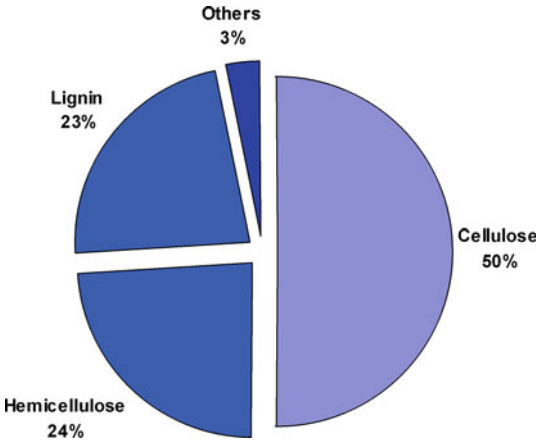

Fig. 5.101 Wood composition

higher for smaller wood specific gravity. The highest calorific value of dry wood is 19.2 MJ/kg (zero humidity). The calorific value decreases inversely to water content.

The main mass of wood is made up of organic matter, mainly four elements: carbon, hydrogen, oxygen, and nitrogen. On average, absolutely dry wood contains 49.6% carbon, 6.3% hydrogen and 44.2% oxygen with nitrogen (see Table 5.14). The nitrogen content in the wood averages 0.12%. In addition to organic matter in the composition of the wood depending on the species there are mineral substances in the range of 0.2–1.7%.

Raw knowledge about the main chemical elements in the composition of wood is insufficient to model gasification processes. The elements in question are mainly components of long chain hydrocarbons, like lignin, cellulose, and hemicelluloses (see Table 5.15 and Fig. 5.101). The structure of hemicelluloses is very similar to

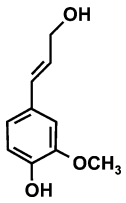

Fig. 5.102 Lignin molecule for modeling purposes

cellulose itself, so in the presented analysis it was assumed that, in the model, wood consists only of cellulose (75%) and lignin (25%).

Cellulose is an infinite network of interconnected particles in the structure. Since there is no possibility to take into account, in the model, compounds of infinitely long chains, only a basic component of the entire chain of cellulose was used the result as a model of cellulose.

Of the three main types of lignin molecules that occur in wood, the applicable model was the molecule shown in Fig. 5.102. The selected molecule has an intermediate number of atoms in relation to the other two.

5.5.1.4 Biomass Gasification

Some types of bio-fuels cannot be delivered to the SOFC directly, and in those cases, the gasifier should be used. There are many types of gasifiers (autothermal, aluthermal). An autothermal gasifier is fed simultaneously by oxygen and steam, the oxygen quantity is adjusted to achieve the desired temperature during the adiabatic process.

The gasifier characteristics were generated for both fuels: canola oil and wood. The characteristics are presented in Figs. 5.103 and 5.104. The syngas obtained by

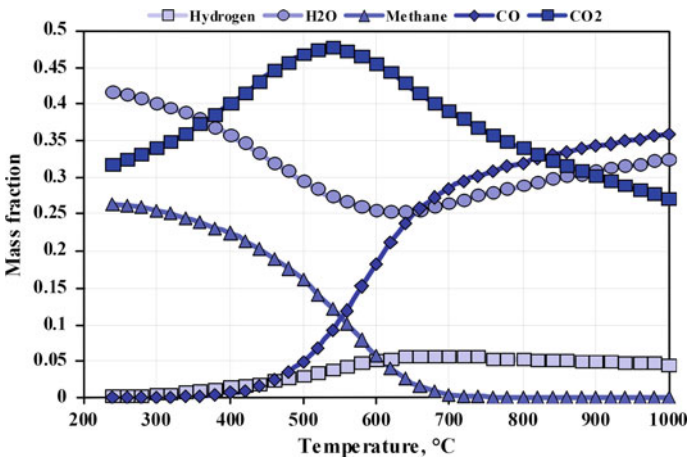

Fig. 5.103 Canola oil syngas composition as a function of temperature

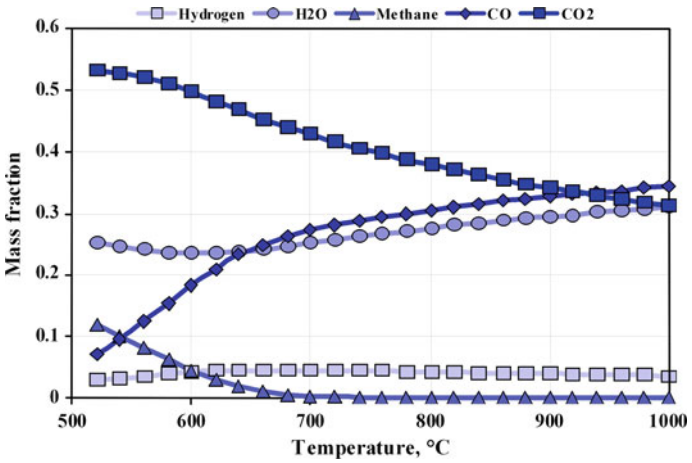

Fig. 5.104 Wood syngas composition as a function of temperature

Table 5.16 The composition of real gas from the wood gasification process

Component	Fraction (%)
Nitrogen	50–54
Carbon Monoxide	17–22
Carbon Dioxide	9–15
Hydrogen	12–20
Methane	2–3

biomass gasification is characterized by a high content of carbon monoxide (35%) and steam (30%), and a low content of hydrogen (5%); there is almost no methane A high inert gases content is also observed (carbon dioxide: 35%), which reduces its calorific value to 5.7 MJ/kg (for comparison, natural gas—55.9 MJ/kg, gasoline—44.1 MJ/kg). This low calorific value (as well as per volume unit) makes gas distribution in compressed form uneconomical, even when the gas does not cause corrosion.

A sample real composition of the synthetic gas obtained from wood is shown in Table 5.16, the gas was produced with the use of oxygen in the air, hence the large amounts of nitrogen.

5.5.2 Modeling SOFC Fueled by Bio-fuels

In order to determine the performance potential of fuel cells powered by bio-fuels, the resultsobtained were compared with two reference fuels: hydrogen and natural gas. Fuel cell characteristics for two reference fuels: hydrogen and methane were calculated for a comparative baseline. The type of fuel supplied is not the only

parameter affecting the performance of fuel cells. The most important parameters are: type of material used as the electrolyte, the thickness of the electrolyte, temperature of the cell surface, cell surface area in relation to the amount of fuel supplied, among others.

The use of bio-fuels to feed a fuel cell was tested on an appropriate mathematical model of a singular laboratory cell. This assumption allows the effect of the fuel used to be separated out exclusively and determined independent of other devices which form part of the whole system containing the fuel cell.

Most of the available experimental data and related results generated by the various models in fact refer to the off-design operation of the fuel cell. Studies which investigate the impact of fuel under off-design operation seek to obtain results in terms of the tolerance of given cells to the new fuel type. To estimate the potential of various fuels for fuel cell feeding, a design point class of models should be used. In those models, the characteristic parameter of the fuel cell is the fuel utilization factor (see Sect. 5.1) instead of the current density. This means that the comparison is made between two cells with the same fuel utilization factor and not the same area. This approach seems more reasonable and could be used to identify the real potential of bio-fuels in fuel cell use.

With currently built and tested devices, the most widely used material for the electrolyte is YSZ. Therefore this material has been chosen to study bio-fuel fueled SOFC. Achievable levels of fuel utilization factor in cells used commercially reach 80%. Other cell parameters were fixed as follows: electrolyte thickness of 15 μm, maximum current density (i_{max}) of 2.6 A/cm^2, cell working temperature of 800°C, and cell pressure at atmospheric pressure. During the analysis of the oxidant, flow was kept at a constant excess air factor (λ) of 3.

The analysis was performed for the following fuels:

1. Hydrogen
2. Methane
3. ADG
4. LFG
5. Bio-methanol
6. Bio-ethanol
7. Canola oil syngas
8. Wood syngas

Syngases (canola oil and wood based) and methane, prior to entering the fuel cell, are mixed with steam to obtain a steam to carbon ratio of 1.4. The structure of feeding the fuel cell syngases and methane is shown in Fig. 5.105.

Fig. 5.105 Structure of feeding the fuel cell by bio-gases and methane

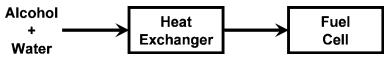

Fig. 5.106 Structure of feeding the fuel cell with alcohols

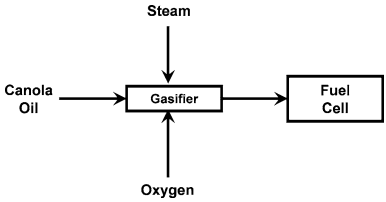

Fig. 5.107 Structure of feeding the fuel cell with canola oil

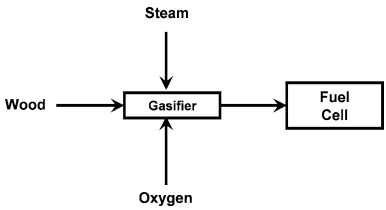

Fig. 5.108 Structure of feeding the fuel cell with wood

Bio-methanol before entering the SOFC is pre-mixed with water and then evaporated (see Fig. 5.106 for details). Relevant data on the ratio of steam to methanol to avoid carbon deposition are given in Fig. 5.37 (for definition see Table 5.4). During the simulations the molar ratio of steam to methanol was assumed at 1 (i.e. 50% aqueous solution of methanol as fuel). For this value and above 130°C, there is no risk of carbon deposition. High temperature fuel cells can operate at a somewhat lower ratio of water to methanol.

Bio-ethanol, like bio-methanol, should be pre-mixed with water in a ratio to avoid carbon deposition on the surfaces of electrodes. An appropriate factor is defined in Table 5.4 and its values for various temperatures are given in Fig. 5.38. The molar ratio of steam to ethanol to avoid carbon deposition was set at a value of 3: for this value and temperature above 200°C there is no risk of this phenomenon.

The compositions of gases used in the analysis are listed in Table 5.10. The canola oil based syngas composition was obtained for a temperature of 800°C, and its composition is shown in Fig. 5.103. The composition synthesis gas obtained by the wood gasification process at 800°C is presented Fig. 5.104. Structures for feeding a fuel cell canola oil and wood are shown in Figs. 5.107 and 5.108, respectively.

Generally speaking, bio-fuels are characterized by lower efficiency and a lower optimum fuel utilization factor than methane. The SOFC fueled by LFG, ADG and alcohols outperforms both canola oil and wood. The highest open circuit voltage is achieved with hydrogen, but that does not automatically translate into the greatest efficiency for higher fuel utilization factors.

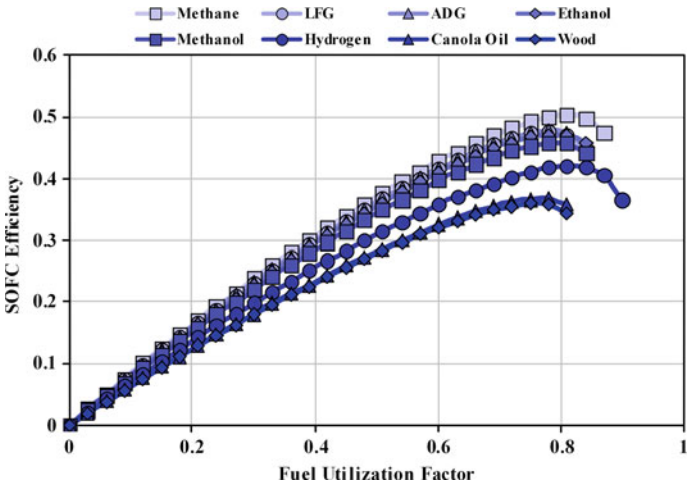

Fig. 5.109 SOFC efficiency vs. fuel utilization factor for various biofuels

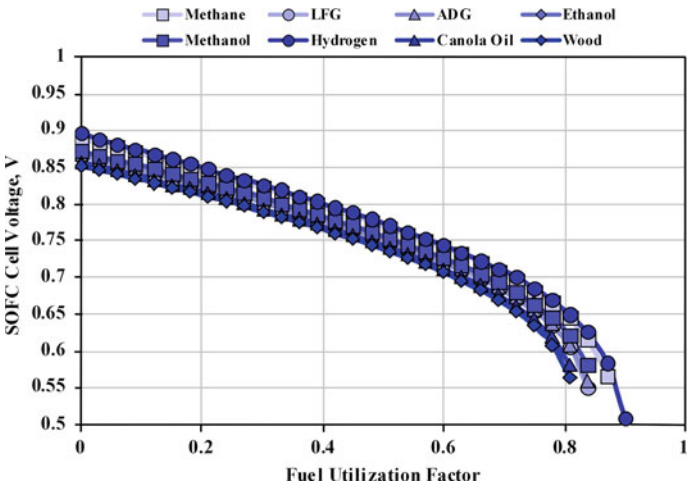

Fig. 5.110 SOFC voltage vs. fuel utilization factor for various biofuels

SOFC voltages and obtained efficiencies for various fuels are shown in Figs. 5.109 and 5.110. The figures contain the cell voltages and efficiencies for various fuels as a function of the fuel utilization factor. The highest level of efficiency (50%) is obtained for methane as a fuel, whereas syngases are characterized by much lower performances (35%). The highest optimum fuel utilization factor is for hydrogen as a fuel (80%), and the lowest one is for canola oil syngas (75%).

Internal reforming of methane involves the chemical conversion of process heat into a fuel (hydrogen), and it achieves higher SOFC efficiency than is the case with

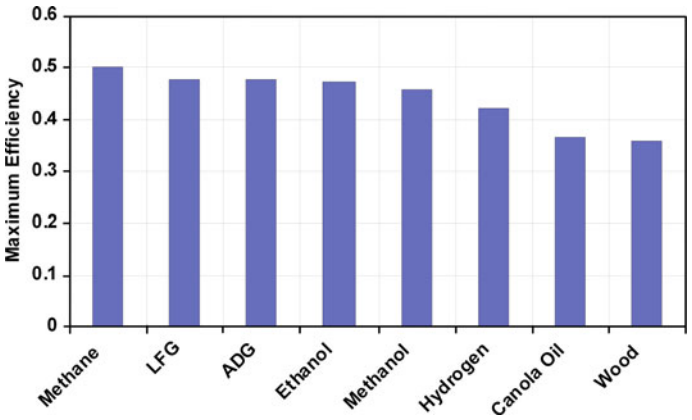

Fig. 5.111 Comparison of SOFC fueled by biofuels—maximum efficiency

Table 5.17 Comparison of bio-fuels as fuels for SOFC

Fuel	E_{OCV} (V)	Maximum efficiency (%)	Fuel utilization factor at maximum efficiency (%)
ADG	0.90	50	80
LFG	0.90	50	80
Bio-methanol	0.90	45	80
Bio-ethanol	0.90	47	80
Canola oil	0.85	35	75
Wood	0.85	35	75

dry hydrogen (see Fig. 5.111) even though hydrogen has the highest maximum voltage of all the fuels analyzed (see Fig. 5.112) (Table 5.17).

5.5.3 Economic Issues of Biofuels as Fuel for SOFC

Cash flow forecasting is a key element in determining the feasibility of an investment. The main costs involved in power plant projects are up-front outlays and primary fuel supplies. Revenues take the form of proceeds from sale of electricity and heat. All those elements rely heavily on project-specific conditions. This section presents a simplified feasibility analysis of fuel cells powered by bio-fuel. To provide a comparison, other concepts were also analyzed: reciprocating engine technology and natural gas as fuel (see Table 5.18). The use of traditional devices—reciprocating engines being the most popular of which—can be seen as an alternative to using fuel cells for bio-fuel energy conversion. An alternative for bio-fuel can be found in traditional fossil fuel, utilized either in fuel cells or traditional devices.

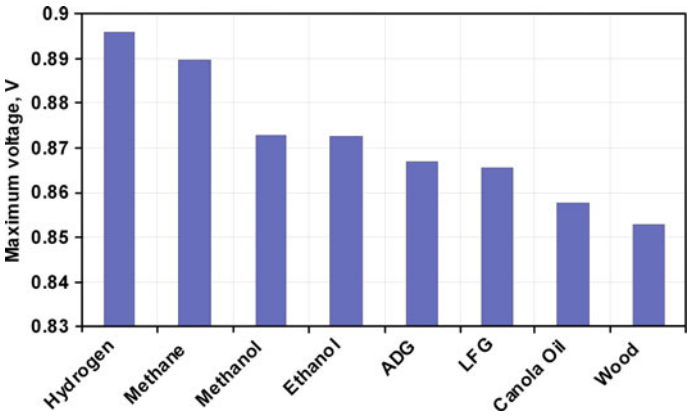

Fig. 5.112 Comparison of SOFC fueled by biofuels—maximum voltage

Table 5.18 Main parameters of discussed fuels

Property	Bio-ethanol	Natural gas
Density at 15°C (kg/m^3)	790	–
Heating value	19.59 MJ/l	34.4 MJ/m^3
Price	\$0.86/dm^3	Tariff
	\$43.9/GJ	\$9/GJ

Bio-ethanol was chosen because it can be used in fuel cells and in ICE (albeit requiring some modification of the engine and/or mixing with additional substances).

Usually, the following two economic indicators are used to assess the effectiveness of an investment: Net present value (NPV) and internal rate of return (IRR). In practice, it is difficult to compare different investments on the basis of only one indicator because NPV depends on the value of investments (not comparable for two investments with different initial values) whereas IRR value is determined at the end of the project. Additionally, NPV is sensitive to the assumed discount rate; in contrast IRR is independent of the value of the initial investment and independent of the discount rate. A financial profile can be prepared for NPV which shows a very good return on the investment process over the period. Since cash flows were calculated according to the free cash flow for the firm (FCFF) formula , no financial costs were included.

The analysis is based on the assumptions that the economic life of the investment is 15 years and the residual value at term is \$0.

It is difficult to give fuel prices for bio-fuels, because there is no market at present for some of them. The most popular bio-fuel is bio-ethanol which is used currently in many countries as an alternative to gasoline. Figure 5.113 shows the cost of bio-ethanol production in different countries. It should be noted that the cost of production does not translate automatically itself into fuel price.

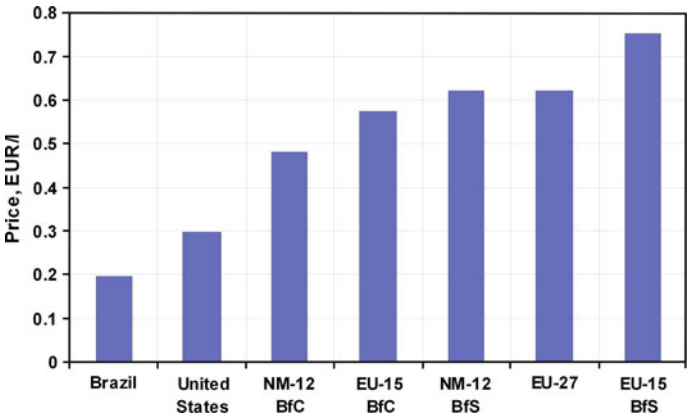

Fig. 5.113 The cost of bio-ethanol production in different countries

Table 5.19 Comparison of selected biofuels and conventional fuels

Parameter	Bio-fuels				Traditional Fuels	
	Canola oil	Bio-ethanol	Wood	Sewage waste	Diesel	Natural gas
Density at 15°C(kg/m^3)	860–900	790	150–400	130–160	820–845	–
Calorific value (GJ/m^3)	34	20	3	1.2	38	0.034
Cost ($/GJ)	16	44	4.0	−5.6	31	9.0

A comparison of selected fuels in terms of their cost versus chemical energy is presented in Table 5.19. It should be noted that in the case of bio-ethanol for piston engines, the fuel must contain additives (e.g. 15% gasoline).

In the case of wood, canola oil a gasification plant must be built. The cost of the gasification plant together with an air separation unit (ASU) with a capacity of 20 kg/s of municipal waste is $52 M. With a calorific value of fuel at 8 MJ/kg, the installation costs of the unit are $400/kW. Also included in the costs is that some additional compounds need to be delivered to a sewage waste gasification plant: about 2% of CaO (at $5.2/tonne) and 2% of SiO_2 (at $545/tonne), what gives about $9.1/tonne of fuel. To function, the gasifier requires an electricity source; it was estimated that 10% of the electricity produced is consumed by the gasifier.

The electricity market is fairly well defined, so the electricity sales price can be determined with a high reliability, but depending on the country and the particular circumstances there may be substantial differences (Table 5.21).

In order to determine profitability it is assumed that all electricity produced is earmarked for own use. Therefore, the revenue side will be called the "avoided costs" of purchasing electricity. The unit rate of electricity adopted is that for the purchase of electricity in the industrial sector. The price for electricity was

Table 5.20 Comparison of maximum efficiency values for SOFC with various fuels

Efficiency (%)	SOFC		Reciprocating engine	
	Total	Electric	Total	Electric
Bio-ethanol	90	47.2	93	37
Natural gas	90	50.2	93	39
LFG	90	47.7	–	–
ADG	90	47.6	–	–
Hydrogen	90	42.0	–	–
Canola oil	90	36.6	–	–
Wood	90	35.9	–	–

Table 5.21 Comparison of investment costs for various power plants

	Fuel	Total investment cost ($/kW)	Operation and maintenance cost
Reciprocating engine	Natural gas	1,400	0.010$/kW h
	Bio-ethanol	1,500	0.010$/kW h
SOFC	Natural gas	3,500	84$/kW/yr
	Bio-ethanol	3,500	84$/kW/yr

assumed at $90/MW h. The calculation does not take into account changes in electricity prices which may be triggered by the purchase of CO_2 allowances.

The analyzed cases concerned a CHP plant with installed capacity of some 300–500 kW. The assumed annual equivalent full-power working time was 4,500 h. All the electricity produced was to be used for the site's own consumption (the electricity price constituted the avoided purchase cost). The prices used were valid for the Polish market. The specific avoided cost for electricity purchases was $88/MW h—this is the average electricity purchase price for business customers according to [44]. The analysis also included revenues from renewable energy certificates in accordance with Polish regulations. The value of those was assumed to be $57.7/MW h. A similar scheme of consumption was used for heat. The assumed price of heat was $8.1/GJ.

For the generation of electricity from renewable sources (biofuels), the subsidy received is assumed at $57.7/MW h. In the case of municipal waste incineration it is assumed that 50% of the composition of the components is biodegradable, and therefore it was assumed that only half of the energy attracts subsidies (Table 5.21).

The heat produced is consumed in its entirety for own use at the assumed heat price of $8.1/GJ.

NPVs were calculated for 15 years for two types of plant: Solid Oxide Fuel Cell and reciprocating internal combustion engine (IC); and for three types of fuel: natural gas, bio-mass and bio-ethanol. The NPVs during the period of financial analysis are shown in Fig. 5.114.

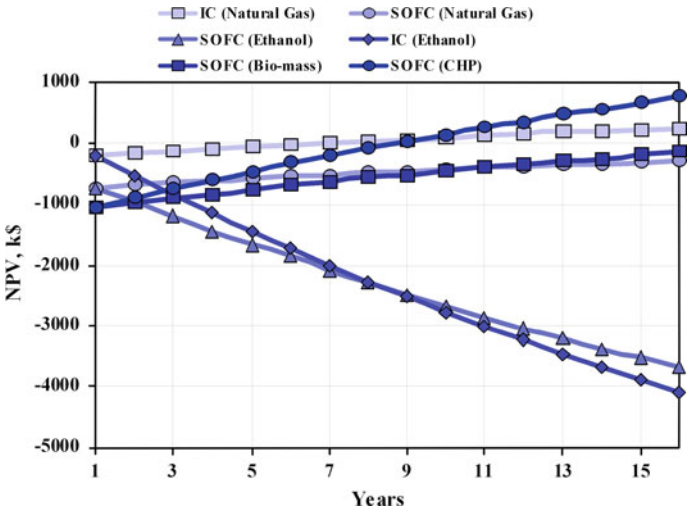

Fig. 5.114 NPV values for considered period of time

Table 5.22 Comparison of NPV values (in thousands $)

Plant type	Fuel type	
	Natural gas	Ethanol
SOFC	–291	–3,542
ICE	182	–3,513

Table 5.23 Comparison of subsidies for renewable electricity generation–current and required for NPV=0 condition

Plant type	Current subsidy ($/MW h)	Subsidy for NPV=0 ($/MW h)	Current specific cost ($/GJ)	Specific cost for NPV=0 ($/GJ)
SOFC	57.7	289.2	43.9	13.5
IC	–	321.4	43.9	16.8

The results shown in Table 5.22 show that it is not feasible to use bio-ethanol as a fuel. Therefore the next step was to calculate what level of subsidies would be required for bio-ethanol-based electricity generation or bio-fuel price to guarantee profitability (NPV=0) (see Table 5.23).

Under current conditions, bio-fuel combustion is not feasible for either fuel cell-based plants or conventional plants (such as reciprocating engines). The level of subsidies available to promote this type of fuel is insufficient. It can be seen, however, that fuel cell technology would require a smaller fuel price drop or subsidy increase to deliver profitability than would traditional engines. It is also pertinent to highlight the possibility of a significant drop in investment cost for a fuel cell plant when fuel cell technology reaches the industrial production phase.

References

1. Kakac S, Pramuanjaroenkij A, Zhou XY (2007) A review of numerical modeling of solid oxide fuel cells. Int J Hydrogen Energy 32(7):761–786
2. Virkar A (2005) Theoretical analysis of the role of interfaces in transport through oxygen ion and electron conducting membranes. J Power Sources 147(1–2):8–31
3. Milewski J, Swirski K (2009) Modelling the sofc behaviours by artificial neural network. Int J Hydrogen Energy 34(13):5546–5553
4. Zhao F, Virkar A (2005) Dependence of polarization in anode-supported solid oxide fuel cells on various cell parameters. J Power Sources 141(1):79–95
5. Jiang Y, Virkar AV (2003) Fuel composition and diluent effect on gas transport and performance of anode-supported SOFCs. J Electrochem Soc 150(7):A942–A951
6. Young D, Sukeshini AM, Cummins R, Xiao H, Rottmayer M, Reitz T (2008) Ink-jet printing of electrolyte and anode functional layer for solid oxide fuel cells. J Power Sources 184(1):191–196
7. Park HC, Virkar AV (2009) Bimetallic (Fe-Ni) anode-supported solid oxide fuel cells with gadolinia-doped ceria electrolyte. J Power Sources 186:133–137
8. Zhou W, Shi H, Ran R, Cai R, Shao Z, Jin W (2008) Fabrication of an anode-supported yttria-stabilized zirconia thin film for solid-oxide fuel cells via wet powder spraying. J Power Sources 184(1):229–237
9. Ding J, Liu J (2008) An anode-supported solid oxide fuel cell with spray-coated yttria-stabilized zirconia (YSZ) electrolyte film. Solid State Ion 179:1246–1249
10. Madsen B, Barnett S (2005) Effect of fuel composition on the performance of ceramic-based solid oxide fuel cell anodes. Solid State Ion 176:2545–2553
11. Ishihara T, Shibayama T, Honda M, Nishiguchi H, Takita Y (1999) Solid oxide fuel cell using co doped la(sr)ga(mg)o3 perovskite oxide with notably high power density at intermediate temperature. Chem Commun 13:1227–1228
12. Cai Z, Lan TN, Wang S, Dokiya M (2002) Supported Zr(Sc)O2 SOFCs for reduced temperature prepared by slurry coating and co-firing. Solid State Ion 152–153(1):583–590
13. Yao Z, Chunming Z, Ran R, Cai R, Shao Z, Farrusseng D (2009) A new symmetric solid oxide fuel cell with La0.8Sr0.2Sc0.2Mn0.8O3-D perovskite oxide as both the anode and cathode. Acta Materilia 57(4):1665–1175
14. Virkar A, Wilson L (2003) Low-temperature, anode-supported high power density solid oxide fuel cells with nanostructured electrodes. Technical report, Department of Energy, USA
15. Demuth H, Beale M, Hagan M (2008) Neural Network Toolbox 6 User's Guide Matlab
16. Foresee FD, Hagan MT (1997) Gauss-Newton approximation to Bayesian regularization. In: Proceedings of the 1997 International Joint Conference on Neural Networks
17. Tabata Y, Orui H, Watanabe K, Chiba R, Arakawa M, Yamazaki Y (2004) Direct internal reforming characteristics of SOFC with a thin SASZ electrolyte and a LNF cathode. J Electrochem Soc 151(3):A418–A421
18. Marsano F, Magistri L, Massardo AF (2004) Ejector performance influence on a solid oxide fuel cell anodic recirculation system. J Power Sources 129(2):216–228
19. Ferrari ML, Traverso A, Magistri L, Massardo AF (2005) Influence of the anodic recirculation transient behaviour on the SOFC hybrid system performance. J Power Sources 149:22–32
20. Milewski J, Miller A, Salacinski J (2007) Off-design analysis of SOFC hybrid system. Int J Hydrogen Energy 32(6):687–698
21. Sokolow J, Zinger N (1965) Ejectors (in Polish). Wydawnictwa Naukowo-Techniczne, War- saw
22. Box MJ (1965) A new method of constrained optimization and a comparison with other methods. Comput J 8:42–52

23. Bessette NF, Wepfer WJ (1996) Prediction of on-design and off-design performance for a solid oxide fuel cell power module. Energy Convers Manag 37(3):281–293
24. Costamagna P, Magistri L, Massardo AF (2001) Design and part-load performance of a hybrid system based on a solid oxide fuel cell reactor and a micro gas turbine. J Power Sources 96(2):352–368
25. Chan SH, Ho HK, Tian Y (2003) Multi-level modeling of sofc-gas turbine hybrid system. Internat J Hydrogen Energy 28(8):889–900
26. Stiller C, Thorud B, Bolland O (2005) Safe dynamic operation of a simple SOFC/GT hybrid system. In: Proceedings of the ASME Turbo EXPO
27. Stiller C, Thorud B, Bolland O, Kandepu R, Imsland L (2006) Control strategy for a solid oxide fuel cell and gas turbine hybrid system. J Power Sources 158(1):303–315
28. Calise F, Palombo A, Vanoli L (2006) Design and partial load exergy analysis of hybrid SOFC–GT power plant. J Power Sources 158(1):225–244
29. Stiller C (2006) Design, operation and control modeling of SOFC/GT Hybrid Systems. Phd thesis, Norwegian University of Science and Technology
30. Kurzke J (2004) Compressor and turbine maps for gas turbine performance computer programs
31. Brett DJ, Atkinson A, Cumming D, Ramrez-Cabrera E, Rudkin R, Brandon NP (2005) Methanol as a direct fuel in intermediate temperature (500–600°C) solid oxide fuel cells with copper based anodes. Chem Eng Sci 60(21):5649–5662
32. Kee Robert J, Zhu Huayang, Goodwin David G (2005) Solid-oxide fuel cells with hydrocarbon fuels. In: Proceedings of the Combustion Institute 30(2):2379–2404
33. Fryda L, Panopoulos KD, Kakaras E (2008) Integrated CHP with autothermal biomass gasification and SOFC-MGT. Energy Convers Manag 49(2):281–290
34. Tsiakaras P, Demin A (2001) Thermodynamic analysis of a solid oxide fuel cell system fuelled by ethanol. J Power Sources 102(1–2):210–217
35. Leone P, Lanzini A, Santarelli M, Cale M, Sagnelli F, Boulanger A, Scaletta A, Zitella P (2010) Methane-free biogas for direct feeding of solid oxide fuel cells. J Power Sources 195(1):239–248
36. Van Herle J, Marchal F, Leuenberger S, Membrez Y, Bucheli O, Favrat D (2004) Process flow model of solid oxide fuel cell system supplied with sewage biogas. J Power Sources 131(1–2):127–141
37. Staniforth J, Kendall K (1998) Biogas powering a small tubular solid oxide fuel cell. J Power Sources 71(1–2):275–277
38. Piroonlerkgul P, Laosiripojana N, Adesina AA, Assabumrungrat S (2009) Performance of biogas-fed solid oxide fuel cell systems integrated with membrane module for co2 removal. Chem Eng Process Process Intensif 48(2):672–682
39. Staniforth J, Ormerod RM (2002) Implications for using biogas as a fuel source for solid oxide fuel cells: internal dry reforming in a small tubular solid oxide fuel cell. Catal Lett 81(1):19–23
40. Jamsak W, Assabumrungrat S, Douglas PL, Laosiripojana N, Suwanwarangkul R, Charojrochkul S, Croiset E (2007) Performance of ethanol-fuelled solid oxide fuel cells: proton and oxygen ion conductors. Chem Eng J 133(1–3):187–194
41. Mahishi MR, Goswami DY (2007) Thermodynamic optimization of biomass gasifier for hydrogen production. Int J Hydrogen Energy 32(16):3831–3840
42. Sequeira CAC, Brito PSD, Mota AF, Carvalho JL, Rodrigues LFFTTG, Santos DMF, Barrio DB, Justo DM (2007) Fermentation, gasification and pyrolysis of carbonaceous residues towards usage in fuel cells. Energy Convers Manag 48(7):2203–2220
43. Iordanidis AA, Kechagiopoulos PN, Voutetakis SS, Lemonidou AA, Vasalos IA (2006) Autothermal sorption-enhanced steam reforming of bio-oil/biogas mixture and energy generation by fuel cells: concept analysis and process simulation. Int J Hydrogen Energy 31(8):1058–1065
44. Eurostat. web site: http://epp.eurostat.ec.europa.eu

45. Assabumrungrat S, Laosiripojana N, Pavarajarn V, Sangtongkitcharoen W, Tangjitmatee A, Praserthdam P (2005) Thermodynamic analysis of carbon formation in a solid oxide fuel cell with a direct internal reformer fuelled by methanol. J Power Sources 139(1–2):55–60
46. Rabenstein G, Hacker V (2008) Hydrogen for fuel cells from ethanol by steam-reforming, partial-oxidation and combined auto-thermal reforming: a thermodynamic analysis. J Power Sources 185(2):1293–1304
47. Smith JM, Van Ness HC (1959) Introduction to chemical engineering thermodynamics. McGraw-Hill Book Company, Inc. London
48. Corporation S-WP (2001) A High Efficiency PSOFC/ATS-Gas Turbine Power System—Final Report, Tech. Rep., Siemens-Westinghouse Power Corporation